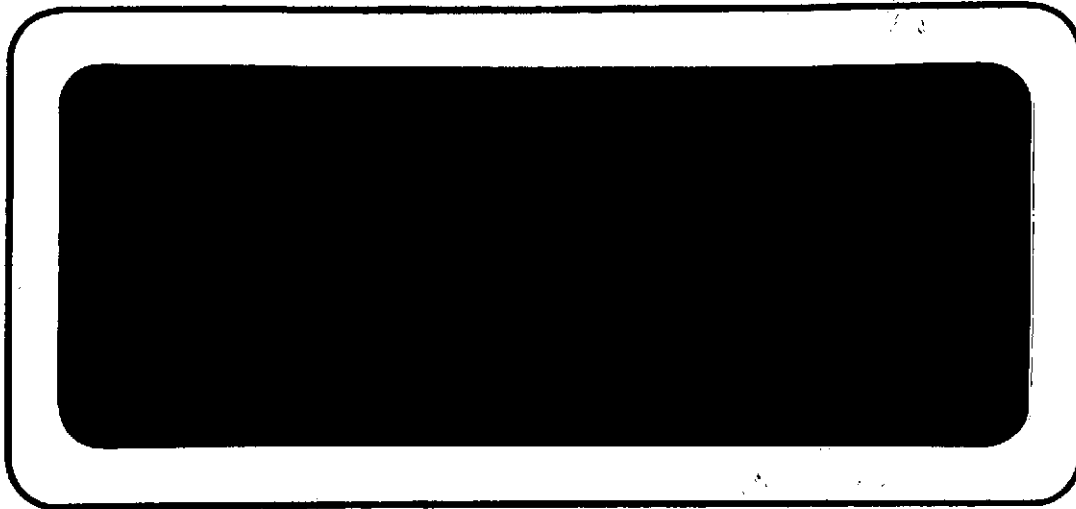


2 msk

CR 114734
Available to the Public



(NASA-CR-114734) FEASIBILITY TEST FOR A V-SLIT STAR MAPPER FOR PIONEER SPACECRAFT TERMINAL NAVIGATION Final Report (TRW Systems Group) 123 p HC \$9.25	N74-17384
	Unclas G3/21 30203

TRW
SYSTEMS GROUP

ONE SPACE PARK • REDONDO BEACH • CALIFORNIA 90278

CR-114734

AVAILABLE TO THE PUBLIC

R 7537.2-451

FEASIBILITY TEST
FOR A
V-SLIT STAR MAPPER
FOR
PIONEER SPACECRAFT TERMINAL NAVIGATION
Final Report
By R. F. Gates, J. V. Flannery, J. T. Cragin
November 1973

Distribution of this report is provided in the interest of information exchange. Responsibility for the contents resides in the author or organization that prepared it.

Prepared under contract NAS 2-7597 by
TRW Systems Group
Redondo Beach, California
for
AMES RESEARCH CENTER
NATIONAL AERONAUTICS AND SPACE ADMINISTRATION

FOREWORD

This report was prepared by TRW Systems Group for the National Aeronautics and Space Administration, Ames Research Center under Contract NAS 2-7597.

The TRW Project Engineer was R. F. Gates. Other contributing authors of this report were J. V. Flannery, J. T. Cragin, S. A. Munar, and M. C. Jennings. Assisting the Project Engineer as consultants were W. J. Dixon and H. F. Meissinger.

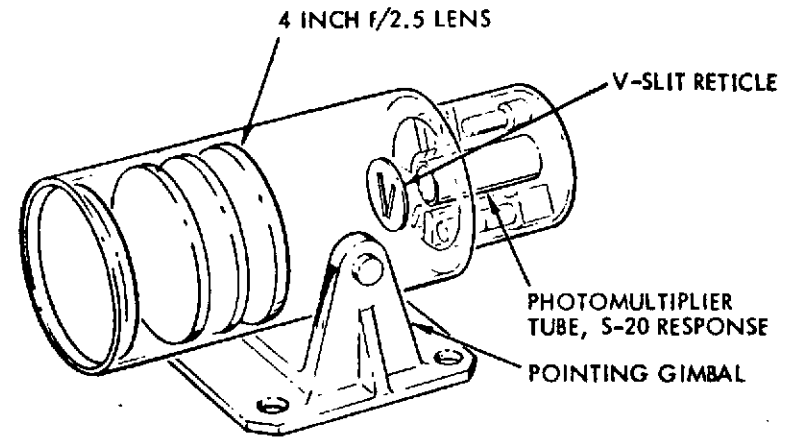
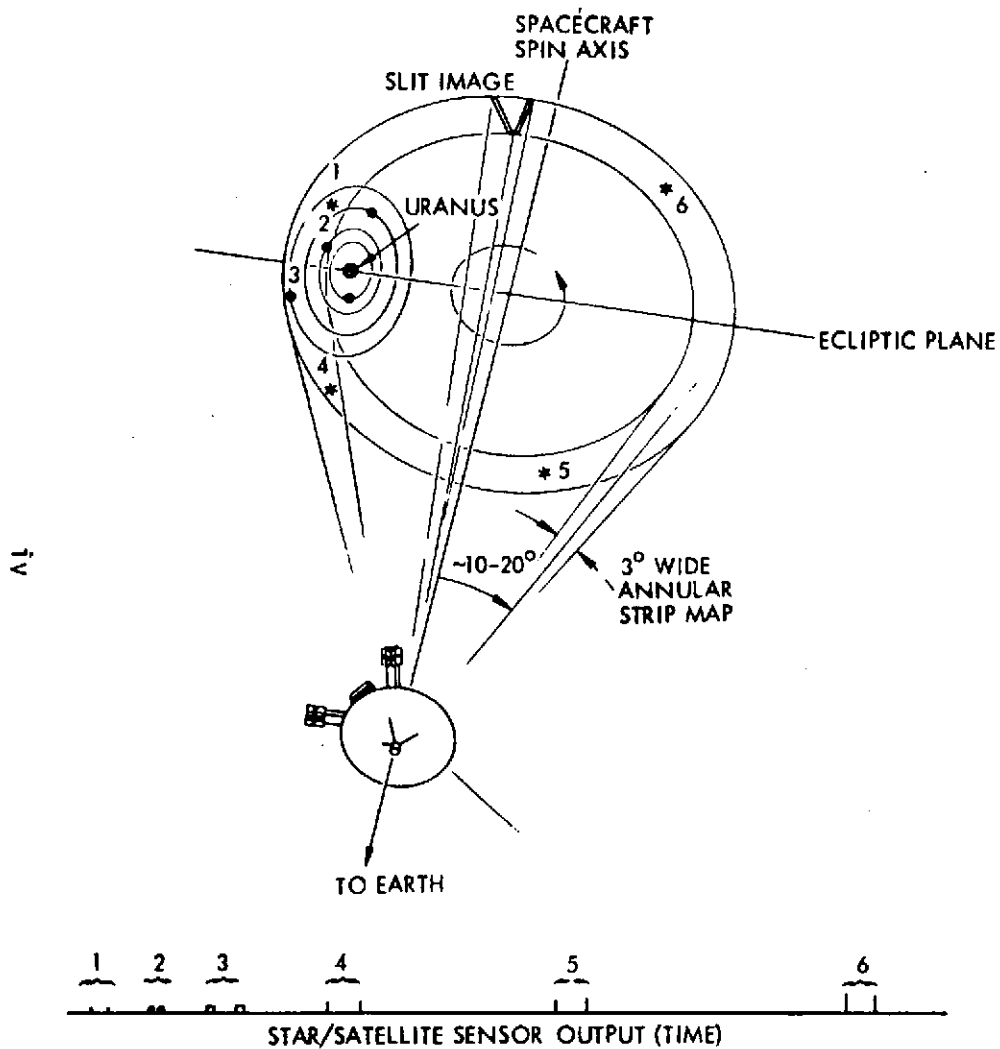
PREFACE

This report conveys the results of tests of a V-slit star mapper. The tests were conducted to determine the feasibility of such a sensor to provide on-board navigational data for a spinning spacecraft (Pioneer) on missions to planets beyond Jupiter.

This preface reviews the on-board navigation approach conceived for a representative mission — the Pioneer Saturn/Uranus atmospheric probe mission — and indicates the performance requirements for the sensor. The body of the report indicates that the V-slit sensor telescope does meet these requirements. Other aspects of the navigation process were not treated in the study.

For the Saturn/Uranus mission, in which an atmospheric entry probe is delivered to Uranus after an earth-Saturn-Uranus interplanetary flight, navigation using only earth-based radio measurements is inadequate or at best marginal for the approach to Uranus, primarily because of the large uncertainty in the ephemeris of the planet. The use of on-board optical data reduces the trajectory error almost an order of magnitude, and satisfies mission requirements. While radio navigation alone will suffice for other phases of this mission, the use of on-board optical sensing in addition at the approach to Saturn can significantly cut propellant requirements for the corrective maneuver following the Saturn swingby. These results are described in Reference 1, and are based on a one-sigma error of 0.1 milliradians (20 arc seconds) in the measurement of the direction from the spacecraft to a satellite of the target planet.

The desired result of the navigation process, the direction in celestial coordinates from the spacecraft to the target planet, is not measured by the sensor directly. It must be deduced from the sensor measurements, which consist of pulse pairs corresponding to each bright celestial object in the 3-degree-wide swath swept by the field of view in a single spacecraft revolution, as shown in Figure i. If the objects detected in a single swath — i.e., without changing the sensor gimbal angle — include the designated satellite and at least two fixed stars, the deduction of the direction to the target planet is straightforward, encompassing the steps shown in Table i.



- MINIMUM NUMBER OF REFERENCE STARS IS TWO
- STAR PATTERN IDENTIFIED IN ADVANCE OF TARGET DETECTION
- STAR MAPPER ALSO ACCURATELY DETERMINES SPIN AXIS POINTING ON CELESTIAL SPHERE
- PLANET'S SATELLITES ARE PREFERABLE AS NAVIGATIONAL REFERENCES: SMALLER IMAGE SIZE; MASS CENTER DETERMINATION SIMPLIFIED
- INTERFERENCE BY BRIGHT PRIMARY IMAGE TO BE AVOIDED

Figure i. Terminal Navigation Sensor Operation

Table i. Navigation by On-Board Optical Sensor Measurements

Step	Object	Quantity	Approximate Precision (milliradians, 1σ)	
			a priori	a posteriori
Measurement by V-slit star mapper	Star No. 1 Star No. 2 Planetary satellite	Cone angle of the ob- ject relative to the boresight of the sensor	3 3 3	0.05
	Star No. 2 Planetary satellite	Clock angle of the ob- ject relative to the clock angle of Star No. 1	1 2	0.05
Intermediate quantities (from a single set of measurements)	Spin axis of spacecraft	Pointing direction (2 coordinates)	2	0.1
	Boresight of the sensor	Angle to spin axis of spacecraft	3	0.1
Intermediate quantities (requires repeated measure- ments over an orbital cycle)	Planetary satellite	Ephemeris about target planet (6 parameters)		(improved)
Final desired output	Target planet	Direction (in celes- tial coordinates) from spacecraft (2 coordinates)	1 (from radio naviga- tion)	0.1

The intermediate quantities of Table i are determinable in two processes. From a single set of measurements of two identifiable stars and one satellite it is possible to estimate by triangulation the precise spin axis orientation and boresight cone angle, as well as the direction to the satellite. From such measurements repeated over the orbital period of the satellite about the planet, the ephemeris of the satellite about the planet will be determinable with improved precision, and the final desired quantity may be estimated to the desired precision.

This determination must be accomplished early enough in the mission to allow for a trajectory correction maneuver before the entry probe is released from the spacecraft to proceed on its final descent trajectory. This requirement, imposed with respect to Uranus' satellite Titania, leads to a sensitivity requirement of brightness magnitude 4.0.

Titania appears this bright at the spacecraft 26 days before its arrival at Uranus. The probe is to be released about 20 days before arrival, allowing six days for navigation and trajectory correction. The brightness threshold must also be low enough to lead to the expectation of two or more observable stars in the 3-degree swath. The magnitude 4.0 threshold provides an average of four observable stars in the swath at either Saturn approach or Uranus approach. See also Reference 1 for specific star maps.

Reference 2 explores the above concepts and requirements for on-board optical sensor measurements in considerably greater detail, supporting the performance standards of Table ii for the V-slit telescope (optics, V-slit reticle, plus electro-optical sensor).

The object of this feasibility test is to verify that the V-slit telescope can meet the performance of Table ii.

There are other links in the chain of logic leading to complete verification of the on-board optical navigation approach. Some have been covered in other documents; others remain to be addressed, but are beyond the resources available for this feasibility test. Areas not covered in the body of this report include the following:

- a) Details of the algorithms which carry out the navigation processes implicit in Table i. (Results of such navigation processes are presented in Reference 1.)

Table ii. V-Slit Telescope Requirements

Spacecraft spin rate	5 rpm
Gimbal angle range (measured from spin axis, anti-earth direction)	5 to 110 degrees
Gimbal angle assumed in test	40 degrees
Field of view (in cone angle direction)	3 degrees
Brightness threshold	4.0 magnitude
Angular precision of measurement*	0.05 mrad (10 arc seconds)
Accuracy of measurement**	(assumed attainable by calibration)

* Accounting for all random errors.

** Accounting for all bias errors and nonlinearities.

- b) Analysis of non-random errors (biases and nonlinearities). (It is assumed that ground and flight calibration will compensate for these errors.)
- c) Analysis and test of light shielding methods to avoid interference from the proximity of a bright object (planet) while measuring the satellite. (Suggested future study and test.)
- d) Definition of the star mapper system design, emphasizing the interface with the spacecraft. This would treat portions of the star mapper in addition to the telescope itself, and would define the system so as to address the following subjects:
 - Weight
 - Power requirements
 - View angle
 - Mounting provisions
 - Temperature requirements
 - Gimbal accuracy, resolution, control, etc.
 - Command requirements to effect mode changes, status changes, gimbal rotations, threshold variations, etc.
 - Signal conditioning requirements
 - Telemetry requirements

- Reliability and lifetime requirements
- Requirements for use of the star mapper as a roll position sensor for cruise portions of the mission.

This definition would be based on a nominal mission profile, although applicability to a wide class of missions would be sought.

The requirements critical to the navigation process — ability to measure dim celestial bodies (4.0 magnitude or dimmer) with precision adequate for navigation requirements (0.05 milliradian, one sigma) — have been verified in this feasibility test.

TABLE OF CONTENTS

Title Page	i
Foreword	ii
Preface	iii
Table of Contents	ix
Section (1) Summary	1
Section (2) Introduction	3
Section (3) Symbols	5
Section (4) Sensor Description	13
Section (5) Analysis	18
Section (6) Test Set	32
Section (7) Test Program	41
Section (8) Test Results	44
Section (9) Conclusion	49
Section (10) References	50
Section (11) Appendices	51

SECTION 1

SUMMARY

A laboratory demonstration of the feasibility of using a V-slit star mapper to meet the sensitivity and accuracy of on-board navigational requirements for future Pioneer Missions to the outer planets has been conducted by the Control and Sensors Laboratory of TRW.

The V-slit star mapper breadboard used in the laboratory tests was made available from another program at TRW. Thus, the physical configuration was predetermined. In like manner, the mechanical test set used in testing the sensor was made available to the project by the Pioneer-Jupiter program at TRW on a no conflict basis.

The first major thrust of the project was to determine analytically if the breadboard sensor could meet the performance required. The breadboard was extremely simple in configuration, consisting of an end-on photomultiplier tube and a V-slit reticle located at the focal plane of the objective lens. In addition, a plano-convex lens was used between the reticle and the PMT in a Fabry-Perot configuration. The analytical effort indicated that the sensor should easily meet the requirements and the second major effort began. This was to test the Pioneer SRA test set to determine its basic accuracy and modify it where necessary to bring its accuracy into the 1-3 arc second range. This proved to be a much larger problem than expected. The rotating mirror spin rate stability became the critical factor. It was finally resolved by driving the synchronous motor with a high-fidelity power amplifier excited by a precision sine wave generator.

The final portion of the program was the actual testing of the mapper. First indications were that the mapper was less sensitive than expected by at least 2-1/2 star magnitude. This was traced to the process technique used to fabricate the reticles. The "clear" slit areas had a transmission of only 10 to 15%. A new chrome plated reticle with much more acceptable transmission characteristics was subsequently substituted. All

reduced data included in this report was taken using the new reticle.

The test results show that it is feasible to use this type of star mapper in the 10 arc second accuracy range. The test equipment accuracy (~ 5 arc sec) was sufficient to bound the sensor errors at less than 10 arc seconds. In order to verify with much more precision the accuracy of the sensor, a more sophisticated test set would be required. One major improvement would be the use of an air bearing table for controlling the motions of the scanning mirror.

SECTION 2

INTRODUCTION

It is anticipated that in the near future fly-by and entry probes will be flown to the outer planets, i.e., Saturn and Uranus. If these missions are to be successfully completed highly accurate navigational information will be required. Present earth based observation of the outer planets yields uncertainties in planet position of 10^3 to 10^4 Km and the same inaccuracies in navigation of the probes would result if these ephemerides were used. An on-board sensor could provide the accurate targeting required for the control of atmospheric probe entry points, and to reduce post-encounter correction for multiple planet missions. One such approach considers the use of a V-slit star mapper to determine the direction to the planets' satellites against the stellar background.

The objective of this program was to demonstrate in a laboratory environment the feasibility of using a V-slit star mapper to meet the sensitivity and accuracy required by the navigational systems that might be used in future Pioneer spacecraft flights.

The test program was primarily directed to the consideration of the navigational information required for planetary fly-by missions, in which the star mapper targets would be the fixed stars (for reference) and the natural satellites of the outer planets. For a certain class of missions these satellites will always be observed at a zero or near zero aspect angle which means that they will be in a full phase condition.

The program was based upon two important considerations; 1, that a breadboard sensor would be available from another TRW program, 2, that the Pioneer-Jupiter SRA Unit Test Set would be available and could be modified to provide the accuracy needed.

The program was organized into three major tasks

- (1) Performance Analysis and Trade offs
- (2) Preparation of Test Facility and check out
- (3) Testing

This organization of tasks is slightly different than that listed in the Contract Statement of Work. The tasks are organized in this manner since it represents the way in which the work was actually performed.

The symbols used in the report are defined in Section 3, while Section 4 describes the sensor used in the tests. An analysis of the sensor performance is detailed in Section 5. The following sections describe the test equipment, test program, and test results. Section 9 is a concluding paragraph, while references are listed in Section 10, followed by the technical appendices. Appendices A thru F represent analytical studies done early in the program and are included for completeness.

SECTION 3

SYMBOLS

This section contains a list of symbols and their definitions as used in the report. Since the report was prepared by several people, the same symbols were used for different variables. Rather than try to come up with a completely non-redundant symbology, the report was carefully culled, and subscripts or superscripts added for distinguishing purposes. Even so there are probably some symbol corrections that have slipped by.

α, β	Angle formed by the slits with respect to the clock reference plane.
α_V, β_V	Angles of V-slit scanner Boresight relative to spacecraft axes.
α_{sm}	Rotation angle when star target enters measurement slit.
α_{sr}	Rotation angle when star target enters reference slit.
$\alpha', \beta', \gamma', \delta'$	Limit of integration determined by details of slit location.
β_s	Angle between star line of sight and spacecraft \bar{Z} axis.
γ	Angular target size.
δ	Angle formed by \bar{Z} and \bar{L} .
δ_{SM}	Angle between \bar{Z} and \bar{L} at time T_{SM} .
δ_{SR}	Angle between \bar{Z} and \bar{L} at time T_{SR} .
$\frac{\Delta\delta}{\Delta T}$	Rotational rate of star target.
$\frac{\Delta\alpha_V}{\Delta T}$	Time rate of change of α_V .
$\frac{\Delta\beta_V}{\Delta T}$	Time rate of change of β_V .
ΔT_c	Time interval between two signal pulses.

ΔT_1	Time interval between the first encoder wheel pulse and first signal pulse.
ΔT	RSS value of total time error.
Δt	Signal pulse width.
ζ	Linear width of slit.
η	Quantum efficiency of detector.
η'	Spacecraft clock angle.
θ	Aspect angle
θ_1	The angle between the normal to the object and the direction of radiation.
θ'	Angle formed by \bar{Z}' and Z.
κ	Angular width of slit.
μ	Cosine θ_1 .
ν	Spectral frequency band.
ν_1, ν_2	Spectral frequency bounds.
ξ	Correction for viewing aspect.
τ	Transit time of target between slit centers.
ϕ	Spacecraft cone-angle.
$\tilde{\phi}$	Reference frame of V-slits.
ψ	Angular separation of slits at their truncation.
ω	Spacecraft rotational velocity.
a	Major Axis of an ellipse representing the illuminated area of a moon, in Gibbous or Crescent Phase.
A_i	Object albedo at color i.

A	Minimum collecting aperture of objective lens.
A_v	Object's albedo.
A1, 2	Encoder wheel alignment apertures.
A,B	Slit designators.
b	Minor Axis of ellipse representing the illuminated area of a moon and the radius of a . moon when assumed to be a circle.
b^{II}	Galactic latitude.
C	Photocathode surface of photomultiplier.
c	Speed of light.
C_1	Constant
cm	Centimeter
D	Optics diameter.
e	Electronic charge.
E1	First encoder wheel pulse.
E2	Second encoder wheel pulse.
$E_{s,v}$	Amount of energy intercepted by the object.
$E_{s,v \text{ out}}$	Energy emitted by the object.
F_v	Optical filter Transmission.
F	V-Slit sensor focal length.
FL	Field lens.
FS	Field lens and reticle.
G	Photomultiplier tube gain.
h	Planck's constant.

$H_{m_v} = 4$	Flux from a $m_v = 4$ star.
H_s	Flux emitted by an object.
$H_{s,v}$	Monochromatic solar flux at the object.
$H_{o,i}$	Solar surface flux.
$H_{o,i}$	Irradiance in spectral band V at the observer.
$H_{o,v}$	Flux seen by an observer.
i	Summation increment.
I	The illuminated portion of the disk contained within the projected slit.
i_d	Image distance.
I_A	S-20 photomultiplier detector response for a 4 th , magnitude star corrected for optical transmission.
$I_{s,v}$	Solar radiance in the spectral band V .
I_S	Anode signal current.
I_{ii}	General illumination parameter (slit perpendicular to illumination Vector).
I_{iii}	General illumination parameter (slit parallel to illumination Vector).
I_{pc}	Photocathode current.
$I_{o,v}$	Solar radiance.
k	Boltzman's constant.
$k_{i,v}$	Optical element transmission of i th element.
z^{II}	Galactic longitude.
\bar{L}	Path of target radiation.

L_{pg}	Photographic threshold level.
L_v	Visual threshold level.
m	Star magnitude.
m_{pg}	Photographic star magnitude.
m_v	Visual star magnitude.
$m_{o, i}$	Apparent magnitude of an object at an arbitrary location.
$m_{o, i}$	Magnitude of object at the earth for the color i .
$m_{o, l}$	Apparent magnitude of a target at a Range $R_{o, o}$.
mm	Millimeter
n	Index of refraction.
n''	Target signal (photon flux).
n_o	Photon flux due to a 4^m star.
N	Total background noise.
N'	Background signal (photon flux).
N_B	Background signal.
$N_{m_v=4}$	Photon flux from a $m_v = 4$ star.
N_o	Worst case background signal.
$N_{o, i}$	Photon flux at the observer in the spectral band v .
$N_{\Delta t}$	Number of photoelectrons in pulse width Δt .
O	Objective lens.
\bar{O}	Line of sight on the reticle through the optics and into space.

P	Total random error of V-slit mapper.
P_F	Probability of a false detection.
P_T	Probability of true detection.
q	Representative mathematical symbol.
r	Sun - object distance.
r''	Radius of curvature of field lens.
r_o	Object - observer distance
r_o	Radius of the earth.
R_s	Object radius.
R_1	Reset pulse.
R_o	Solar radius.
$R_{o, o}$	Range between earth and sun.
$R_{o, o}$	Range between earth and observer.
rpm	Revolutions per minute
S	Signal at the photomultiplier cathode.
S'	Signal level.
S_B	Background signal.
S_T	Target signal
S1	First signal pulse.
S2	Second signal pulse.
S/N	Photon statistical signal to noise ratio.

sr	Steradian
t	Integration time.
t_B	Time of detection in slit B.
t_{clock}	Time at which the target crosses the reference plane.
$t_{1,B}$	Time of detection of target center in slit B.
$T_{SM} - T_{SR}$	Time interval between star pulses when sun in measurement and reference slits.
T	Absolute temperature.
T'	Target signal.
x, y	Variables in the equations for a circle and ellipse.
x_c	The value the x variable assumes for a given value of y in the equation for a circle.
x_e	The value the x variable assumes for a given value of y in the equation for an ellipse.
x_0	Center of slit width (slit perpendicular to illumination vector).
\bar{X}_v, \bar{Y}_v	Plane in which the reticle lies.
$\bar{X}, \bar{Y}, \bar{Z}$	Spacecraft reference frame orientation.
$\bar{X}', \bar{Y}', \bar{Z}'$	Test setup reference frame orientation.
$\bar{X}'', \bar{Y}'', \bar{Z}''$	Sensor reference frame orientation with respect to the spacecraft.
y_c	The value the y variable assumes for a given value of x in the equation for a circle.

y_e	The value the y variable assumes for a given value of x in the equation for an ellipse.
y_o	Center of slit width (slit parallel to illumination vector).
$y_{o,iii}$	Center of slit width for general illumination expression (slit parallel to illumination vector).
Z	Spacecraft spin axis.
\bar{Z}''	Sensor boresight axis.

SECTION 4

SENSOR DESCRIPTION

The V-slit star mapper is relatively simple in concept, being composed of only 5 major components,

- o Objective lens
- o V-slit reticle
- o Field lens
- o Photomultiplier
- o Video processor

A pictorial schematic of the sensor is shown in Fig. 1.

In operation, the stellar radiant energy is collected and focused by the objective lens on the V-slit reticle. As the spacecraft rotates this image crosses the reticle, and when the stellar image is in the slit, the radiant energy passes through the field lens and falls on the photocathode and causes a signal to be generated. This signal is then amplified by the secondary emission multiplier to produce an electrical current at the anode. This signal is further amplified, bandwidth limited, and thresholded in the video processor. The resultant output pulses are used in the test circuitry to determine clock and cone angles relative to the boresight axis of the sensor.

The various components are mutually interdependent; however, since the PMT is the least flexible it is usually taken as the starting point.

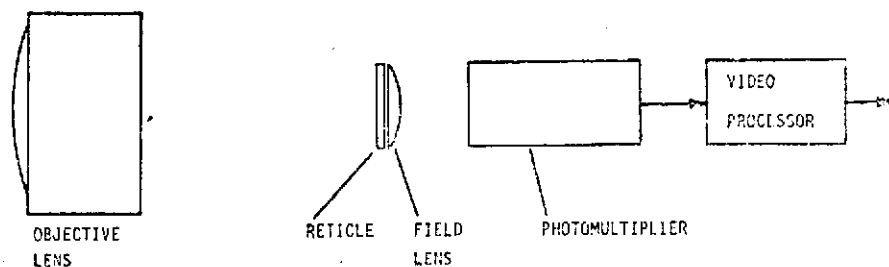


Figure 1. Pictorial Schematic

The Photomultiplier

Since the stars cover a wide spectral band, the spectral response of the detector must cover wavelengths from 370 to 800 nanometers. The tri-alkali or S-20 photocathode covers this range and is the most sensitive and noise free photocathode of this general type. The physical size of the photocathode was selected as 25 mm on the basis of field of view and sensitivity requirements discussed in the next paragraph. EMR's 541E-01-14 met these requirements and in addition is stable, rugged, and reliable. It is composed of a fused envelope containing a series of metal rings which serve as rugged electrical contacts to the silver magnesium venetian blind dynodes. A unique photocathode processing technique removes the excess formation materials from within the tube, giving assurance that no contamination can occur during operation. The tube is potted with 3.9 megohm resistors in the high voltage divider network. The factory test data is reproduced in Appendix H.

Objective Lens

Two parameters of the objective lens needed to be specified are the collecting aperture and the focal length. The collecting aperture is determined by the basic sensitivity required and the focal length is determined by the required field of view and the accuracy desired.

Sensitivity

It is necessary to achieve sufficient signal from a fourth magnitude star to meet the signal to noise requirements. Forbes and Mitchell² list stellar photometric data for several photocathodes, among them the S-20. It is customary to use an A0 class star as the standard, since its visual magnitude and photoelectric magnitude are identical by definition. The data lists the S-20 detector response in amperes/cm² of telescope aperture for α Lyra (Vega) as 0.803×10^{-13} amperes/cm². Since Vega is a zero magnitude star, it is an easy matter to extend this

data to 4th magnitude and obtain 2.0×10^{-15} amperes/cm². With an optical loss of 40%, the energy reaching the PMT would be reduced so that the photocathode current (I_A) would be 1.2×10^{-15} amperes/cm².

If the width of the slit is 20 arc seconds, and the worst case spot size is 20 arc seconds, then the total signal pulsewidth time at 5 rpm would be approximately one millisecond.

The major noise source in the sensor is shot noise in the signal. This noise leads to an uncertainty in position determination called Noise Equivalent Angle (NEA). In the V-slit mapper an NEA of 2 arc seconds was considered to be sufficiently low enough to make the overall sensor accuracy less than 10 arc seconds. Thus the NEA is given by

$$NEA = \frac{1}{\sqrt{N_{\Delta t}}} (\kappa + \gamma)$$

where κ is the angular slit width = 20 arc seconds
 γ is the angular target size = 20 arc seconds
 $N_{\Delta t}$ is the number of photoelectrons in pulsewidth Δt or
 $N_{\Delta t} = 400$ photoelectrons

The photocurrent is

$$I_{pc} = \frac{N_{\Delta t}}{\Delta t} \times e = .64 \times 10^{-13} \text{ amperes.}$$

The minimum collecting aperture of the lens is given by

$$A = \frac{I_{pc}}{I_A} = \frac{.64 \times 10^{-13}}{1.2 \times 10^{-15}} = 53.3 \text{ cm}^2$$

Focal Length

The focal length of the objective lens is determined by the slit width and length needed to obtain the desired field of view.

In order to make the slit relatively easy to fabricate, it was decided to make the minimum slit width 2.54×10^{-3} cm.

If this is to be equivalent to 20 arc sec, then the focal

length must be 26.2 cm.

A standard commercial lens was selected that was reasonably close to this, being 300 mm f/3.5. Thus, the effective slit width is 17.4 arc seconds, and the collecting aperture is 59.6 cm^2 , giving approximately a 10% margin on signal.

The V-Slit Reticle

The width of the slit was shown to be 17.4 arc seconds with the 300 mm focal length lens. The desired length of the slits was 3 degrees, making the physical length about 17.5 mm. Appendix K shows the details of the reticle.

The Field Lens

The field lens is a plano-convex lens used to image the objective lens on the photocathode. The details of this are in Appendix B. The lens selected for this purpose has a 17.8 mm diameter and a 31 mm focal length.

The Video Processor

A simplified schematic diagram of the video processor is shown in Figure 2. The 100K ohm resistance is the anode load resistor for the PMT. The peak anode signal current on a 4th Mv star is given by

$$I_S = I_A \cdot A \cdot G = 143 \times 10^{-9} \text{ amperes.}$$

where $I_A = 1.2 \times 10^{-15} \text{ amperes/cm}^2$

$$A = 59.6 \text{ cm}^2 = \text{area of objective lens.}$$

$$G = 2 \times 10^6 = \text{gain of PMT.}$$

Thus the peak signal voltage developed across the anode load resistor, 14.3 millivolts, is fed to a voltage follower to change the impedance level. This stage is followed by a LM118 operational amplifier with a stabilized gain of 100 feeding into another LM118 with a stabilized gain of 4. At this point a anode signal current

of 100 na would generate a signal of 4 volts. This signal is then thresholded in an LM211 comparator. The nominal threshold is set at 2 volts, but is adjustable for experimental reasons. The output of the video processor is a +5V peak signal which is used to activate the logic circuitry described in Section 6.

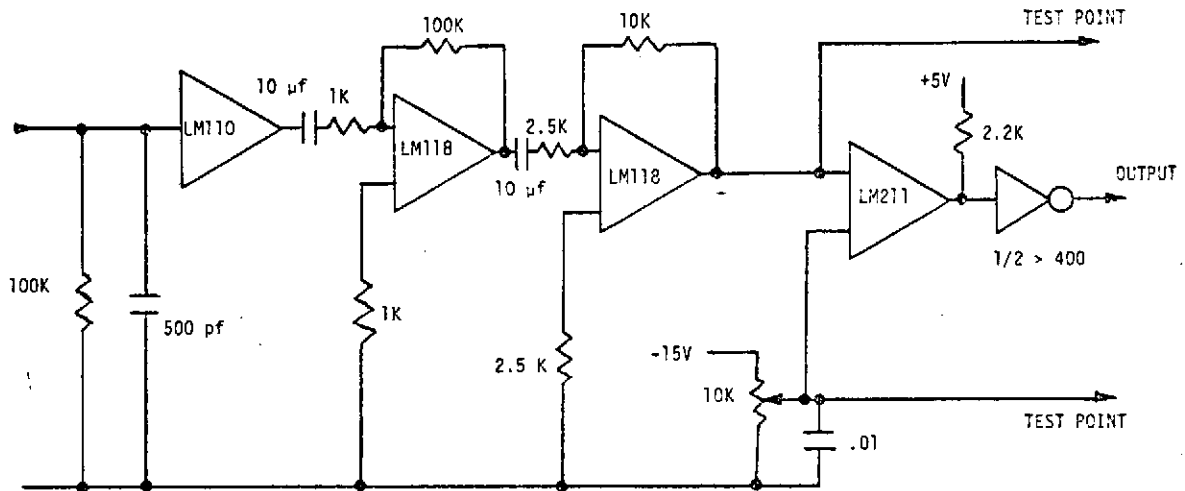


Figure 2. Video Processor

In order to provide a gain margin, the video processor was designed to operate on signals as low as 5 millivolts. The desired bandwidth of the amplifier is

$$\Delta f = \frac{1}{2\tau}$$

where τ = pulsewidth (seconds) = 1 millisecond (at aspect angle of 40° with 20 arc second target)
giving $\Delta f = 500$ Hz

When the aspect angle is 90°, the bandwidth necessary to pass the signal would be 1600 Hz with a 20 arc second target, and 3200 Hz with a point source (star) target. The bandwidth of the amplifier was therefore set at the maximum by placing a 500 pf capacitor across the 100K anode load resistance.

SECTION 5

ANALYSIS

This section covers the relationship between the test parameters and the parameters relevant to the flight application. The comparison is necessary to correctly determine the space performance from the laboratory test results. Therefore both sets of parameters are derived, and the errors associated with the test equipment and sensor estimated.

Flight Parameters

Figure 3 shows the coordinate system that is used in the subsequent analysis.

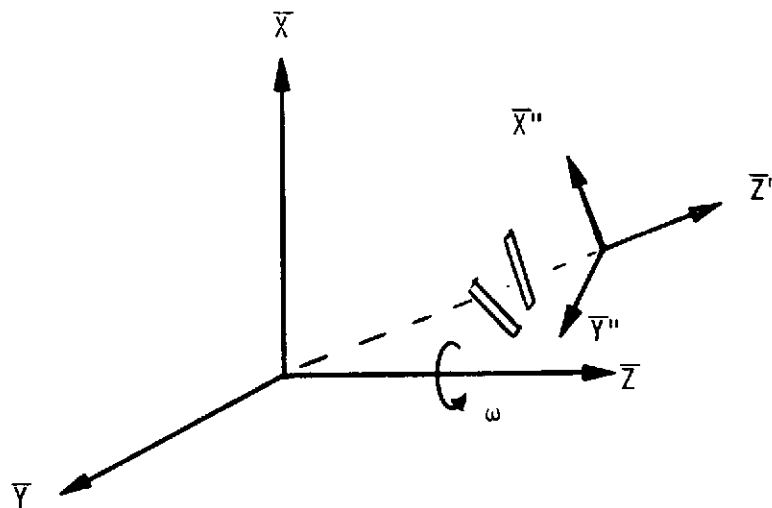


Figure 3. Sensor Field of View Relative to Spacecraft Coordinate

The projected field of view at both the reference slit and the measurement slit are shown in this figure. The \bar{Z}''

axis represents the sensor boresight axis. Orientation of the sensor triad $(\bar{X}'' , \bar{Y}'' , \bar{Z}'')$ may be related to the spacecraft triad $(\bar{X} , \bar{Y} , \bar{Z})$ by two angles α_V and β_V . Angle α_V is rotation of the V Slit Scanner Boresight about the \bar{Z} axis, and β_V is the angle between the sensor boresight and the \bar{Z} axis. Using matrix notation -

$$\begin{bmatrix} \bar{X}'' \\ \bar{Y}'' \\ \bar{Z}'' \end{bmatrix} = \begin{bmatrix} \cos\alpha_V \cos\beta_V & \sin\alpha_V \cos\beta_V & -\sin\beta_V \\ -\sin\alpha_V & \cos\alpha_V & 0 \\ \cos\alpha_V \sin\beta_V & \sin\alpha_V \sin\beta_V & \cos\beta_V \end{bmatrix} \begin{bmatrix} \bar{X} \\ \bar{Y} \\ \bar{Z} \end{bmatrix} \quad (1)$$

Figure 4 aids in defining the field of view of the V-Slit Scanner as determined by the reticle/optics geometry.

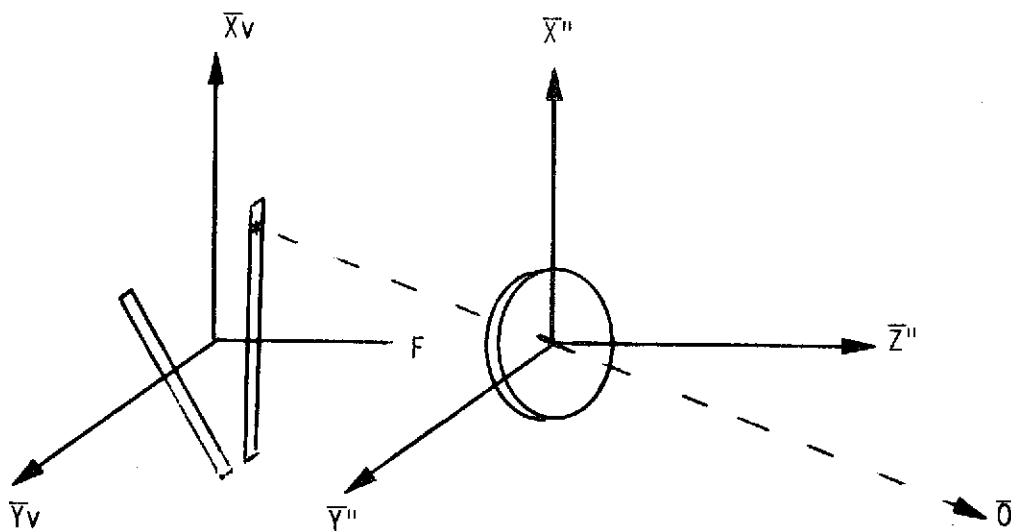


Figure 4 Reticle/Optics Geometry

The reticle lies in the $\bar{X}_v \bar{Y}_v$ plane. Dimension F is the effective focal length of the optics. Figure 5 identifies the dimensions for one of the reticles that is used in the testing. Dimensions are in inches.

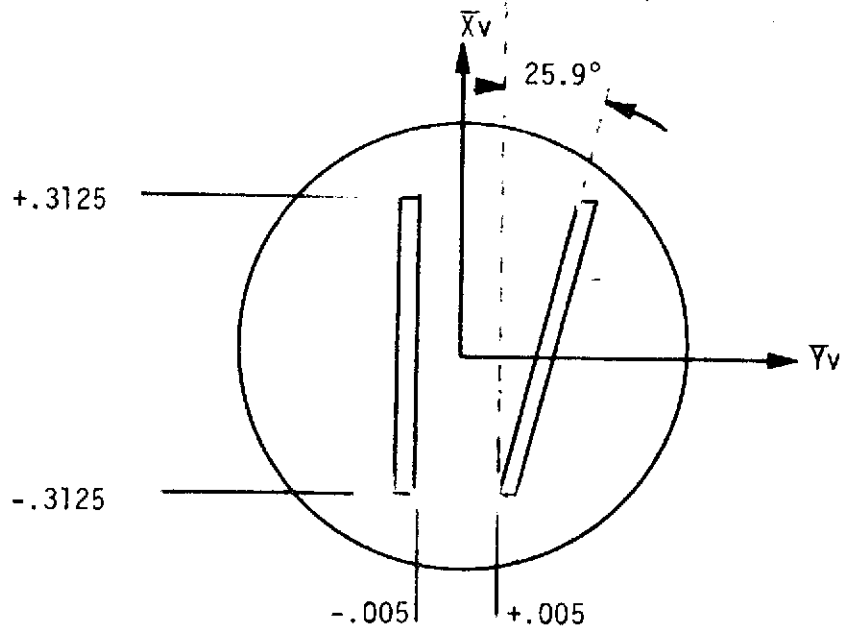


Figure 5. V-Slit Reticle

The line of sight from any point (X_v, Y_v) on the reticle, through the optics and into space is given by the following expression -

$$\bar{O} = \frac{X_v \bar{X}'' + Y_v \bar{Y}'' + F \bar{Z}''}{\sqrt{X_v^2 + Y_v^2 + F^2}} \quad (2)$$

By combining expressions 1) and 2) and substituting appropriate values of X_V and Y_V for the slit boundaries, the field of view of the scanner may be computed. (Fortran Program in Section 11.) Figure 6 shows the projected field of view as measured in spacecraft coordinates. For this representative case the sensor boresight is 40% off the spacecraft \bar{Z} Axis. The slit boundaries appear relatively linear on the graph. However, a slight nonlinearity exists as evidenced by the computer printout (Table I) of the boundaries. Ground software would be implemented to incorporate the exact trigonometric functions rather than any linear approximation. The dashed lines in Figure 6 represent the viewing corridor for the reference slit, after 5° of rotation about the \bar{Z} Axis.

This example demonstrates that a star which is 2384 arc minutes ($39^\circ 44'$) off the \bar{Z} Axis generates a 5° rotation angle separation between pulses from the reference and measurement slits. For other star angles (β_S) the approximate relation is -

$$\beta_S = 2304.5 + 1.32 (\alpha_{SM} - \alpha_{SR}) \text{ arc minutes} \quad (3)$$

Where α_{SM} and α_{SR} are the rotation angles when the star enters the respective measurement and reference slits. Assuming a spin rate of 5 rpm, angle β may be inferred from the time interval ($T_{SM} - T_{SR}$ seconds) between star pulses at the two slits

$$\beta_S = 2304.5 + 2400 (T_{SM} - T_{SR}) \quad (4)$$

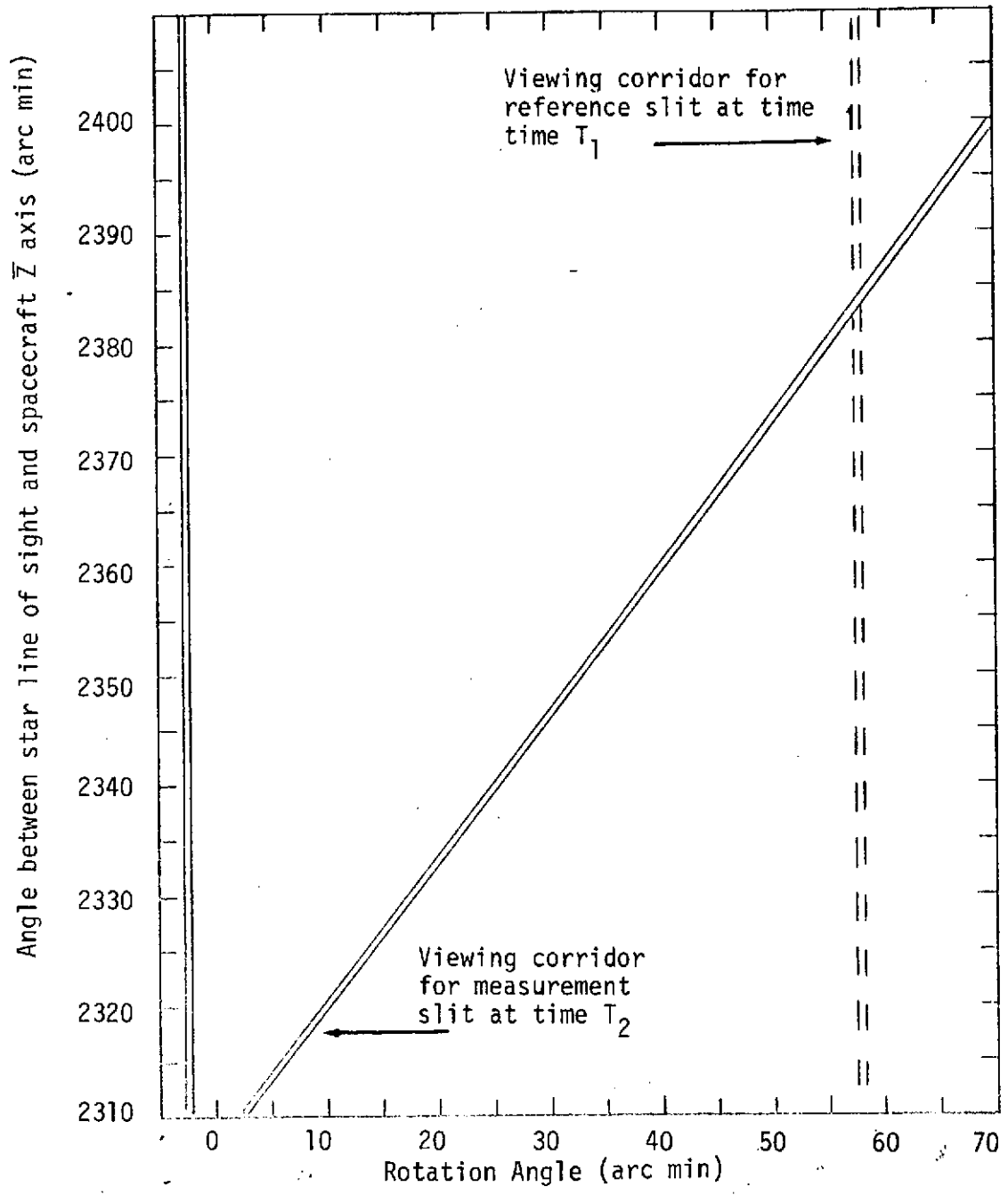


FIGURE 6. FIELD OF VIEW FOR 25.9° RETICLE

Table 1 Slit Boundaries in Arc Minutes for 40° boresight angle and 25.9° Reticle

Reference		Measurement	
ROTATION	ANGLE OFF Z AXIS	ROTATION	ANGLE OFF Z AXIS
0.			
-2.299785925	2.31049386E+03	2.299785925	2.31049386E+03
-2.292443386	2.319440843E+03	9.249607545	2.31944654E+03
-2.285147582	2.328388917E+03	1.615511815E+01	2.328407084E+03
-2.277898069	2.337337961E+03	2.301668498E+01	2.337375264E+03
-2.270694409	2.346287855E+03	2.9834672E+01	2.346350854E+03
-2.263536167	2.355238477E+03	3.660943997E+01	2.355333626E+03
-2.256422914	2.364189707E+03	4.33413464E+01	2.364323356E+03
-2.24935423	2.373141421E+03	5.003074561E+01	2.373319816E+03
-2.242329694	2.3820935E+03	5.667798878E+01	2.382322782E+03
-2.235348897	2.391045822E+03	6.32834239E+01	2.39133203E+03
-2.228411429	2.399998265E+03	6.984739585E+01	2.400347336E+03
5.0E-01			
2.770018794E+01	2.31049386E+03	3.229975979E+01	2.31049386E+03
2.770753048E+01	2.319440843E+03	3.924958141E+01	2.31944654E+03
2.771482629E+01	2.328388917E+03	4.615509202E+01	2.328407084E+03
2.77220758E+01	2.337337961E+03	5.301665885E+01	2.337375264E+03
2.772927946E+01	2.346287855E+03	5.983464587E+01	2.346350854E+03
2.77364377E+01	2.355238477E+03	6.660941384E+01	2.355333626E+03
2.774355095E+01	2.364189707E+03	7.334132026E+01	2.364323356E+03
2.775061964E+01	2.373141421E+03	8.003071948E+01	2.373319816E+03
2.775764417E+01	2.3820935E+03	8.667796265E+01	2.382322782E+03
2.776462497E+01	2.391045822E+03	9.328339777E+01	2.39133203E+03
2.777156244E+01	2.399998265E+03	9.984736972E+01	2.400347336E+03
1.0			
5.770016181E+01	2.31049386E+03	6.229973366E+01	2.31049386E+03
5.770750435E+01	2.319440843E+03	6.924955528E+01	2.31944654E+03
5.771480015E+01	2.328388917E+03	7.615506589E+01	2.328407084E+03
5.772204967E+01	2.337337961E+03	8.301663271E+01	2.337375264E+03
5.772925333E+01	2.346287855E+03	8.983461974E+01	2.346350854E+03
5.773641157E+01	2.355238477E+03	9.66093877E+01	2.355333626E+03
5.774352482E+01	2.364189707E+03	1.033412941E+02	2.364323356E+03
5.775059351E+01	2.373141421E+03	1.100306933E+02	2.373319816E+03
5.775761804E+01	2.3820935E+03	1.166779365E+02	2.382322782E+03
5.776459884E+01	2.391045822E+03	1.232833716E+02	2.39133203E+03
5.777153631E+01	2.399998265E+03	1.298473436E+02	2.400347336E+03

Test Parameters

In the test simulation, the V-Slit Scanner is fixed and the simulated star light \bar{L} is swept in a horizontal plane, about the vertical \bar{X} Axis. (See Figure 7)

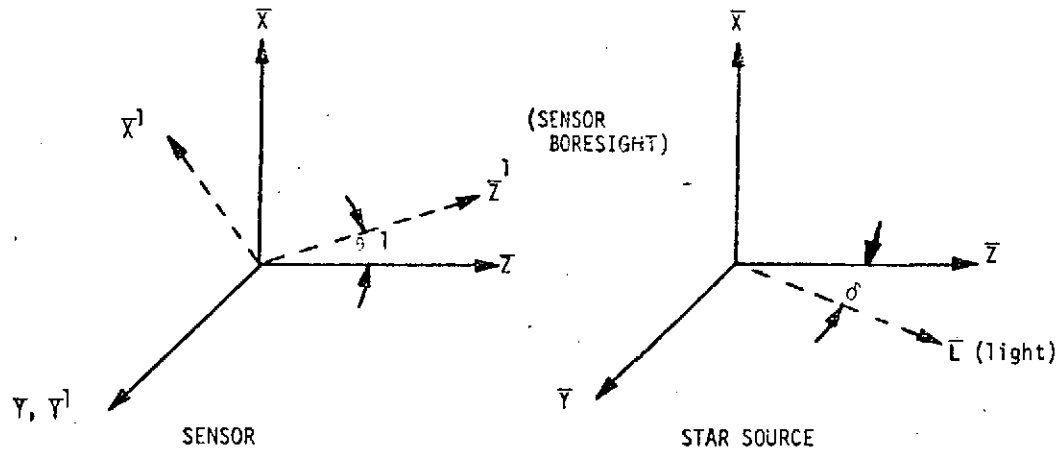


Figure 7. Simulation Geometry

By changing the angle θ of the vertical rotary table different angles between the star line of sight and the spacecraft \bar{Z} axis may be simulated.

$$\begin{bmatrix} \bar{X}' \\ \bar{Y}' \\ \bar{Z}' \end{bmatrix} = \begin{bmatrix} \cos\theta & 0 & -\sin\theta \\ 0 & 1 & 0 \\ \sin\theta & 0 & \cos\theta \end{bmatrix} \begin{bmatrix} \bar{X} \\ \bar{Y} \\ \bar{Z} \end{bmatrix} \quad (5)$$

$$\bar{L} = \bar{Z} \cos\delta + \bar{Y} \sin\delta \quad (6)$$

$$\bar{\theta} = \frac{X_v \bar{X}' + Y_v \bar{Y}' + F \bar{Z}'}{\sqrt{X_v^2 + Y_v^2 + F^2}} \quad (7)$$

Combining equations 5), 6), and 7) -

$$\tan \delta = \frac{Y_v}{F \cos \theta - X_v \sin \theta} \quad (8)$$

$$\tan \theta' = \frac{X_v}{F} \quad (9)$$

For the reference slit, $Y_v = .005''$

$$\tan \delta = \frac{.005}{12 \cos \theta' - X_v \sin \theta'} \quad (10)$$

For the measurement slit -

$$Y_v = .005 + (F \tan \theta' - .3125) \tan 25.9^\circ \quad (11)$$

Substituting equation (11) into equation (8), the boundary for the field of view at the measurement slit may be defined in terms of θ' and δ . Section 11 shows the Fortran Program used to make this computation. The boundary is shown graphically in Figure 8, and is tabulated in Table II.

The time interval between the time that the star image traverses between the two slit fields of view is approximated

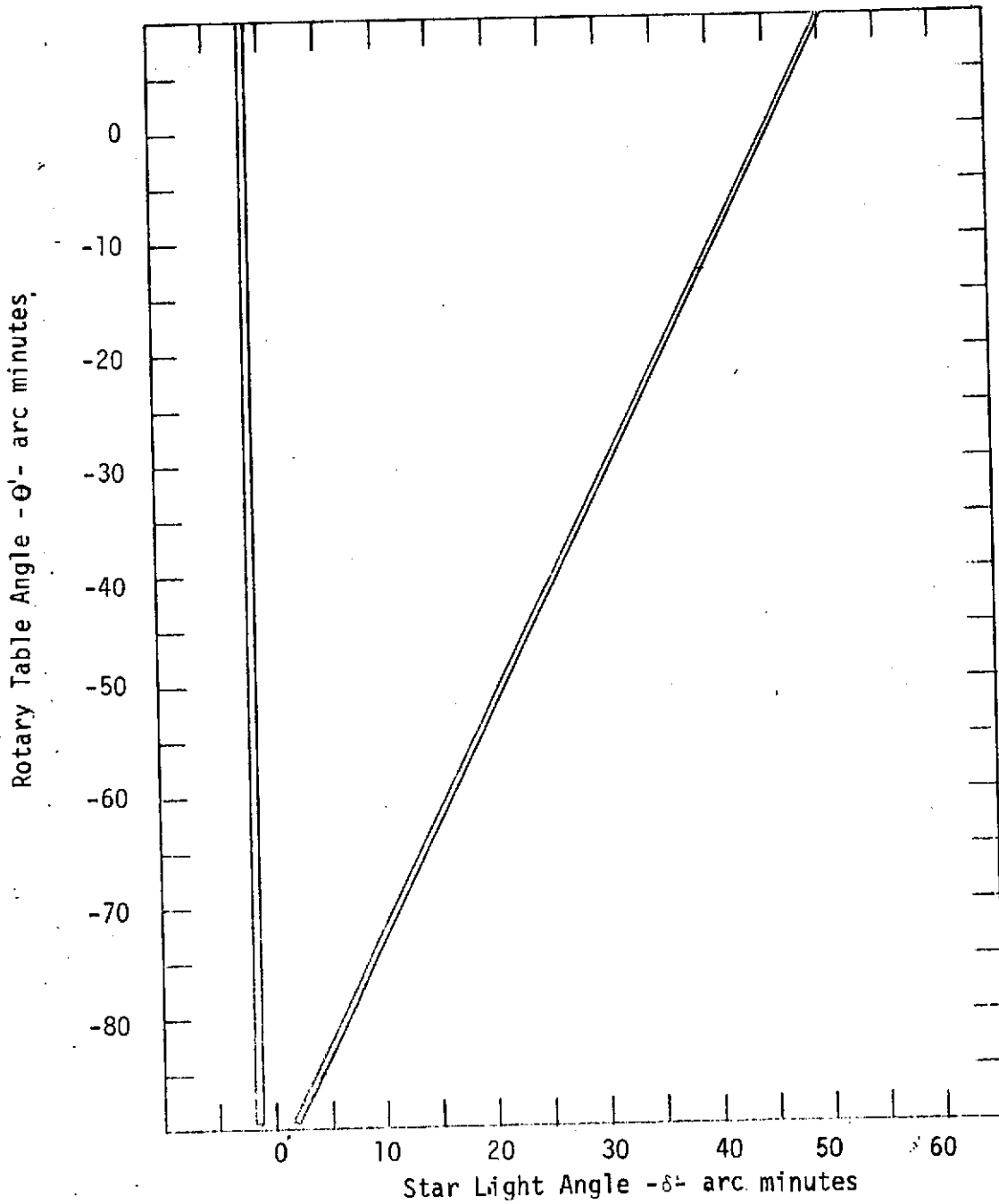


FIGURE 8. FIELD OF VIEW OF 25.9° RETICLE

by

$$T_{SM} - T_{SR} = \frac{\delta_{SM} - \delta_{SR}}{\Delta\delta/\Delta T}$$

$$\approx \frac{2.9 + .486 (\theta' + 89.5)}{\Delta\delta/\Delta T} \text{ sec} \quad (12)$$

Where $\frac{\Delta\delta}{\Delta T}$ = Rotation rate of light beam
in arc min/sec

Table II. Boundary Points for Measurement
Slit Field of View

Measurement Slit	
θ' (Arc Min)	δ (Arc Min)
-8.057226582E+01	5.777068992
-7.161979167E+01	1.012809551E+01
-6.266731771E+01	1.447740644E+01
-5.371484375E+01	1.882531335E+01
-4.476236979E+01	2.317212742E+01
-3.580989583E+01	2.751815951E+01
-2.685742188E+01	3.186372025E+01
-1.790494792E+01	3.620912007E+01
8.952473958	4.055466926E+01
-7.633338406E-13	4.490067807E+01
8.952473958	4.924745674E+01
1.790494792E+01	5.359531556E+01
2.685742187E+01	5.794456496E+01
3.580989583E+01	6.229551554E+01
4.476236979E+01	6.664847814E+01
5.371484375E+01	7.100376394E+01
6.266731771E+01	7.536168445E+01
7.161979167E+01	7.972255164E+01
8.057226562E+01	8.408667798E+01
8.952473958E+01	8.845437647E+01

Now rearranging terms

$$\theta' \approx 2.06 (\Delta\delta/\Delta T) (T_{SM} - T_{SR}) - 95.5 \text{ arc min} \quad (13)$$

By comparing equation (13) with equation (6), it may be noted that the same time interval $(T_{SM} - T_{SR})$ would be generated in the test simulation or in space if -

$$\theta' \approx \beta_V - 2400 \quad \text{arc min} \quad (14)$$

$$\begin{aligned} \Delta\delta/\Delta T &\approx 1160 \text{ arc min/sec} \\ &= 3.24 \text{ rev/min} \end{aligned}$$

Error Summary

Table III lists the major error sources and the timing error associated with each. The table values are based on a simulated spacecraft spin rate of 5 RPM and a boresight cone angle of 40° . This first pulse timing error ΔT_1 may be scaled by $\Delta\alpha_V/\Delta T$ to estimate the expected clock angle error $\Delta\alpha_V$. Similarly by scaling chord error ΔT_C by $\Delta\beta_V/\Delta T$, the expected angle uncertainty $\Delta\beta$ may be calculated.

At 40° angle relative to \bar{Z} Axis

$$\frac{\Delta\alpha_V}{\Delta T} = 30^\circ/\text{sec} = .108 \text{ arc sec}/\mu\text{sec}$$

$$\frac{\Delta\beta_V}{\Delta T} = 2400 \text{ arc min/sec} = .144 \text{ arc sec}/\mu\text{sec}$$

(from Equation 4)

$$\Delta\alpha_V = \underline{5.1} \text{ arc sec}, \quad \Delta\beta_V = \underline{5.5} \text{ arc sec}$$

TABLE III. NOISE ERROR SUMMARY

Error Source	Magnitude Calculation	1σ Error (μ sec of time)	
		1st Pulse	Clord
Test Equipment			
a. Mirror Drive Stability	$\Delta T_c = \frac{300 \text{ counts P/P}}{400,000 \text{ Avg Counts}} \times 3^\circ \tan 25.9^\circ \times 60 \text{ min/deg}$ $/(\sqrt{12} \times .00116 \text{ min/μsec})$ $\Delta T_1 = 300 \times 175,000 \text{ avg count}/400,000 \text{ avg}/\sqrt{12}$	38.0	16.4
b. Clock Frequency Stability	$\Delta T_c = .001\% \times 10^{-2} \times 3^\circ \tan 25.9^\circ \times 60 \text{ min/deg}$ $/.00116 \text{ min/μsec}$ $\Delta T_1 = .001\% \times 10^{-2} \times 175,000 \text{ avg count}$	1.8	.8
c. Clock Resolution	1μ sec	1.0	1.0
d. Threshold Detector	$\Delta T_1 = 20\mu \text{ sec rise time} / 10 \quad (S/N = 10:1)$ $\Delta T_c = \sqrt{2} \times \Delta T_1$	2.0	2.8
Test Equipment RSS Sum (μsec)		38.1	16.6
Sensor			
e. Shot Noise	$\Delta T_1 = 300\mu\text{sec rise time}/13 \quad (S/N = 13:1)$ $\Delta T_c = \sqrt{2} \times \Delta T_1$	23.0	32.6
Data Reduction Statistics		4.5	3.7
f. 100 Sample Uncertainty		47.0	38.5
Total Predicted Uncertainty (μsec)		<u>47.0</u>	<u>38.5</u>

These numbers are well within the 10 arc sec requirements of the work statement. At different sensor boresight angles the expected errors will be different. Consider the case where the boresight angle is 5° . The approximate relationship between star angle β_V and the chord width $T_{SM} - T_{SR}$ for this case may be derived from Figure 9.

$$\beta_V \approx 210 + 432 (T_{SM} - T_{SR}) \text{ arc min} \quad (15)$$

$$\frac{\Delta\beta_V}{\Delta T} \approx 432 \text{ arc min/sec } (.026 \text{ arc. sec}/\mu\text{sec})$$

Thus for a 5° boresight angle, the predicted measurement uncertainties are

$$\Delta\alpha_V = 5.1 \text{ arc sec}, \quad \Delta\beta_V = 1.7 \text{ sec}$$

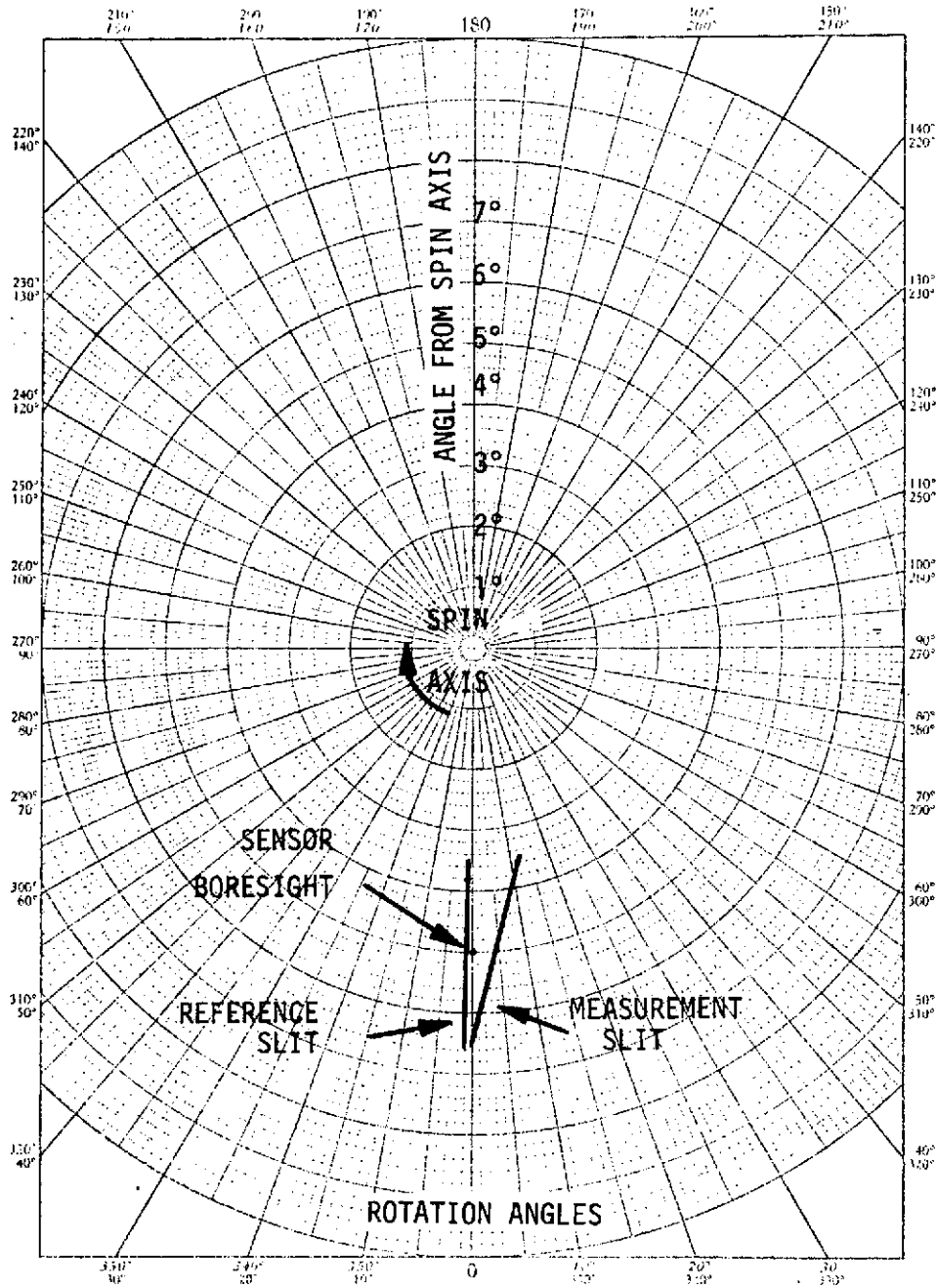


FIGURE 9. Projection of Sensor Field of View for Aperture 5° Off the Spin Axis

SECTION 6

TEST SET

Testing the V-slit star mapper requires that either the sensor is rotated, to simulate spacecraft rotation with respect to a fixed star source, or that the star source is made to sweep past the sensor. The latter implementation was chosen because it is simpler in concept. Also, a test set using this principle was used to test the Stellar Reference Assembly on the Pioneer-Jupiter program, and was made available to the V-slit program.

The test set optical schematic is shown in Figure 10 while the optomechanical portion is outlined in Figure 11. The salient features of the test set are listed in Table IV. The primary hardware elements are -

- a) Two rotary tables: an 18-inch horizontal table and a 9-inch vertical table with a sensor mounting bracket.
- b) Bodine gear motor and controller: 0.3 - 15 rpm continuous adjustment.
- c) Ten-inch diameter encoder plate containing two slits located 90 degrees to each other, to provide reference time signals, and a series of holes for rpm readout.
- d) Detector and light diode assembly with precision adjustment for use as the reference source.
- e) Precision bearing assembly, shaft and rotating mirror assembly.
- f) 12-inch collimator.
- g) Star source. (See Appendix L)

TABLE IV. TEST FEATURES

SIMULATE STAR OR SATELLITE TARGETS BY --

COLLIMATING LIGHT FROM A SMALL ILLUMINATED APERTURE

CHANGING EQUIVALENT STELLAR MAGNITUDE BY VARYING LAMP CURRENT OR ALTERING SOURCE SIZE

SIMULATE SPACECRAFT SPIN MOTIONS BY --

MAINTAINING THE SENSOR FIXED ON A PRECISION 2 AXIS TABLE

SWEEPING THE COLLIMATED LIGHT ACROSS THE SENSOR OPTICS BY ROTATING A MIRROR BETWEEN THE LIGHT SOURCE AND SENSOR

MIRROR RATE IS ADJUSTED TO PROVIDE THE SAME TRANSIT TIME OF THE TARGET IMAGE ACROSS THE SLITS AS EXPECTED IN FLIGHT

SIMULATE DIFFERENCE LOCATIONS OF TARGETS BY --

CHANGING THE HORIZONTAL TABLE ANGLE AS A FUNCTION OF THE DESIRED ROTATION ANGLE

CHANGING THE VERTICAL TABLE ANGLE AS A FUNCTION OF THE DESIRED ANGLE FROM THE \bar{Z} AXIS

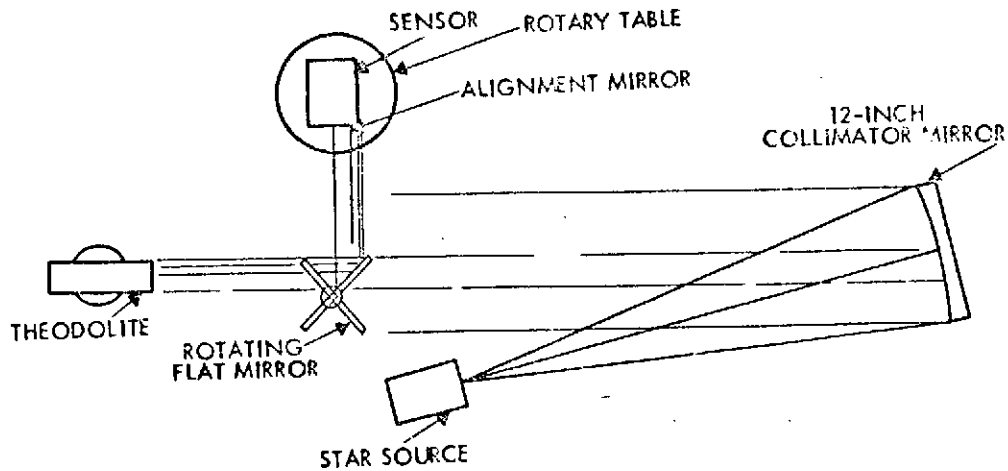


Figure 10. Test Set Optical Schematic

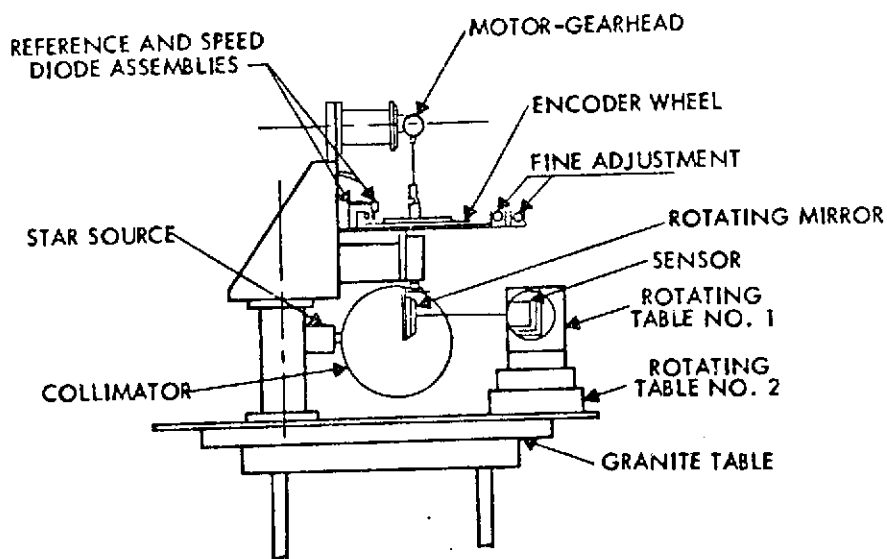


Figure 11. Optomechanical Portion of Test Set

The test set was used in the following manner for testing the Pioneer-Jupiter SRA.

The test set is initially aligned to reflect a collimated beam at 90 degrees to cover the sensor aperture. This is done by positioning a theodolite to face the collimated beam and aligning the star image to coincide with the cross hairs of the theodolite.

The flat mirror assembly is disengaged from the drive motor and adjusted to a position of 90 degrees from the normal star crossing using the second slit on the encoder wheel. The angular difference between the optical star crossing axis and the sensor alignment mirror normal is determined by adjusting the horizontal and vertical rotary tables. The tables are adjusted until autocollimation is achieved by sighting through the previously aligned theodolite to the sensor alignment mirror.

As the flat mirror rotates, the collimated beam crosses the sensor aperture and generates a signal output that starts a counter. The first slit on the encoder wheel passes a detector and light diode assembly, providing a phased-reference signal pulse that stops the counter. This reference signal pulse can be adjusted to coincide with the sensor output pulse. The time jitter between the reference pulse and the sensor pulse provides a measure of the "noise" in clock angle.

The stability of the mirror rotation is measured by another counter which counts the number of reference clock pulses between the first encoder slit to the second encoder slit.

Modification

Modification included the relocation of the second encoder slit so that the mirror rotation stability is measured only over an angle immediately about the sensor pulses. The relocation of the slits is described below in reference to Figure 12.

A1 and A2 are the alignment apertures. The importance of A1 in this discussion is that it is in line with the optical axis, the scan mirror is at 45° to the sensor optical axis and

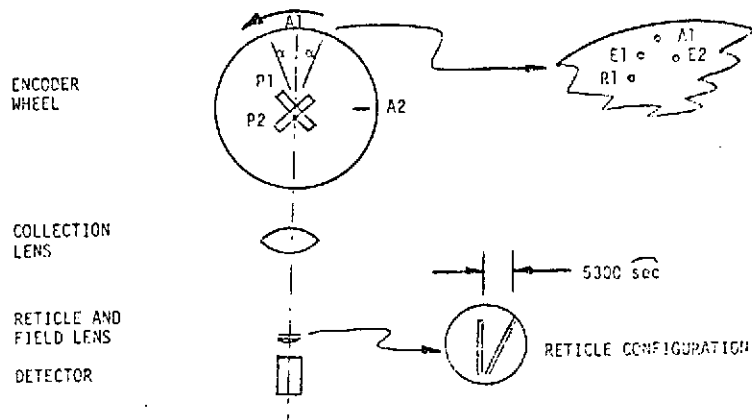


Figure 12. Test Set-Up

the star image falls somewhere between the two slits on the reticle. The maximum angular distance between any slit pair was calculated to be 5300 arc seconds or approximately 1.5° . The aperture which provides a gate pulse to start any counters occurs before A1. The encoder start pulse E1 and the stop pulse E2 were relocated 1° either side of A1. A reset pulse R1 initiated by the aperture R1 was placed about 1° ahead of E1. This arrangement of apertures resulted in the following sequence:

1. Reset pulse (R1) resets counters
2. Encoder pulse (E1) starts counters
3. Encoder pulse (A1) indicates target location
4. Encoder pulse (E2) stops counters

Existing apertures were temporarily blanked out.

Parameters Measured

Upon completion of the modification of the SRA unit, the stability of the scan mirror rotation and the angular wobble in the scan mirror as it scans through 360° were measured. Rotational stability was experimentally determined by using the pulse outputs of the encoder wheel to gate a counter which counted pulses generated by a clock.

Angular wobble was measured in the following way. A plane flat mirror (M1) was mounted normal to the scan axis. Provision was made for adjustment of the mirror. Scan axis wobble would result in a displacement of the mirror M1. Its location was constantly monitored by an automatic two-axis autocollimator. The analog output was periodically recorded over a period of several days to determine the excursion of scan axis wobble, mean and standard deviation. The test block diagram is shown in Figure 13.

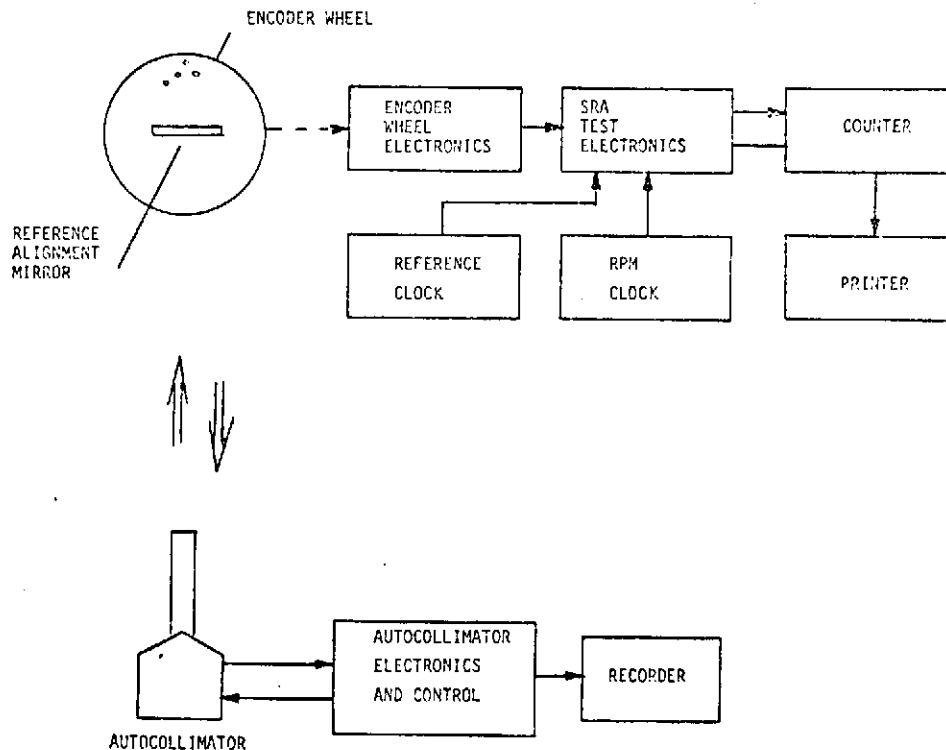


Figure 13. Test Block Diagram

System parameters measured are the following:

- o Sensitivity of the sensor to detect faint star targets
- o RMS noise of sensor system
- o Sensor response to "extended targets" (no larger than 20 arc seconds) having a brightness equivalent of fourth magnitude.

- o Time stability of 1st Pulse
- o Time stability of pulse separation
- o Rotational stability of scan mirror during measurement period

Star targets fourth magnitude and fainter are presented to the V-slit sensor system to determine system sensitivity to point targets. Star luminosity levels are controlled by combinations of apertures and neutral density filters. The star course is calibrated by direct comparison with the NASA/GSFC source which has been calibrated by N.B.S.

Stability of the timing of the two pulses from the V-slit Scanner, are measured in the following manner. Pulse E1 generated by the encoder wheel opens the gate and starts a count on two separate counters (counter 1 and counter 3). The signal S1 which occurs when the target crosses the first slit (threshold detection on leading edge of pulse) stops the count on counter 1 and opens the gate and starts the count on counter 2. The second signal pulse (S2) which occurs when the target crosses the other slit stops the count on counter 2. The second pulse from the encoder wheel (E2) stops the count on counter 3. All counters are reset by the pulse R1 generated by the encoder wheel. The sequential gating of the counters is controlled by the outputs of the logic circuitry which accepts the encoder wheel and

signal pulses as inputs. The clock frequency which is also an input to the logic circuitry is 1 megahertz. This frequency provides a clock accuracy of approximately .04 arc second for the measurement conditions. A block diagram of the test set up and pulse sequence is shown in Figure 14.

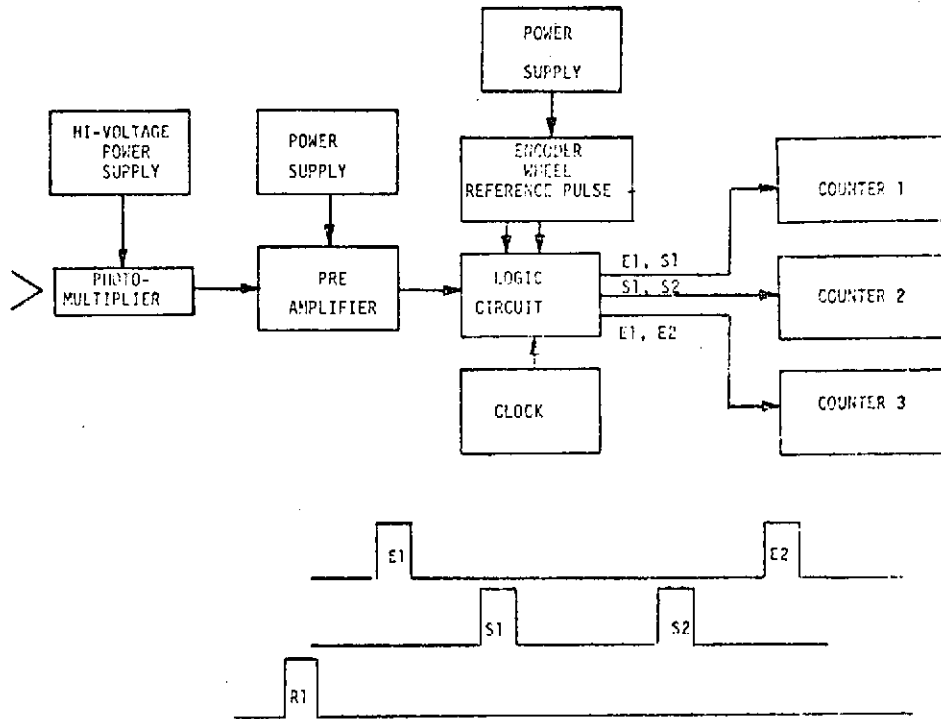


Figure 14. Test Set Block Diagram

Counter number 1, which measures the number of counts occurring between pulse, E1, and the first signal pulse, S1, is

a measure of the rotation angle and its stability. Counter number 2 which counts the number of clock pulses between the two signal pulses is a measure of the angle to the \bar{Z} Axis and its stability. A third measurement which is important to the analysis of the test results is the rotational rate and stability of the scanning mirror. This is derived from the data obtained from counter number 3. The clock pulses measured by counter 3 provide a means of determining scan rate and stability during the measurement period.

The outputs of the counters are sequentially recorded on a digital recorder. In addition, the measured data is computer processed to determine the mean and standard deviation.

SECTION 7

TEST PROGRAM

The test program consisted of checking out the Jupiter Pioneer SRA Test Unit to determine if its performance was within its allotted error budget and testing of the V-slit mapper breadboard. Checkout of the test unit was performed to determine the extent of the angular wobble of the scanning mirror and rotational stability of the scanning mechanism. Measurement of the angular wobble (described in Section 6) proved to be straightforward and no significant problems were encountered. However, the initial measurements of the rotational stability of the scan mirror were unacceptably high. This should not imply that the test unit is inferior in its design. The original stability requirements were that it be better than 1 arc minute, which the initial test measurements showed it to be. Several approaches to improve its performance by mechanical methods failed. The method of improvement which seemed to work best was to drive a high fidelity power amplifier with a precision sine wave generator and transformer couple the Bodine drive motor to the power amplifier. An improvement factor of at least a decade was achieved which improved the rotational stability to an acceptable value of 2-3 arc seconds.

Having determined that the test unit was performing satisfactorily, attention was directed to the testing of the V-slit mapper. All the individual components such as the photomultiplier tube, preamplifier, logic circuitry and encoder wheel pulse generators were checked out in the laboratory prior to the start of the tests. Emulsion reticles of the V-slit were purchased from an outside vendor and visually checked under high magnification upon receipt. Scanner breadboard testing began with

disappointing results. The signal-to-noise ratio was too low thus degrading overall sensor performance. Trouble shooting of the test set up began by checking the logic circuitry to ensure that the counters were being triggered correctly. Output pulses from the encoder wheel and preamplifier were monitored to again check their rise time and amplitude and to ensure that thresholding occurred at the right level. A change in the preamplifier design which resulted in an improvement in sensor performance was a reduction in the bandwidth. Initially the required bandwidth was calculated, increased somewhat and designed into the preamplifier. Due to the problems being experienced during the testing the bandwidth was experimentally adjusted to minimize the noise without seriously affecting the signal. The experimentally determined bandwidth is 2 kilohertz. The reduction in bandwidth did not improve system performance to a satisfactory level. Satisfied that the electronics were optimized, attention was then directed to the optical performance of the sensor. Alignment and focus were checked and verified. The one remaining item which remained was the reticle.

A measurement of sensor transmission with and without the reticle showed that at least 85% of the light was being lost at the reticle. The focus of the entire system with and without the reticle was visually made to see if the star image fell within the reticle slit. Two independent observations were made and the same conclusion reached. The star image did fall within the slit. The vendor who supplied the reticles was contacted and advised of the optical transmission problem being experienced. They suggested two approaches: "bleaching" the clear area of the emulsion reticles and changing the reticle to a chrome reticle. It was decided to do both. "Bleaching" increased the signal by about 50% but that was still inadequate. A significant increase in

signal level was achieved when the chrome reticle was used since only losses due to the glass were present. Signal current at the photomultiplier was now determined to be approximately 50 nanoamperes. Since a current level of about 150 nanoamperes was expected, further improvements remained to be made. However, due to time limitations it was decided to measure sensor performance under the existing test conditions. The results of the tests are presented in the following section.

SECTION 8
TEST RESULTS

Data from the counters were recorded and sample sizes of 100 points operated on to determine the mean and standard deviation. Initial analysis of the data showed that the 1 sigma variations of the (E1 - S1) and (S1 - S2) counts were larger than expected when compared to the 1 sigma value for the RPM counts. A closer look at this data showed a long term cyclical variation which might not be related to the SRA test set up. (Fig. 15) The source of the variation is suspected to be due to problems in the electronics, specifically threshold stability. To account for this long term variation, it was decided to divide each group of 100 samples into groups of 10 samples, determine the 1 sigma value of the smaller groups and then rss these 1 sigma values to obtain a 1 sigma value representative of the 100 sample size. Table V summarizes the raw test data collected. Two reticles, 10° and 25.0°, were used during the test. The angle σ represents the excursion of the cone angle, i.e. data was collected for the star target crossing the top of the slits and the bottom of the slits. (The total field of the sensor was measured to be slightly less than 3°.) One sigma value (σ), mean count (μ), and sample size (N) are listed for each measurement condition.

Table VI summarizes the results of the data reduction for the 10° and 25.9° reticle. E1 - S1 timing data was scaled by the scan rate 3.84 RPM to obtain the 1st pulse angle entries. Similarly, the S1 - S2 timing data was scaled to get $\Delta\zeta$. Note that the $\pm 1\sigma$ uncertainties in ζ and $\Delta\zeta$ are less than 14.4 arc seconds for the 4.9 magnitude star and less than 9.7 arc seconds

FIGURE 15. TYPICAL TIME VARIATION
OF SIGNAL AND SCAN MIRROR
10° RETICLE

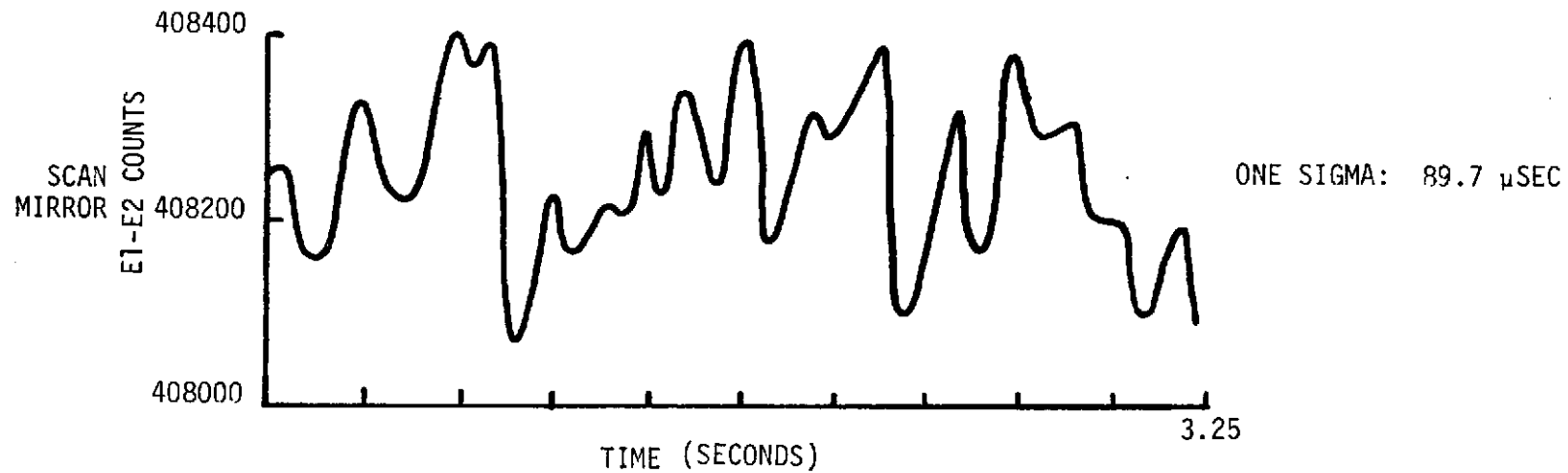
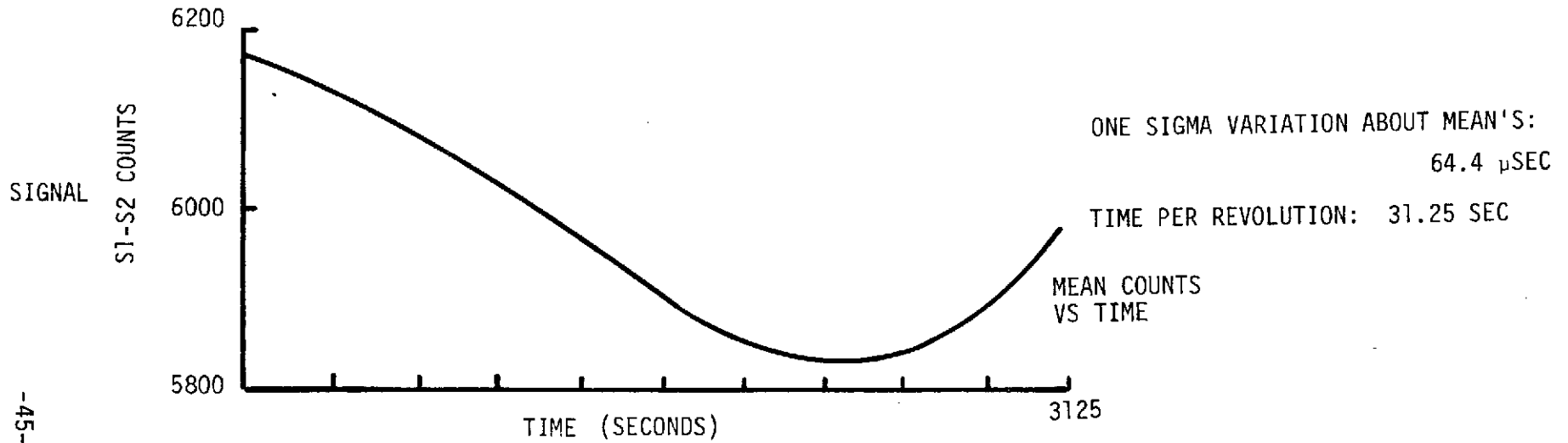


TABLE V TEST DATA SUMMARY

<u>Reticle</u>	<u>Angle</u> σ'	<u>Parameter</u>	<u>RPM</u>	<u>E1 - S1</u>	<u>S1 - S2</u>
10°	~-1.5°	σ	89.7	137.0	64.4
		μ	408244	168118	5992
		N	100	100	100
	~+1.5°	σ	98.0	149.6	126.8
		μ	408166	164855	24076
		N	100	100	100
25.9°	~-1.5°	σ	93.4	107.3	121.3
		μ	408178	155110	7170
		N	100	100	100
	~+1.5°	σ	88.5	121.0	174.0
		μ	408144	153220	57991
		N	100	100	100

Note: 1) The simulated star magnitude was 4.9 for this test ($31 \times 10^{-15} \text{A}$ vs $72 \times 10^{-15} \text{A}$)

2) Mean and standard deviations are indicated in μ seconds units.

3) Conditions

Tube Voltage: 1810 volts

Scan Rate: 3.84 RPM optical

Anode Current: 50 ηA peak

Source Aperture: .002 in diameter (8.5 arc sec)

TABLE VI DATA REDUCTION SUMMARY

<u>Reticle</u>	<u>Angle</u> σ	<u>1st Pulse</u> <u>δ Angle</u> <u>(Arc Sec)</u>	<u>Pulse Pair</u> <u>Separation $\Delta\delta$</u> <u>(Arc Sec)</u>	<u>Extrapolated Performance</u>			
				$\theta_{\beta v} = 40^\circ$		$\theta_{\beta v} = 5^\circ$	
				<u>σ_α</u>	<u>σ_β</u>	<u>σ_α</u>	<u>σ_β</u>
10°	~ - 1.5°	14,000 \pm 11.4	497 \pm 5.4	14.8	24.0	14.8	4.3
	~ 1.5°	13,750 \pm 12.4	2010 \pm 10.6	16.2	47.0	16.2	8.5
25.9°	~ - 1.5°	12,950 \pm 8.9	598 \pm 10.1	11.6	17.4	11.6	3.2
	~ 1.5°	12,750 \pm 10.1	4810 \pm 14.4	13.0	25.0	13.0	4.5

-47-

- Note: 1) Errors would be reduced by approximately 1.5x, if a 4th magnitude star were observed rather than the 4.9th magnitude. (Errors $\propto \sqrt{1/N_{\Delta t}}$ per Page 15)
- 2) Further improvement by a factor of approximately 1.3 may be obtained by using a 4" diameter lens rather than 3".
- 3) Averaging of data from the sensor over a one minute period would further reduce the rms deviation by $\sqrt{5}$.

for the 4th magnitude star. The equivalent system errors in the measurement of rotation angle ζ_s and the angle β_s between the apparent line of sight to the star and the \bar{Z} axis, are 8.7 arc seconds and 17 arc seconds worst case, respectively. (Assuming 40° sensor boresight angle, 25.9° reticle, 4th magnitude star.)

These performance numbers, 8.7 to 17 arc seconds, are not as good as predicted in the Section 5 Analysis, indicating that the test set errors were probably under estimated. Instead of the test set errors being in the ± 3 arc second range, they are more likely in the ± 9 arc second range.

The 4.9 Mv star used in the tests results from the need to keep the angular subtense of the star source at 20 arc seconds or less. Since the source is calibrated at a fixed filament current, the only way to change star brightness is by changing the size of the pinhole aperture. Thus, with the maximum aperture usable to meet the 20 arc second requirement the extrapolated stellar magnitude was 4.9.

SECTION 9
CONCLUSIONS

Test results have shown that 10 arc second level repeatability is achievable using a relatively simple sensor configuration. Analysis results show how the sensor errors translate into measurement errors relative to spacecraft axes. Better system accuracy is obtained by using reticles with a cant angle, between the slits, of 25.9° or more. This improvement in the angle (β) measurement comes about from the larger $\Delta\alpha/\Delta\beta$ sensitivity factor. Similarly, improved performance would be expected when the sensor axis is directed closer to the spin axis, since $\Delta\alpha/\Delta\beta$ is again larger. However, the apparent size of the target gets magnified near the spin axis and introduces more errors. For example, a 20 arc second target image at a distance of 5° from the spin axis would completely translate past one slit edge over a clock angle (α) rotation interval of about 200 arc seconds. For small images, resulting from negligible lens aberrations and star or distant satellite targets, the accuracy would improve for sensor boresights near the spin axis.

Any further studies of the basic concept should consider the stray light interference from the sun or planets when they are near the target star or satellite. Possible configurations for the required structure or intercavity region should be investigated. TRW has previously looked at a photon counting scheme for processing star sensor information that allows the use of a much smaller collecting aperture. This feature allows the use of a smaller shade or allows the sensor to operate closer to sources of interference for the same shade volume. The photon counting scheme should be included in future studies of the star mapper if satellite detection, as well as star detection, is required.

SECTION 10

REFERENCES

1. "Advanced Pioneer Planetary Probe Mission Guidance and Navigation Requirements", Jet Propulsion Laboratory Report No. 760-88, 15 November 1973, by C. K. Paul, R. K. Russell, J. Ellis.
2. "Saturn Uranus Atmospheric Entry Probe Mission, Spacecraft System Definition Study", TRW report 23267-6001-RU-00, July 15, 1973, under Contract No. NAS2-7297 to NASA Ames Research Center.
3. Calibration Procedure, Pioneer F/G Stellar Reference Assembly Unit Test Set.
4. Forbes, F. F. and Mitchell, R. I., "No. 141 Stellar Photometric Data for Six Different Photocathode Materials and the Silicon Detector", Communications of the Lunar and Planetary Laboratory, University of Arizona, 1968.
5. Allen, C. W., "Astrophysical Quantities", London, The Athlone Press, 1964.

SECTION 11

APPENDICES

- A Properties of the V-Slit Reticle
- B Use of a Field Lens in the V-Slit Scanner
- C The Waveform of a Slit Transiting a Disk
- D The Effect of the General Stellar and Nonstellar Background on Signal-to-Noise and the True and False Detection Probabilities of the V-Slit Scanner
- E The Energy and Photon Flux and Apparent Magnitude of a Solar System Object View from an Arbitrary Location
- F Minimum Allowable Slit Width
- G The Detection Statistics in Flight
- H Photomultiplier Data Sheet
- J Computer Programs
- K Slit Reticle Drawing
- L Star Sources and Spectral Calibration

APPENDIX A

PROPERTIES OF THE V-SLIT RETICLE

The response expected from a generally defined V-slit reticle has been examined with regard to both the cone and clock angles. It is found that if the sensor is to be used at small cone angles the apex of the V-slit should be oriented away from the satellite spin axis to avoid cone angle ambiguity. Equations relating the clock and cone angles to observables are derived as are expressions giving the cone and clock angle errors in terms of system tolerances.

Consider a slit mounted on a gimbaling arm as in Figure A-1.

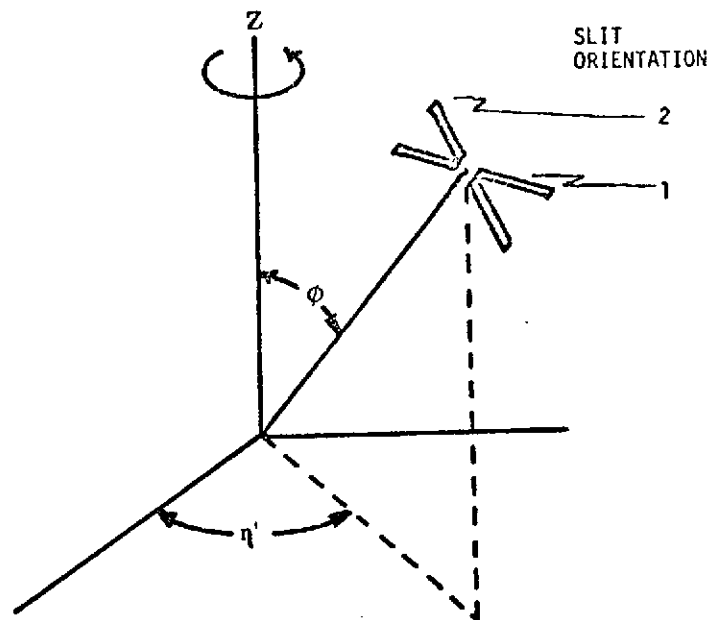


FIGURE A-1. - Gimbal Parameters

Examine the situation of the two possible slit orientations (i.e. 1 and 2) when ϕ is small.

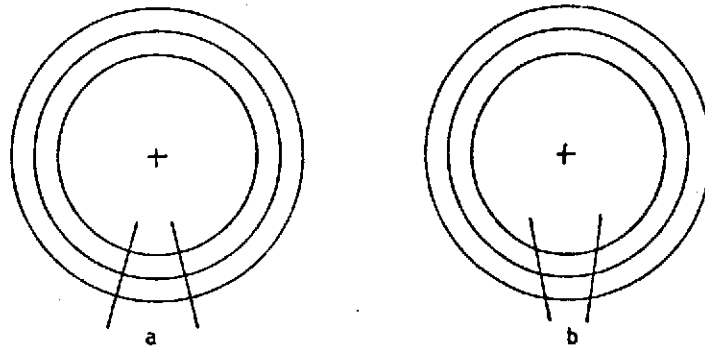


FIGURE A-2. - Slit-Target Orientations

In Figure A-2-a the spin axis is at the apex of the V-slits (extended) which means that no cone angle can be measured since all targets take the same time to traverse the space between the slits. This difficulty does not occur with the orientation shown in Figure A-2-b, therefore the preferred orientation is with the apex of the V-slits away from the spin axis.

In Figure A-3 one sees the geometry pertaining to a generally defined V-slit.

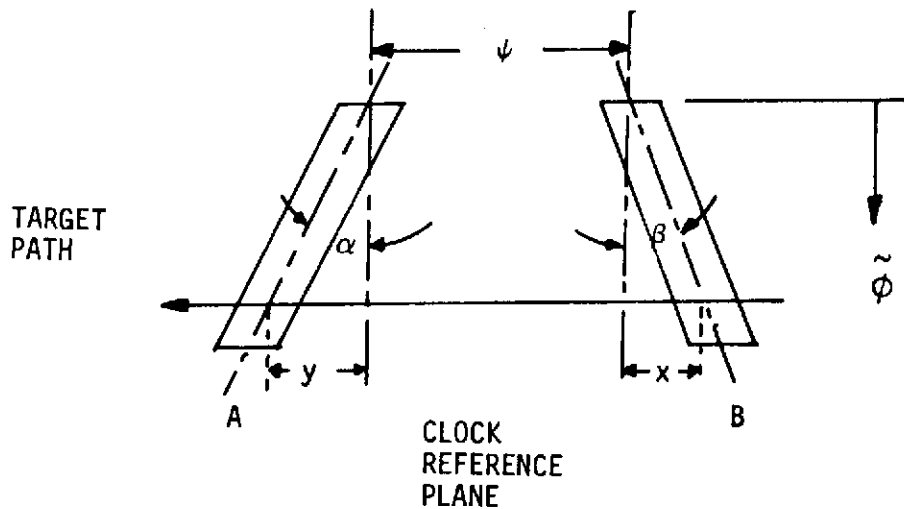


FIGURE A-3. - Slit Geometry Parameters

The V-slit is in the $\tilde{\phi}$ reference frame where $\tilde{\phi} = 0$ at the slit apex and is colinear with and increases in the same sense as ϕ . The slits are canted by angles α and β with respect to the clock reference plane and their tops are separated by an angular distance ψ (a function of the optics focal length and the linear separation of the slits). By inspection the total angular distance between slit centers for a target at $\tilde{\phi}$ is given by

$$d = \tilde{\phi} (\tan \alpha + \tan \beta) + \psi \quad (1)$$

Letting τ be the observed time of transit between slit centers one may write

$$\tilde{\phi} (\tan \alpha + \tan \beta) + \psi = \omega \tau \sin (\phi + \tilde{\phi}) \quad (2)$$

where $\omega \equiv$ spacecraft rotational velocity.

Noting that $\tilde{\phi} \leq 3^\circ$ for the proposed v-slit one may write

$$\tilde{\phi} (\tan \alpha + \tan \beta) + \psi = \omega \tau \left(\left(1 - \frac{\tilde{\phi}^2}{2}\right) \sin \phi + \tilde{\phi} \cos \phi \right) \quad (3)$$

Linearizing in $\tilde{\phi}$ and rearranging yields

$$\tilde{\phi} = \frac{\omega \tau \sin \phi - \psi}{\tan \alpha + \tan \beta - \omega \tau \cos \phi} \quad (4)$$

Thus the cone angle is determined solely by observing the target transit time, the other quantities of equation (4) being known a priori.

Errors in $\tilde{\phi}$ are determined by the non-zero tolerances in the various constituents of $\tilde{\phi}$, which may be evaluated by employing the following rule:

$$d\tilde{\phi} = \sum_i \frac{\partial \tilde{\phi}}{\partial q_i} dq_i \quad q = \omega, \tau, \phi, \psi, \alpha, \beta \quad (5)$$

The partial derivatives are given in Table A-1.

TABLE A-1. - Cone Angle Derivatives & Parameters

q	$\partial \tilde{\phi} / \partial q$	
ψ	$\frac{1}{\tan \alpha + \tan \beta - \omega \tau \cos \phi}$	(6)
α	$\frac{\sec^2 \alpha (\psi - \omega \tau \sin \phi)}{(\tan \alpha + \tan \beta - \omega \tau \cos \phi)^2}$	(7)
β	$\frac{\sec^2 \beta (\psi - \omega \tau \sin \phi)}{(\tan \alpha + \tan \beta - \omega \tau \cos \phi)^2}$	(8)
ω	$\frac{\tau (\sin \phi (\tan \alpha + \tan \beta) - \psi \cos \phi)}{(\tan \alpha + \tan \beta - \omega \tau \cos \phi)^2}$	(9)
τ	$\frac{\omega (\sin \phi (\tan \alpha + \tan \beta) - \psi \cos \phi)}{(\tan \alpha + \tan \beta - \omega \tau \cos \phi)^2}$	(10)
ϕ	$\frac{\omega \tau (\cos \phi (\tan \alpha + \tan \beta) + \psi \sin \phi - \omega \tau)}{(\tan \alpha + \tan \beta - \omega \tau \cos \phi)^2}$	(11)

The time at which the target crosses the clock reference plane (t_{clock}) and establishes the clock angle is related to the time of detection in slit B (t_B) in the following way.

$$t_{\text{clock}} = t_B + \frac{\tilde{\phi} \beta}{\omega \sin(\phi + \tilde{\phi})} \quad (12)$$

Employing the method of equation (5) the error in t_{clock} due to constituent uncertainties may be written as

$$\begin{aligned} dt_{\text{clock}} = dt_B + \frac{\tilde{\phi} d\beta}{\omega \sin(\phi + \tilde{\phi})} - \frac{\tilde{\phi} \beta \sin(\phi + \tilde{\phi}) d\omega}{(\omega \sin(\phi + \tilde{\phi}))^2} - \frac{\tilde{\phi} \beta \cos(\phi + \tilde{\phi})}{\omega \sin^2(\phi + \tilde{\phi})} d\phi \\ + \beta \frac{(\sin(\phi + \tilde{\phi}) - \tilde{\phi} \cos(\phi + \tilde{\phi}))}{\omega \sin^2(\phi + \tilde{\phi})} d\tilde{\phi} \end{aligned} \quad (13)^*$$

From this expression one sees that unless prohibited by other circumstances, β should be set to zero to minimize the errors of t_{clock} .

The time of detection, t_B , is itself a function of a number of parameters and may be expressed as:

$$t_B = t_{1,B} + \frac{\gamma \xi(\theta, \frac{\gamma'}{\gamma})}{\omega \sin(\phi + \tilde{\phi})} \quad (14)$$

where γ = angular size of target

$\xi(\theta, \frac{\gamma'}{\gamma})$ correction for viewing aspect

θ = aspect angle

γ' = angular size of slit

$t_{1,B}$ = time of detection of the light center in slit B

Differentiating (14) yields:

$$dt_B = dt_{1,B} + \frac{1}{\omega \sin(\phi + \hat{\phi})} \left[\xi d\gamma - \frac{\gamma \xi}{\omega} d\omega + \gamma d\xi - \frac{\gamma \xi (\cos(\phi + \hat{\phi}))}{\sin(\phi + \hat{\phi})} (d\phi + d\hat{\phi}) \right] \quad (15)^*$$

which may be employed in equation (13).

*Where random errors are desired the following expression would be used rather than Equation (5):

$$dP^2 = \sum_i \left(\frac{\partial P}{\partial q_i} \right)^2 dq_i^2$$

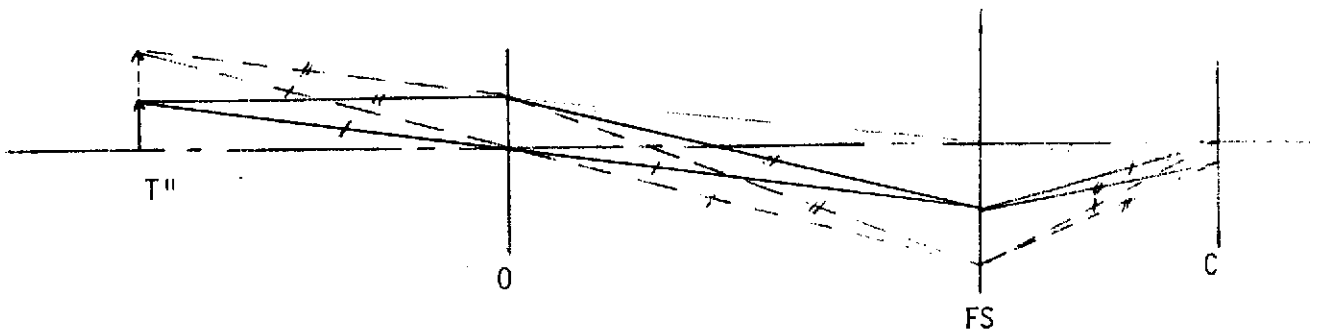
APPENDIX B

USE OF A FIELD LENS IN THE V-SLIT SCANNER

The optical feeding of a V-slit scanner involves the imaging of a target on a slit reticle and the subsequent observation of the spatially filtered image by a photocathode. In such a system, motion of the target results in motion of the image on the photocathode which in turn may result in additional noise due to nonuniformities in the cathode surface. This type of noise may be eliminated, however, if the image position on the cathode can be rendered independent of target motion. It is shown that this may be accomplished by use of a field lens (FL), and the characteristics of a lens applicable to the V-slit scanner are derived. Suggestions for the imaging optics and mounting of the lens are presented.

PROPERTIES OF THE REQUIRED FIELD LENS

The position of the target image on the photocathode may be decoupled from the target's motion by imaging the objective surface onto the cathode as shown in Figure 1.



C = Cathode
FS = Field-Lens & Slit
T'' = Target
O = Objective

FIGURE B-1. - Optical System Schematic

From Figure B-1 it is seen that each image point on the cathode contains full information on the target and that motion of the target from the solid position to the dotted position does not effect the intersection of the I and II rays with the cathode. Since nothing has been assumed regarding the details of the FL, one concludes that any lens which images the objective onto the cathode will decouple the image position from target motion.

FIELD LENS FOR THE V-SLIT SCANNER

By letting the FL be plano-convex it is possible to deposit the V-slit reticle directly on the face of the lens and thus eliminate any possible lens-reticle alignment problems and minimize the number of mounting structures required. The V-slit objective optics has a nominal focal length of 12", allowing one to write the thin lens equation for the FL as:

$$1/12 + 1/i = \frac{1 - N}{r''} \quad (1)$$

where i = image distance
 N = index of refraction
 r'' = radius of curvature (negative for a convex surface)

letting $i \approx 1''$ and $N = 1.5$ one finds

$$r'' = -.46''$$

The required diameter of the lens is determined by the diameter of the objective image field, which for a 3° field-of-view and a 12" focal length is .629". A scale drawing of the suggested FL is found in Figure B-2.

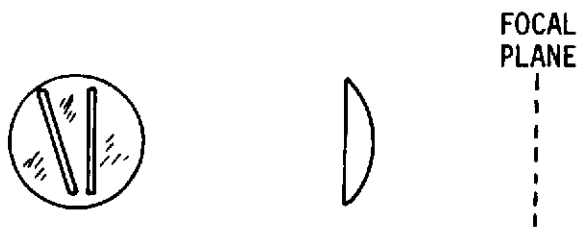


FIGURE B-2.
Field Lens Schematic

For ease of mounting and alignment of the FL a Cassegrain system with a flat secondary, as shown in Figure B-3, is suggested for future flight application.

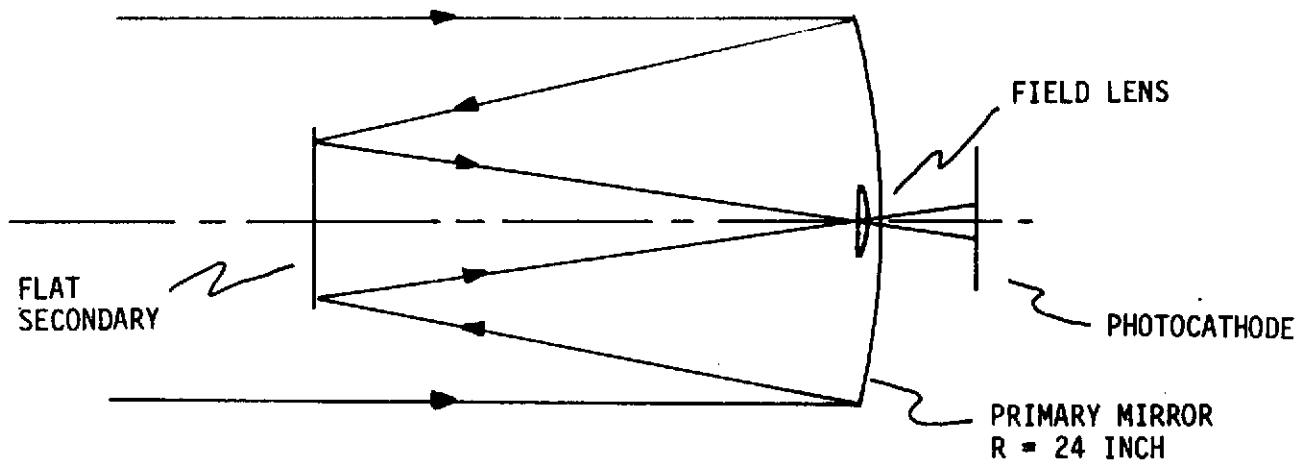


FIGURE B-3 - Cassegrain V-slit Schematic

Here it is seen that the FL mounts directly into the Cassegrain hole of the primary. It should be noted that the diameter of the primary mirror need be only 1.15 times as large as the diameter of a clear aperture objective lens to yield the same effective aperture. In the case of the V-slit system this allows one to replace the 3.5" objective lens with a 4.04" mirror.

APPENDIX C

THE WAVEFORM RESPONSE OF A SLIT TRANSITING A DISK

The use of a slit scanner for navigation requires that the output signal be interpreted to yield the physical centroid of the observed object. In the case of stars and other uniform, actively shining, objects this is done simply by identifying the position of maximum output. However, for objects such as satellites, asteroids, etc., which shine passively, the location of maximum output will in general not correspond to the physical center of the body. Since a V-slit scanner has been proposed for use in the terminal navigation maneuvers of the outer planets missions, it is of interest to define the relation between scanner output and object centroid as it depends on relative slit and image size, satellite aspect angle, etc. To this end the passage of slit of arbitrary width both normal and parallel to the terminator has been studied. The case of arbitrary slit orientation has not been examined due to its mathematical complexing and the fact that it must be intermediate between the aforementioned cases.

It has been found that the optimum spatial resolution occurs for a slit width on the order of the size of the feature to be detected, e. g. for an aspect angle of 120° (one quarter crescent phase), the optimum slit width would be one-half of the disk radius. Slits larger than the characteristics scale result in waveforms with zones of constant response, while those of smaller size tend to flatten the response and thereby reduce the prominence of the maximum point. Either of these situations introduces uncertainty into the identification of the maximum.

For slit widths less than the disk diameter it has been found that the spatial difference between the light maximum and the physical center of the object is a function of aspect angle and slit width. The narrower the slit the smaller the difference for gibbous phases but the larger the difference for crescent phases. This fact results in tradeoff possibilities between optimizing the light maximum detectability and the correction which must be applied to determine the objects physical center.

Later memoranda will examine optimum signal processing philosophies.

2. ANALYTIC DESCRIPTION OF A SLIT CROSSING A DISK

2.1 Slit Normal to Illumination Vector, Aspect $\theta < \pi/2$

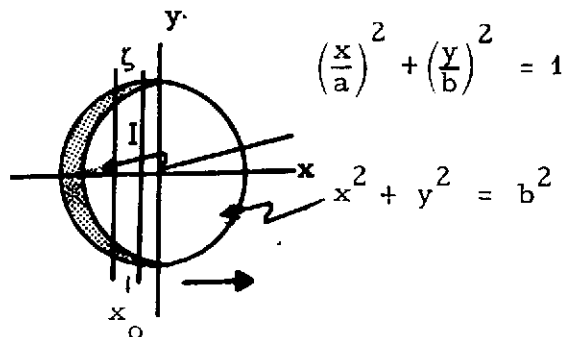


Figure 1

$$y_c = (b^2 - x^2)^{1/2} \quad (1)$$

$$y_e = \frac{b}{a}(a^2 - x^2)^{1/2}$$

Let the center of the slit be at x_0 and the edges of the slit be at $x_0 - \zeta/2$ and $x_0 + \zeta/2$.

The illuminated portion of the disk within the slit may in general be written as

$$A = 2 \int_{\alpha'}^{\beta'} \frac{b}{a}(a^2 - x^2)^{1/2} dx + 2 \int_{\gamma'}^{\delta'} (b^2 - x^2)^{1/2} dx \quad (2)$$

where α' , β' , γ' , δ' are determined by the details of the slit location as described below. Integration of equation (2) produces.

$$I_i = \left[\frac{b}{a} \beta (a^2 - \beta^2)^{1/2} - \alpha (a^2 - \alpha^2)^{1/2} + a^2 \left(\sin^{-1} \frac{\beta'}{a} - \sin^{-1} \frac{\alpha'}{a} \right) \right] \quad (3)$$

$$+ \delta (b^2 - \delta^2)^{1/2} - \gamma (b^2 - \gamma^2)^{1/2} + b^2 \left(\sin^{-1} \frac{\delta'}{b} - \sin^{-1} \frac{\gamma'}{b} \right)$$

α' , β' , γ' , and δ' take values as follows:

Table 1

For $x_0 - \xi/2 < -a$

$-a \leq x_0 + \xi/2 \leq 0$	$0 \leq x_0 + \xi/2 \leq b$	$x_0 + \xi/2 > b$
$\beta' = x_0 + \xi/2$ $\alpha' = -a$	$\beta' = 0$ $\alpha' = -a$	$\beta' = 0$ $\alpha' = -a$
$\delta' = 0$ $\gamma' = 0$	$\delta' = x_0 + \xi/2$ $\gamma' = 0$	$\delta' = b$ $\gamma' = 0$

For $-a \leq x_0 - \xi/2 \leq 0$

$x_0 + \xi/2 < 0$	$0 \leq x_0 + \xi/2 \leq b$	$x_0 + \xi/2 > b$
$\beta' = x_0 + \xi/2$ $\alpha' = x_0 - \xi/2$	$\beta' = 0$ $\alpha' = x_0 - \xi/2$	$\beta' = 0$ $\alpha' = x_0 - \xi/2$
$\delta' = 0$ $\gamma' = 0$	$\delta' = x_0 + \xi/2$ $\gamma' = 0$	$\delta' = b$ $\gamma' = 0$

For $0 \leq x_0 - \xi/2 \leq b$

$x_0 + \xi/2 < b$	$x_0 + \xi/2 > b$
$\beta' = 0$ $\alpha' = 0$	$\beta' = 0$ $\alpha' = 0$
$\delta' = x_0 + \xi/2$ $\gamma' = x_0 - \xi/2$	$\delta' = b$ $\gamma' = x_0 - \xi/2$

2.2 Slit Normal to Illumination Vector, Aspect $\pi/2 \leq 0 \leq \pi$

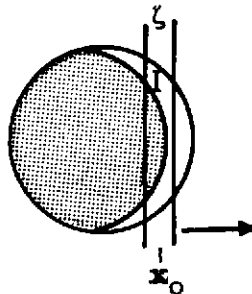


Figure 2

Referring to equations (1), one sees that the general expression for the illuminated area may be written as:

$$I_{ii} = 2 \int_{\alpha'}^{\beta'} (b^2 - x^2)^{1/2} - \frac{b}{a}(a^2 - x^2)^{1/2} dx + 2 \int_{\gamma'}^{\delta'} (b^2 - x^2)^{1/2} dx \quad (4)$$

The limits of integration are defined below. Integration of equation (4) yields:

$$\begin{aligned} I_{ii} = & \beta(b^2 - \beta^2)^{1/2} - \alpha(b^2 - \alpha^2)^{1/2} + \delta(b^2 - \delta^2)^{1/2} - \gamma(b^2 - \gamma^2)^{1/2} \\ & + b^2 \left(\sin^{-1} \frac{\beta}{b} - \sin^{-1} \frac{\alpha}{b} + \sin^{-1} \frac{\delta}{b} - \sin^{-1} \frac{\gamma}{b} \right) \\ & + \frac{b}{a} \left[\alpha(a^2 - \alpha^2)^{1/2} - \beta(a^2 - \beta^2)^{1/2} + a^2 \left(\sin^{-1} \frac{\alpha}{a} - \sin^{-1} \frac{\beta}{a} \right) \right] \end{aligned} \quad (5)$$

α' , β' , γ' and δ' take values as follows

Table 2

For $x_0 - \xi/2 < 0$

$0 \leq x_0 + \xi/2 \leq a$	$a \leq x_0 + \xi/2 \leq b$	$x_0 + \xi/2 > b$
$\beta' = x_0 + \xi/2$ $\alpha' = 0$	$\beta' = a$ $\alpha' = 0$	$\beta' = a$ $\alpha' = 0$
$\delta' = 0$ $\gamma' = 0$	$\delta' =$ $\gamma' = a$	$\delta' = b$ $\gamma' = a$

For $0 < x_0 - \xi/2 < a$

$x_0 + \xi/2 < a$	$x_0 + \xi/2 > a$	$x_0 + \xi/2 > b$
$\beta' = x_0 + \xi/2$ $\alpha' = x_0 - \xi/2$	$\beta' = a$ $\alpha' = x_0 - \xi/2$	$\beta' = a$ $\alpha' = x_0 - \xi/2$
$\delta' = 0$ $\gamma' = 0$	$\delta' = x_0 + \xi/2$ $\gamma' = a$	$\delta' = b$ $\gamma' = a$

For $a < x_0 - \xi/2 \leq b$

$x_0 + \xi/2 \leq b$	$x_0 + \xi/2 > b$
$\beta' = 0$ $\alpha' = 0$	$\beta' = 0$ $\alpha' = 0$
$\delta' = x_0 + \xi/2$ $\gamma' = x_0 - \xi/2$	$\delta' = b$ $\gamma' = x_0 - \xi/2$

2.3 Slit Parallel to Illumination Vector, Aspect $\theta < \pi$

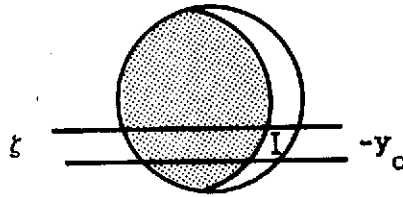


Figure 3

Noting that $a = -b \cos\theta$

Equations (1) may be rewritten as

$$\begin{aligned} x_c &= (b^2 - y^2)^{1/2} \\ x_e &= -\cos\theta (b^2 - y^2)^{1/2} \end{aligned} \tag{6}$$

whereupon

$$I_{iii} = (1 + \cos\theta) \int_{y'}^{\delta y} (b^2 - y^2)^{1/2} dy \tag{7}$$

Comparing this expression with that for I_i one sees that if $y_{o, iii} = x_{o, i}$, and if in case i, $a = b$, that one may write

$$I_{iii} = \frac{(1 + \cos\theta)}{2} I_i \left| \begin{array}{l} a = b \\ y_{o, iii} = x_{o, i} \end{array} \right.$$

Thus for a "parallel" transit the effect of aspect angle is merely to directly scale the total area of the disk appearing within the slit.

3. EVALUATION OF THE ANALYTIC DESCRIPTION

The equations of cases i and ii have been evaluated for $b = 1.0$ and for various aspect angles and slit widths. Figure 4 presents the waveform observed for slits of various widths (z) transiting a zero aspect angle disk. The second half of the passage has been deleted due to symmetry. Here one sees that optimum peak resolution and amplitude

is achieved for $\zeta = 2$, i. e., a slit width equal to the characteristic scale of the object. For larger slits, e. g., $\zeta = 4$, the amplitude is preserved but a constant response zone develops whose length increases directly with slit width. In the case of smaller slit widths one finds that the maximum amplitude attained is reduced and that the position of maximum becomes progressively less pronounced.

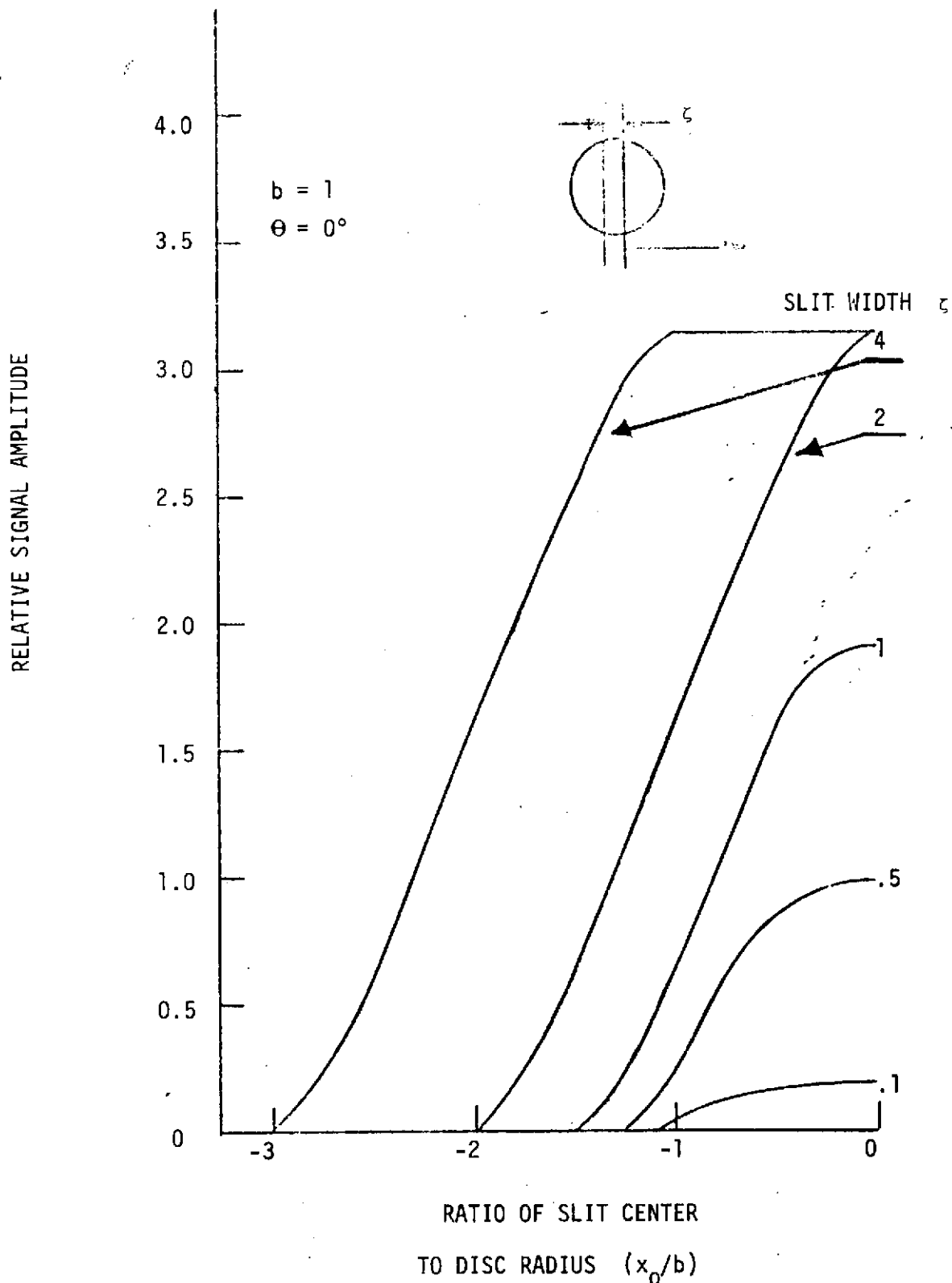
In Figures 5 and 6 one sees waveforms for various aspect angles for slit widths of 1 and .5 respectively. In case of $\Theta < \pi/2$ one finds that the dominant effect of varying slit width is to reduce the amplitude of the maximum with its shape being only slightly effected. At larger aspect angles, however, the slit width becomes important in determining the shape of the region of maximum. Comparing the waveforms at $\Theta = 120^\circ$ in both figures, one notes that while the amplitude is somewhat less for $\zeta = .5$, the position of maximum is substantially more well defined than in the $\zeta = 1.0$ case.

From Figures 4, 5, and 6 one concludes that the amplitude and detectability of the maximum point are optimized by selecting a slit width corresponding to the scale of the object.

Figure 7 displays a plot of x_0/b (at the location of the maximum) versus aspect angle for $\zeta = 1.0$ and .5. From this plot one sees that as the slit width is decreased the difference between the position of maximum response and the physical center of the disk decreases for gibbous phases while it increases for crescent phases. From the figure one notes that "crescent phase" as used here does not strictly imply all $\Theta > \pi/2$. When placed in juxtaposition to the previous conclusion regarding slit width, this result indicates the existence of tradeoff between maximum point spatial resolution and the deviation of that point from the centroid of the disk.

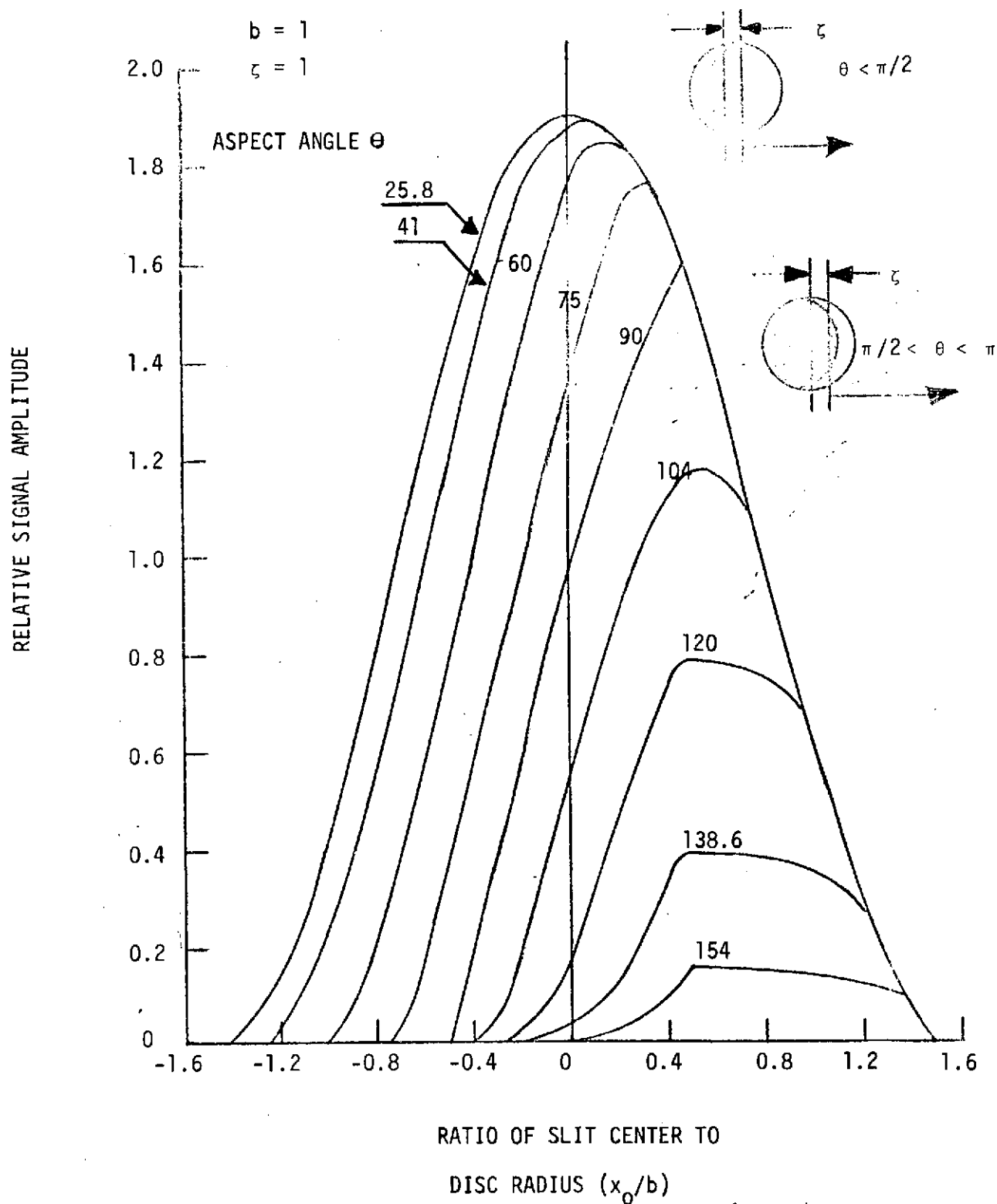
PREDICTED SIGNAL WAVEFORM

FIGURE 4



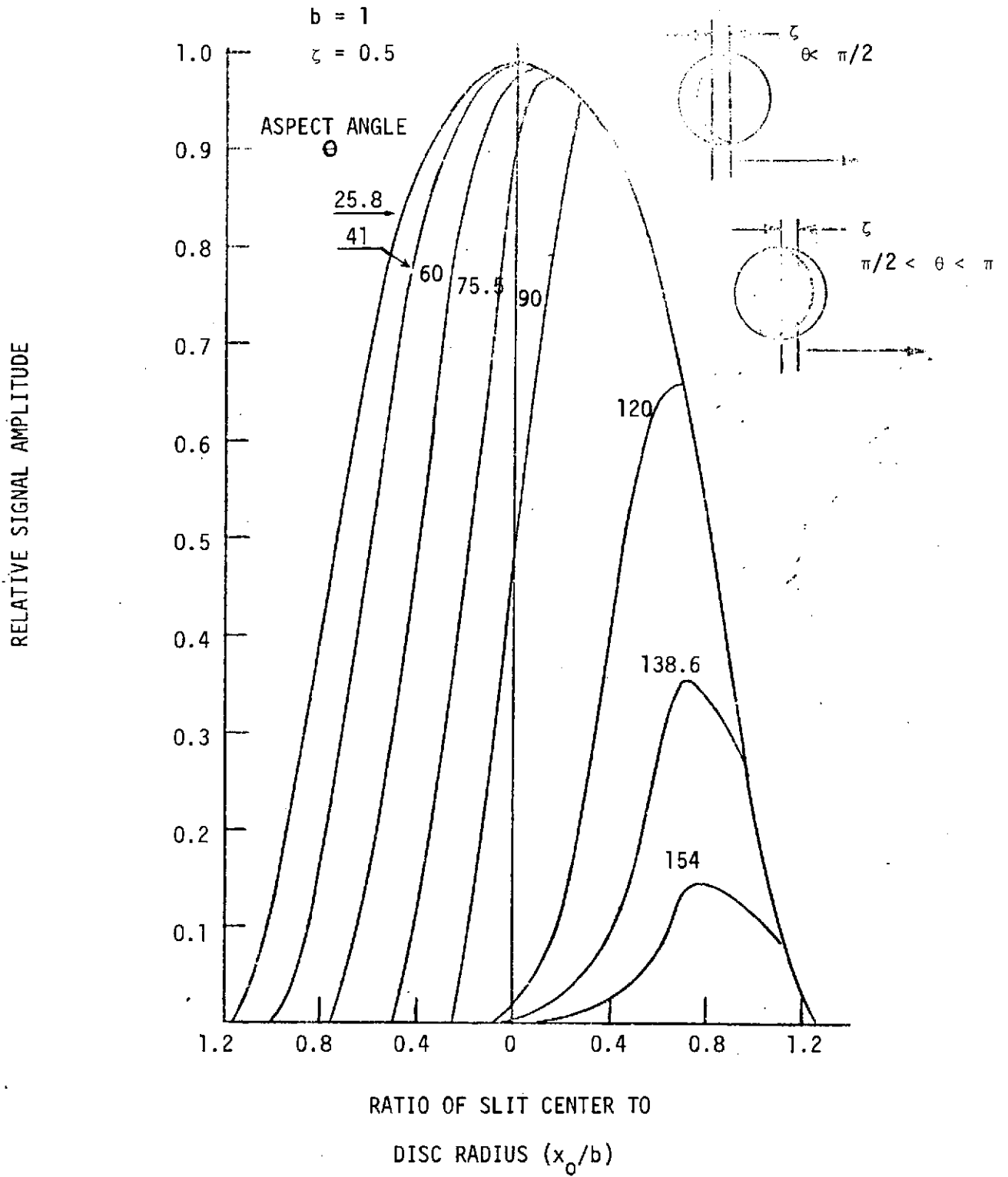
PREDICTED SIGNAL WAVEFORM

FIGURE 5



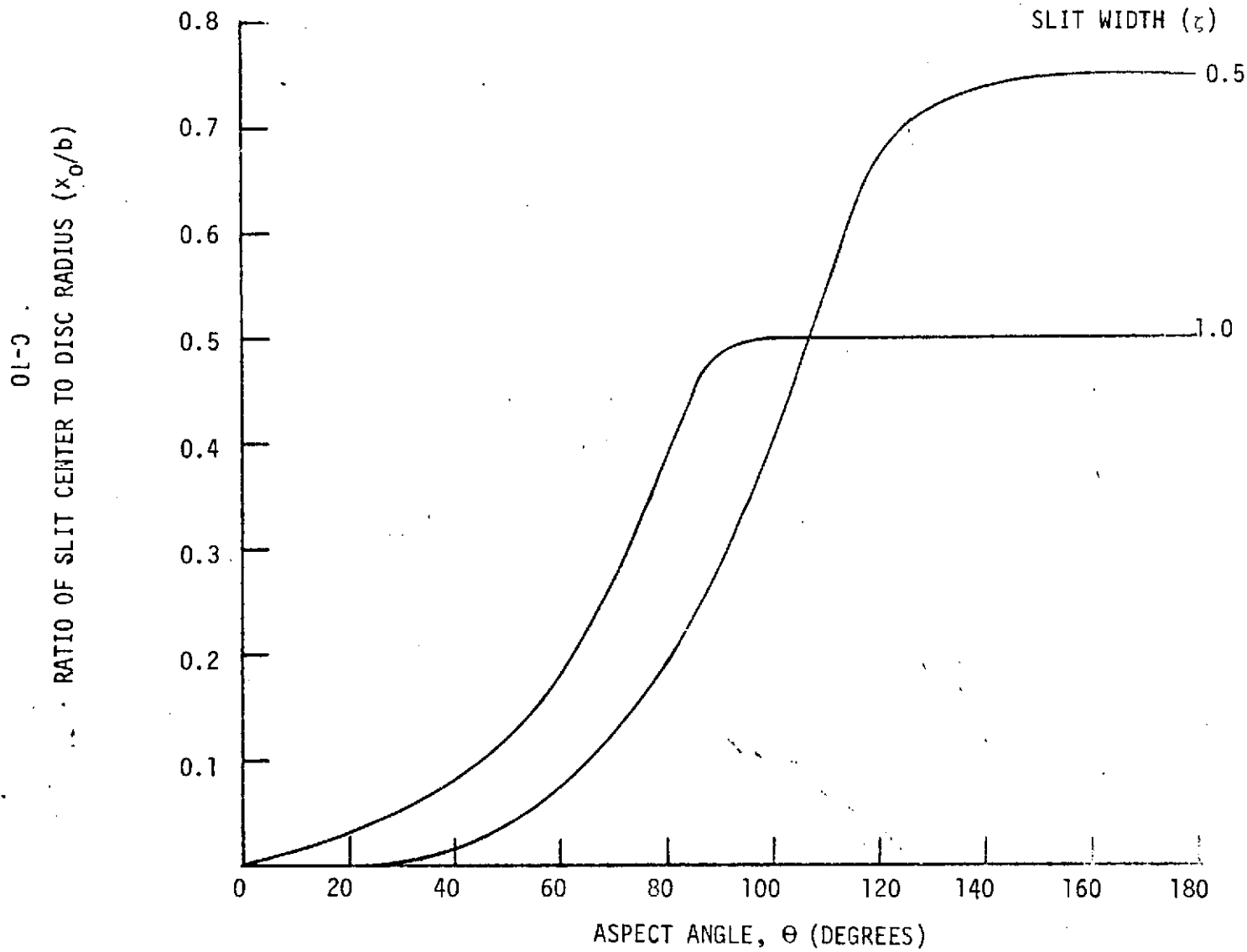
PREDICTED SIGNAL WAVEFORM

FIGURE 6



VARIATION OF SIGNAL RESPONSE WITH
SLIT WIDTH AND ASPECT ANGLE

FIGURE 7



APPENDIX D

THE EFFECT OF THE GENERAL STELLAR AND NON-STELLAR BACKGROUND ON SIGNAL-TO-NOISE AND THE TRUE AND FALSE DETECTION PROBABILITIES OF THE V-SLIT SCANNER

All important background sources, with the exception of scattered planetary light, have been examined and are found to take a maximum brightness of $m_V = 5.56$, or .24 of the luminosity of the minimum required detection at $m_V = 4.0$. It is shown that such a background has only a minimal effect, serving to reduce the signal to noise ratio to 16.25 from the value of 18 expected in the absence of a background. The probability of a true detection (P_T) and a false detection (P_F) have been considered and an expression for the threshold value required to maximize P_T derived. For the optimum threshold value the maximum expected background results in $P_T = 1.0$ and $P_F = 0.0$ to an accuracy of at least 1 in 10^{14} , and thus false detections due to background occur at a rate of approximately $5 \times 10^{-10} \text{ sec}^{-1}$.

The validity of the assumption that scattered planetary light may be neglected is presently uncertain, and particularly so in the case of Saturn where it has recently been suggested that a distribution of ring particles may exist beyond the presently defined edge of the A ring. It can be argued, however, that such a source must certainly have a lower surface brightness than an average location in the galactic plane to have so far escaped detection.

BACKGROUND MODEL

Consider the background produced by the general star field of $m > 6$, non-star galactic light, and zodiacal light. The luminosity of these various sources is given in terms of numbers of tenth magnitude stars by Allen as follows:

TABLE 1

Source	Photographic	Visual
	(10^m Stars Deg ⁻²)	
Zodiacal Light	20	30
Non Star Galactic Light	20:	40:
Faint Stars (M76), $b^{II} = 90^0$	16	30
$\langle b^{II}, z^{II} \rangle$	48	95
$b^{II} = 0, \langle z^{II} \rangle$	140	320

Adding the Zodiacal and non-star components to the faint star luminosities and employing the V-slit field-of-view of $3^0 \times 20''$, the magnitude of the viewed sky is found to be as shown in Table 2.

TABLE 2

	m_{pg}	m_v
$b^{II} = 90^0$	7.60	7.00
$\langle b^{II}, z^{II} \rangle$	7.10	6.45
$b^{II} = 0, \langle z^{II} \rangle$	6.35	5.56

If the threshold is set at 4^m , the factors relating the background flux to the threshold flux are as given in Table 3

TABLE 3

	L_{pg}	L_v
$b^{II} = 90^0$.035	.063
$\langle b^{II}, z^{II} \rangle$.057	.105
$b^{II} = 0, \langle z^{II} \rangle$.114	.236

The signal to noise for the V-slit system at the PMT cathode, assuming a quantum efficiency of .2, is given by (Reference 1) as follows:

$$S/n = 4.35 \times 10^{-2} \frac{n'}{(N_B + n')^{1/2}} \quad \begin{array}{l} n' = \text{target signal} \\ N_B = \text{background signal} \end{array} \quad (1)$$

The photon flux due to a 4^m target is:

$$n_0 = 1.75 \times 10^5 \text{ photons cm}^{-2} \text{ sec}^{-1} \quad (2)$$

Thus employing the worst case in Table 3, i.e. $b^{II} = 0, \langle z^{II} \rangle, L_v$,

the background signal is

$$N_0 = .236 n = 4.15 \times 10^4 \text{ photons cm}^{-2} \text{ sec}^{-1}. \quad (3)$$

Employing (2) and (3) in (1) yields

$$S/N = 16.25 \quad (4)$$

This is to be compared with a $S/N = 18$ derived (Ref. 1) in the absence of a background. Thus it is seen that the maximum expected background, excluding the body of the planet, has only a marginal effect on S/N and that the S/N continues to take a pleasingly large value.

3. TRUE DETECTION AND FALSE ALARM PROBABILITIES

The probability of a true detection and of a false alarm are given by

$$P_T = \frac{1}{2} \left(\operatorname{erf} \left(\frac{S/N - T/N}{\sqrt{2}} \right) + \operatorname{erf} \left(\frac{T/N_B - S_B/N_B}{\sqrt{2}} \right) \right) \quad (5)$$

$$P_F = \frac{1}{2} \left(1 - \operatorname{erf} \left(\frac{T/N_B - S_B/N_B}{\sqrt{2}} \right) \right) \quad (6)$$

where $S_B \equiv$ Background Signal

$S = S_B + S_T =$ Total signal with target

$N_B = \sqrt{S_B} =$ Background noise

$N = \sqrt{N_B^2 + N_T^2} =$ Total background noise

and assuming $S_B < T' < S$

letting $S_T = nS_B$ and thus $N^2 = N_B^2 (1 + n)$, P_T and P_F may be written

(7)

as

$$P_T = \frac{1}{2} \left(\operatorname{erf} \frac{1}{\sqrt{2}} \left(S_B^{1/2} (1+n)^{1/2} - \frac{T'}{S_B^{1/2} (1+n)^{1/2}} \right) + \operatorname{erf} \frac{1}{\sqrt{2}} \left(\frac{T'}{S_B^{1/2}} - S_B^{1/2} \right) \right)$$

$$P_F = \frac{1}{2} \left(1 - \operatorname{erf} \frac{1}{\sqrt{2}} \left(\frac{T'}{S_B^{1/2}} - S_B^{1/2} \right) \right) \quad (8)$$

The optimum value of T' may be determined by demanding that $\partial P_T / \partial T = 0$ which results in

$$\frac{1}{b} \exp\left(-\frac{1}{\sqrt{2}} \left(\frac{T'}{b} - b\right)^2\right) = \frac{1}{a} \exp\left(-\frac{1}{\sqrt{2}} \left(a - \frac{T'}{a}\right)^2\right) \quad (9)$$

where

$$a = S_B^{1/2} (1 + n)^{1/2}$$

$$b = S_B^{1/2}$$

or

$$T' = ab \left(1 - \frac{\sqrt{2}}{(b^2 - a^2)} \ln \frac{a}{b}\right)^{1/2} \quad (10)$$

or substituting for a and b

$$T = S_B (1 + n)^{1/2} \left(1 + \frac{\ln (1 + n)}{\sqrt{2} S_B n}\right)^{1/2} \quad (11)$$

Using Equation (1) to replace T in (5) produces

$$P_T = 1/2 \left[\operatorname{erf} \frac{1}{\sqrt{2}} \left(S_B^{1/2} \left((1 + n)^{1/2} - \left(1 + \frac{\ln (1 + n)}{\sqrt{2} S_B n}\right)^{1/2} \right) \right. \right. \\ \left. \left. + \operatorname{erf} \frac{1}{\sqrt{2}} \left(S_B^{1/2} \left((1 + n)^{1/2} \left(1 + \frac{\ln (1 + n)}{\sqrt{2} S_B n}\right)^{1/2} - 1 \right) \right) \right] \quad (12)$$

The target signal at the cathode at 4^m is found to be

$$S_T = 328 \text{ photons}$$

Employing Table 3 the worst case background takes a value of

$$S_B = .236 (328) = 77 \text{ photons.}$$

Noting that $n = \frac{1}{L} = \frac{1}{.236} = 4.25$, Equation 12 may be written

in the worst case as

$$P_T = \left[\frac{1}{2} \operatorname{erf} \frac{1}{\sqrt{2}} \left(8.8 \left(2.29 - \left(1 + \frac{1.79}{464} \right)^{1/2} \right) \right) + \operatorname{erf} \frac{1}{\sqrt{2}} \left(8.8 \left(2.29 \left(1 + \frac{1.79}{464} \right)^{1/2} - 1 \right) \right) \right] \quad (13)$$

$$= \frac{1}{2} \left(\operatorname{erf} (14.3) + \operatorname{erf} (8) \right) \quad (14)$$

therefore

$$P_T = 1.0 \text{ (to at least } 1 \text{ in } 10^{14} \text{ (Jolly 1973))} \quad (15)$$

One also has

$$P_F = \frac{1}{2} (1 - \operatorname{erf} (8)) = 0 \text{ (to 14 places)}$$

Thus for the worst case background one expects any detection to be a true detection to a certainty of at least $1 \text{ in } 10^{14}$, and false detections to pose no problem for the V-slit scanner operating as defined.

APPENDIX E

THE ENERGY, PHOTON FLUX, AND APPARENT MAGNITUDE OF A SOLAR SYSTEM OBJECT VIEWED FROM AN ARBITRARY LOCATION.

General expressions are derived for the energy and photon flux received from a spherical, solar illuminated body viewed at an arbitrary range and aspect angle. These relations are further used to obtain a relation for the apparent magnitude of the object and to form an expression for the signal-to-noise ratio expected if the noise is purely photon statistical. The signal-to-noise ratio is evaluated in the case of an $m_V = 4$ object.

DERIVATION OF THE FLUX EQUATIONS

Consider the case of zero aspect angle. The monochromatic solar flux at the object is given by

$$H_{s,\nu} = \pi I_{\odot,\nu} \frac{R_{\odot}^2}{r^2} \quad (1)$$

where

$r \equiv$ sun-object distance

$R_{\odot} \equiv$ solar radius

$I_{\odot,\nu} \equiv$ solar radiance

and thus the amount of energy intercepted by the object may be written as:

$$E_{s,\nu} = \pi^2 R_s^2 I_{\odot,\nu} \frac{R_{\odot}^2}{r^2} \quad (2)$$

where

R_s = object radius

Letting A_ν be the object's bond albedo, ignoring limb darkening, and equating the intercepted and reflected energies one may write the flux seen by an observer as:

$$H_{o,\nu} = \frac{\pi A_\nu I_{\odot\nu}}{2} \left(\frac{R_\odot R_s}{r r_o} \right)^2 \quad (3)$$

where

r_o ≡ object-observer distance

Setting $I_\odot = B_\nu$, i. e., ignoring spectral features, and allowing some non-zero aspect angle Θ the received energy and photon fluxes over a frequency band $\nu_1 \leq \nu \leq \nu_2$ may be expressed as

$$H_{o,i} = \frac{\pi h}{2c^2} (1 + \cos\Theta) \left(\frac{R_\odot R_s}{r r_o} \right)^2 \int_{\nu_1}^{\nu_2} \frac{A_\nu \nu^3}{\left(e^{\frac{h\nu}{kT}} - 1 \right)} d\nu \quad (4)$$

$$N_{o,i} = \frac{\pi}{2c^2} (1 + \cos\Theta) \left(\frac{R_\odot R_s}{r r_o} \right)^2 \int_{\nu_1}^{\nu_2} \frac{A_\nu \nu^2}{\left(e^{\frac{h\nu}{kT}} - 1 \right)} d\nu \quad (5)$$

where i indicates the color corresponding to $\nu_1 \leq \nu \leq \nu_2$

3. APPARENT MAGNITUDE

The apparent magnitude of the object at an arbitrary location is given by

$$m_{o,i} = -2.5 \text{ Log } H_{o,i} + C_1 \quad (6)$$

or employing equation (4).

$$m_{\odot, i} = -2.5 (-.3 + \text{Log } A_i + \text{Log } H_{\odot, i} + 2 \left(\text{Log } \frac{R_{\odot}}{r} + \text{Log } \frac{R_s}{r_{\odot}} \right) + \text{Log } \frac{1}{2} (1 + \cos\Theta)) + C_1 \quad (7)$$

where

$H_{\odot, i}$ = solar surface flux

Similarly, the magnitude of the object at the earth is:

$$m_{\oplus, i} = -2.5 (-.3 + \text{Log } A_i + \text{Log } H_{\odot, i} + 2 \left(\text{Log } \frac{R_{\odot}}{r} + \text{Log } \frac{R_s}{r_{\oplus}} \right) + \text{Log } \frac{1}{2} (1 + \cos\Theta)) + C_1 \quad (8)$$

Assuming $m_{\oplus, i}$ is evaluated at opposition, Equations (7) and (8) may be combined to yield:

$$m_{\odot, i} = 2.5 \left(2 \text{Log } \frac{r_{\oplus}}{r_{\odot}} - \text{Log } \frac{1}{2} (1 + \cos\Theta) \right) + m_{\oplus, i} \quad (9)$$

4. PHOTON STATISTICAL SIGNAL-TO-NOISE RATIO

Letting the detector quantum efficiency be η , the optical filter transmission be F_{ν} , the optical element transmission be $k_{i, \nu}$ for the i th element, and the receiving optics diameters be D , and recalling that $N = \sqrt{S}$ for photon noise, the signal-to-noise ratio may be written as:

$$S/N = \frac{\pi D}{2c} \left(\frac{R_{\odot} R_s}{r r_{\odot}} \right) \left(\frac{1 + \cos\Theta}{2} \right)^{1/2} \left\{ \int_{\nu_1}^{\nu_2} \frac{\eta A_{\nu} F_{\nu} \prod k_{i, \nu} \nu^2}{\left(e^{\frac{h\nu}{kT}} - 1 \right)} d\nu \right\}^{1/2} \quad (10)$$

where $t \equiv$ integration time.

5. EVALUATION OF THE SIGNAL-TO-NOISE RATIO FOR AN OBJECT OF $m_v = 4$

The flux from a $m_v = 4$ star may be calculated from the solar constant and the apparent magnitude of the sun to be

$$H_{m_v = 4} = 6.9 \times 10^{-14} \text{ watt-cm}^{-2} \quad (11)$$

Using the average solar photon energy, Equation (1) may be transformed to a photon flux, viz.

$$N_{m_v = 4} = \frac{H_{m_v = 4}}{\langle h \nu \rangle} = 1.75 \times 10^5 \text{ cm}^{-2} \text{ sr}^{-1} \quad (12)$$

Letting $D = 8.9$ cm, $k = .9$, $n = 2$, $\eta = .2$, and $\Theta = 0$, which are representative of Pioneer outer planets missions, the signal-to-noise ratio may be written as

$$S/N = \frac{8.9}{2} \pi^{1/2} t^{1/2} (.2)^{1/2} (.9) (1.75 \times 10^5)^{1/2} \quad (13)$$

or

$$S/N = 1.33 \times 10^3 t^{1/2} \quad (14)$$

For a satellite spin rate of 5 rpm the dwell time of an object on a 20" slit is:

$$t = 1.8 \times 10^{-4} \text{ sec} \quad (15)$$

Therefore, the signal-to-noise ratio becomes

$$S/N = 17.8 \quad (16)$$

The flux emitted by the object is given by

$$H_s = -2\pi \int_1^0 I_{s,\nu} \mu d\mu = \pi I_{s,\nu} \quad (1.1)$$

$\mu = \cos\theta$, $\theta =$ angle from the normal to the direction of radiation,

$I_{s,\nu}$ is assumed to be isotropic.

Using Equation (1.1) the energy emitted by the object is

$$E_{s,\nu \text{ out}} = 2\pi^2 R_s^2 I_{s,\nu} \quad (1.2)$$

Equating (1.2) and (2) with the effect of albedo included, one may write.

$$I_{s,\nu} = \frac{A\nu}{2} I_{\odot,\nu} \frac{R_{\odot}^2}{r^2} \quad (1.3)$$

whereupon the flux received by an observer at some distance, r_o may be expressed as

$$H_{o,\nu} = -2H \int_1^{\sqrt{1 - (R_s/r_o)^2}} I_{s,\nu} \mu d\mu \quad (1.4)$$

$$H_{o,\nu} = \frac{\pi A\nu}{2} I_{\odot,\nu} \left(\frac{R_o R_s}{r r_o} \right)^2 \quad (1.5)$$

APPENDIX F

MINIMUM ALLOWABLE SLIT WIDTH FOR THE V-SLIT SCANNER

The minimum allowable slit width is determined by the requirement that at some range ^{*} one wishes the target, as convolved with the slit, to have an apparent luminosity of 4th magnitude. The required widths have been evaluated for the brightest satellites of Saturn and Uranus. Assuming the initial detection occurs at the greatest possible distance, it is found that a slit width on the order of 7 arc-seconds will suffice in all cases. Using the focal length of the test system the required physical size of the slit takes a value of 4×10^{-4} inches.

THE SLIT-DISK GEOMETRY

Figure F-1 displays the slit-disk geometry yielding the maximum observed luminosity for a given slit width and disk diameter.

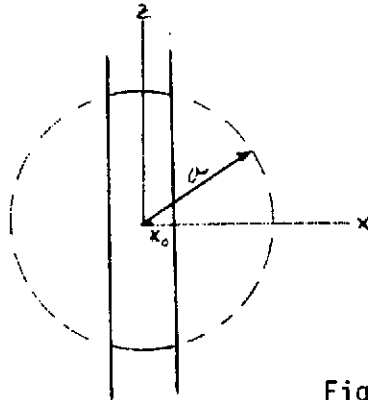


Fig. F-1. Slit Disk Geometry

*Obviously only ranges less than that at which the satellite alone appears at 4^m are allowed.

The area viewed is given by

$$I = 4 \int_0^{x_0} (a^2 - x^2)^{1/2} dx = 2 \left[x_0 (a^2 - x_0^2)^{1/2} + a^2 \sin^{-1} \frac{x_0}{a} \right] \quad (1)$$

or in units of the total disk area as

$$I = \frac{2}{\pi} \left[y (1 - y^2)^{1/2} + \sin^{-1} y \right], \text{ where } y \equiv \frac{x_0}{a} \quad (2)$$

The apparent magnitude of the target at a range R_{ϕ_0} has been given in Appendix E, as

$$m_{\phi_0} = 2.5 \left(2 \log \frac{R_{\phi_0}}{R_{\phi_0}} \right) + m_{\phi_0} \quad (3)$$

where the aspect angle, θ , has been assumed to be zero.

Upon inclusion of the factor given in Equation (2), (3) becomes

$$m_{\phi_0} = 2.5 \left(2 \log \frac{R_{\phi_0}}{R_{\phi_0}} - \log \left(\frac{2}{\pi} \right) \left[y(1 - y^2)^{1/2} + \sin^{-1} y \right] \right) + m_{\phi_0} \quad (4)$$

Setting m_{ϕ_0} to the limiting value of 4^m and rearranging yields

$$y(1 - y^2)^{1/2} + \sin^{-1} y = \exp \left(.925 m_{\phi_0} + 4.64 \log_t \frac{R_{\phi_0}}{R_{\phi_0}} - 3.25 \right) \quad (5)$$

For fixed m_{\oplus} and R_{\oplus} , y has been found by scaled first order numerical iteration to an accuracy of at least 10^{-5} .

RESULTS OF THE MINIMUM SLIT WIDTH CALCULATION

Figures F-2 and F-3 present the minimum required slit width in arc-sec. versus target range for the brightest satellites of Saturn and Uranus, respectively. The termination points of the curves are the range at which the target alone appears as 4^m , and the angular size of the target at that distance. Assuming one wishes to detect satellites at the earliest possible moment the termination points define the minimum allowable slit width. Among these points Titania takes the largest value, i. e. 6.7" and thus if the slit were constructed to a nominal value of 7" all the satellites of interest would be accommodated. If one wishes to relax the requirement of earliest possible detection the slit may be made smaller as indicated by the figures. It should be noted however that for the slit to be less than 1" and yet be useable for all satellites, the limiting range would be constrained by Umbriel and would be $\leq 5 \times 10^6$ km.

Using the focal length of the nominal test setup the data of Figures 2 & 3 may be converted to the required physical size of the slit. These data may be found in Figures F-4 and F-5. From these one sees that the minimum slit width for earliest possible detection is approximately 4×10^{-4} inches ($\sim 10\mu$).

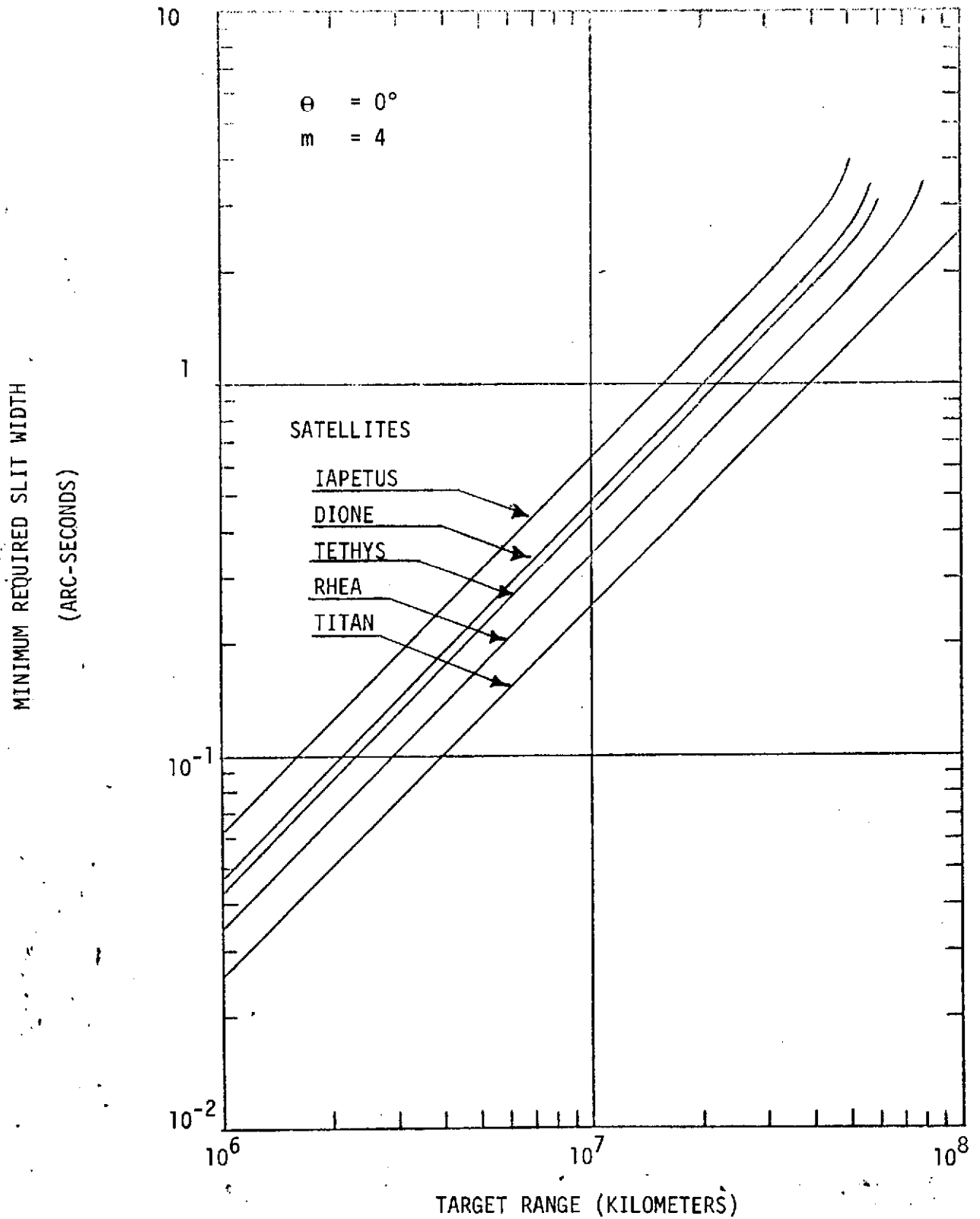
REMARKS RELEVANT TO THE MINIMUM SLIT WIDTH

DIFFRACTION

Assuming that the system operates at an effective wavelength of $.5\mu$ the suggested slit of 10μ width results in the first diffraction minimum occurring at 2° , which in turn couples with the nominal one inch focal length of the field lens to produce an acceptable .1 inch wide primary maximum at the photocathode. One should note however that the use of a slit small enough to give 1" resolution results in a primary maximum .7 inch wide which is clearly unacceptable.

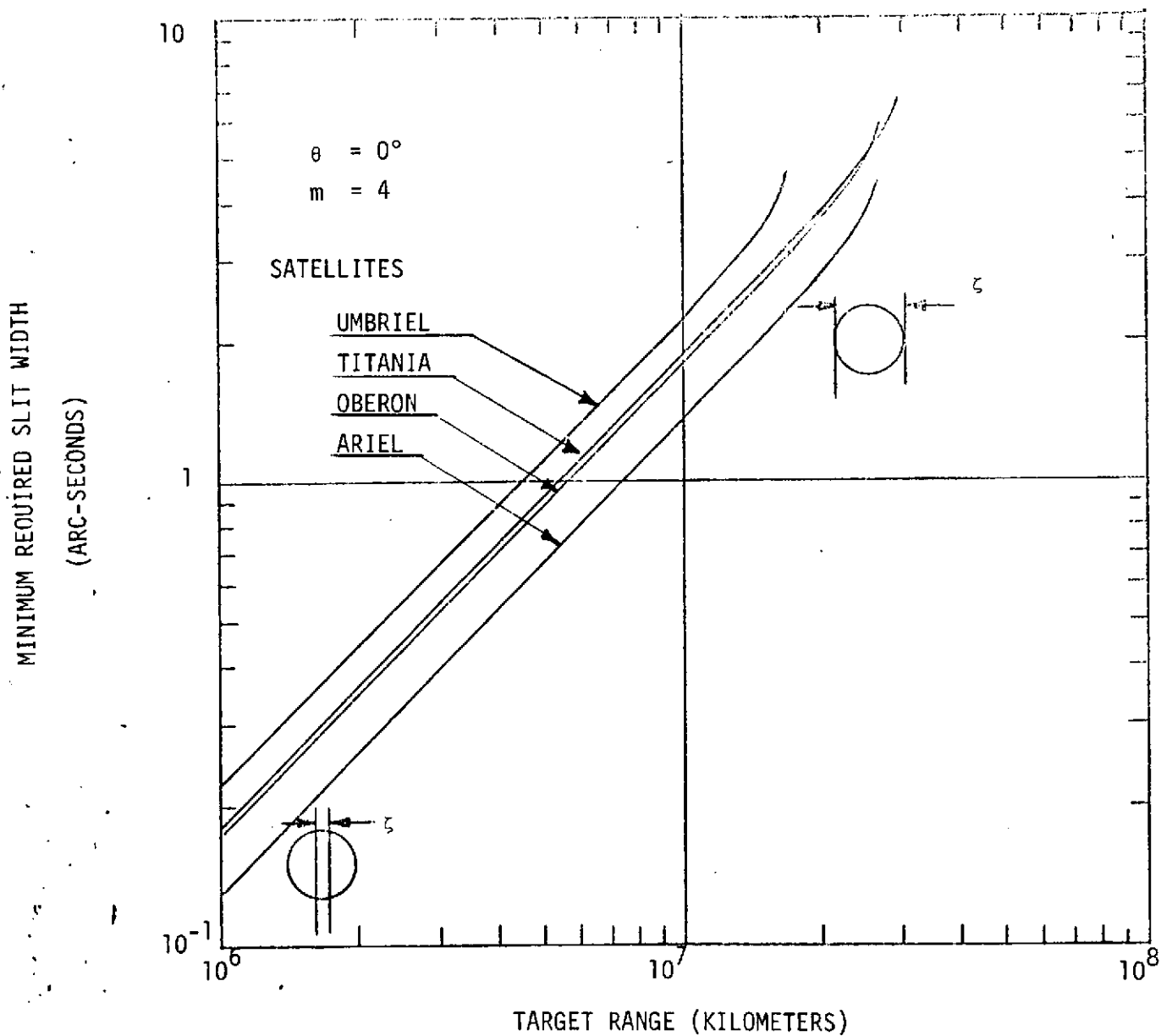
SLIT WIDTH DEPENDENCE ON TARGET
RANGE FOR SATURN'S SATELLITES

FIGURE F - 2



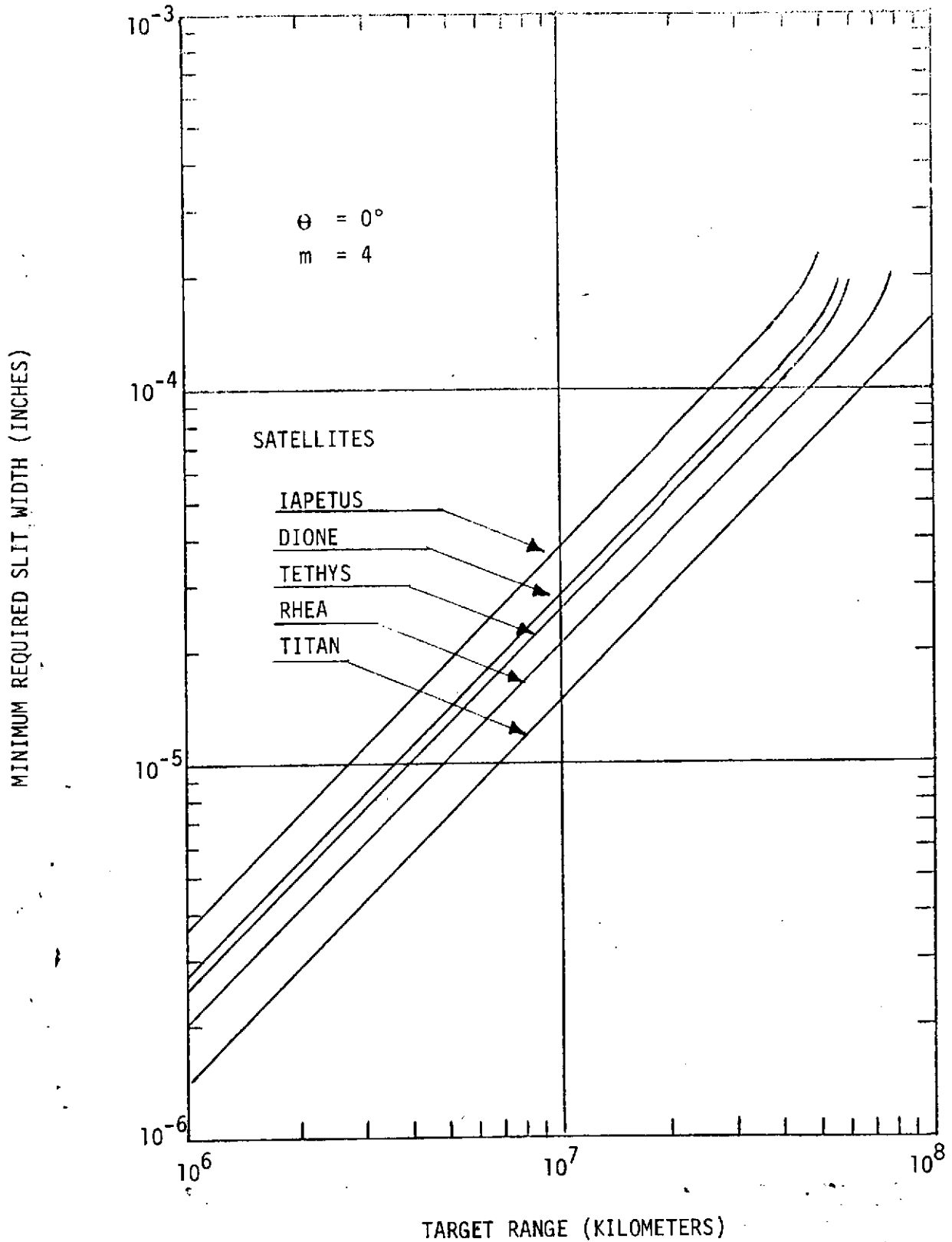
SLIT WIDTH DEPENDENCE ON TARGET
 RANGE FOR URANUS' SATELLITES

FIGURE F - 3



SLIT WIDTH DEPENDENCE ON TARGET
RANGE FOR SATURN'S SATELLITES

FIGURE F - 4

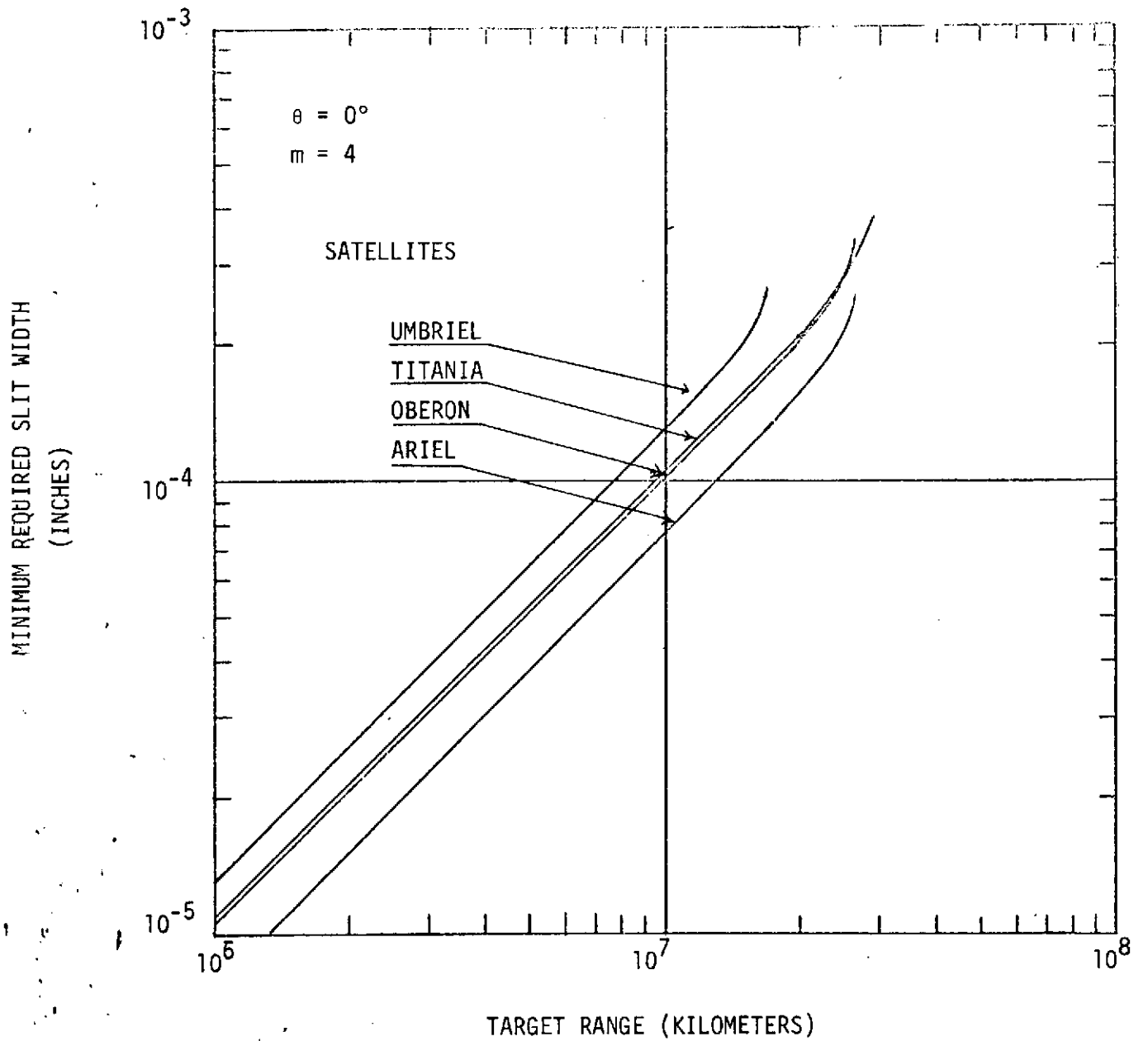


C-2

SLIT WIDTH DEPENDENCE ON TARGET

RANGE FOR URANUS' SATELLITES

FIGURE F - 5



PHYSICAL LIMITATIONS

The problem of etching the slit to the required size and tolerances becomes non-trivial as one progresses to smaller sizes, and indeed this, rather than other considerations, may dictate the smallest possible width.

APPENDIX G

DETECTION STATISTICS IN FLIGHT

The mean star background is approximately equivalent to a $+23^m$ star/arc sec². The average scatter due to sunlight is taken as an additional $+23^m$ star/arc sec². Since the total field of view for the two slits is $2 \times 17 \times 3 \times 3600 = 373,200$ arc sec², the background light is equivalent to that observed from 746,400 stars of visual magnitude $+23$.

From Section 4, the anode signal current (I_S) for a fourth magnitude star was 143×10^{-9} amps.

The current resulting from the star background would be

$$I_B = 746,400 \times \frac{(2.51)^{-23}}{(2.51)^{-4}} \times 143 \times 10^{-9}$$
$$= 2.7 \times 10^{-9} \text{ amps}$$

The dark current I_D observed at the anode of the photo-multiplier is typically 1.4×10^{-9} amps for a multiplier gain of 2×10^6 .

When the star signal is present the average peak anode current \bar{I}_T is

$$\bar{I}_T = I_B + I_D + I_S = 147.1 \times 10^{-9} \text{ amps}$$

The rms variation $\langle I_T \rangle$ in the peak current is

$$\begin{aligned}
\langle I_T \rangle &= 2 \times 10^6 \sqrt{2e \bar{I}_T \Delta f / 2 \times 10^6} \\
&= \sqrt{2 \times 1.6 \times 10^{-19} \times 147.1 \times 10^{-9} \times 2 \times 10^3 \times 2 \times 10^6} \\
&= 13.8 \times 10^{-9} \text{ amps}
\end{aligned}$$

The resulting signal to noise ratio is thus

$$S/N = 10.6:1$$

By using a thresholding level that is 50% of the expected peak signal, the threshold is 5.3σ below the average peak. Assuming Gaussian statistics the probability of the peak signal + noise being below the threshold level is less than 1×10^{-6} . Thus, the probability of detection is in excess of .999999.

The probability of false alarm may be calculated by looking at signal levels when the star is not present.

$$\bar{I}_{T'} = I_D + I_B = 4.1 \times 10^{-9} \text{ amps}$$

$$\begin{aligned}
\langle I_{T'} \rangle &= \sqrt{2 \times 1.6 \times 10^{-19} \times 4.1 \times 10^{-9} \times 2 \times 10^3 \times 2 \times 10^6} \\
&= 2.3 \times 10^{-9} \text{ amps}
\end{aligned}$$

Since the threshold level is set at 73.5×10^{-9} amps, it is about 32σ above the noise. Using either Gaussian or Poisson statistics, the calculated false alarm probability would be essentially zero. Poisson statistics are more relevant for this case where the expected photoelectron numbers are so low.

APPENDIX H

PHOTO MULTIPLIER DATA

EMR PHOTOELECTRIC

Customer TRW
 POA No. 2587
 Serial No. 18146

Model No. 541E-01-14-03900

This serves to certify that the Photoelectric device described above has been inspected and tested in accordance with the specification dated 872 (attached)

Photocathode Characteristics:

Wavelength — nm	Radiant Sensitivity x 10 ⁻³ A/W	Quantum Efficiency %
<u>420</u>	<u>73.0</u>	<u>21.6</u>
<u>630</u>	<u>31.7</u>	<u>6.2</u>
<u>800</u>	<u>6.4</u>	<u>.99</u>

See the attached curve for complete spectral characteristic.

Luminous sensitivity 203.3 μ A/Lumen

Multiplier Phototube Characteristics:

¹ Amplification <u>10⁵</u> at <u>1345</u> V	² Dark Current <u>2.3 x 10⁻¹⁰</u> A
Amplification <u>10⁶</u> at <u>1715</u> V	Dark Current <u>2.6 x 10⁻⁹</u> A
Amplification <u>10⁷</u> at <u>2225</u> V	Dark Current <u>2.8 x 10⁻⁸</u> A
Amplification <u>10⁸</u> at <u>2985</u> V	Dark Current <u>3.0 x 10⁻⁷</u> A

See attached curve for amplification over normal operating range.

Maximum Ratings:

Supply Voltage 3600 V
 Anode Current (Avg.) 6.0 x 10⁻⁶ A
 Temperature 85 °C


Remarks:

Notes:

NA: Not Applicable

- See schematic diagram for voltage distribution.
- Measured at 20 ° Centigrade, after dark stabilization for 16 hours

Date: 7-20-73

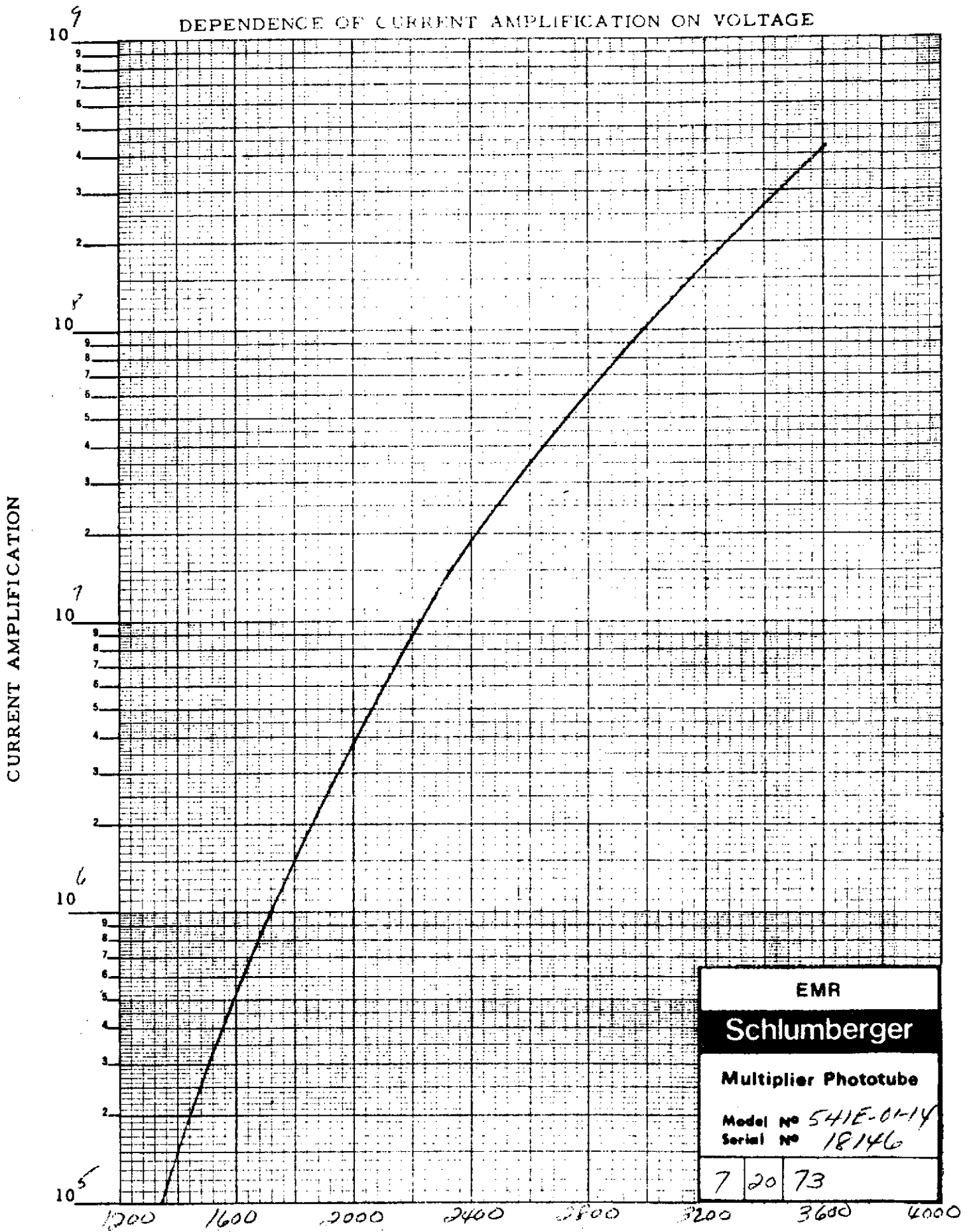
7-20-73 
 Quality Assurance Approval

G.W.
 Test Supervisor



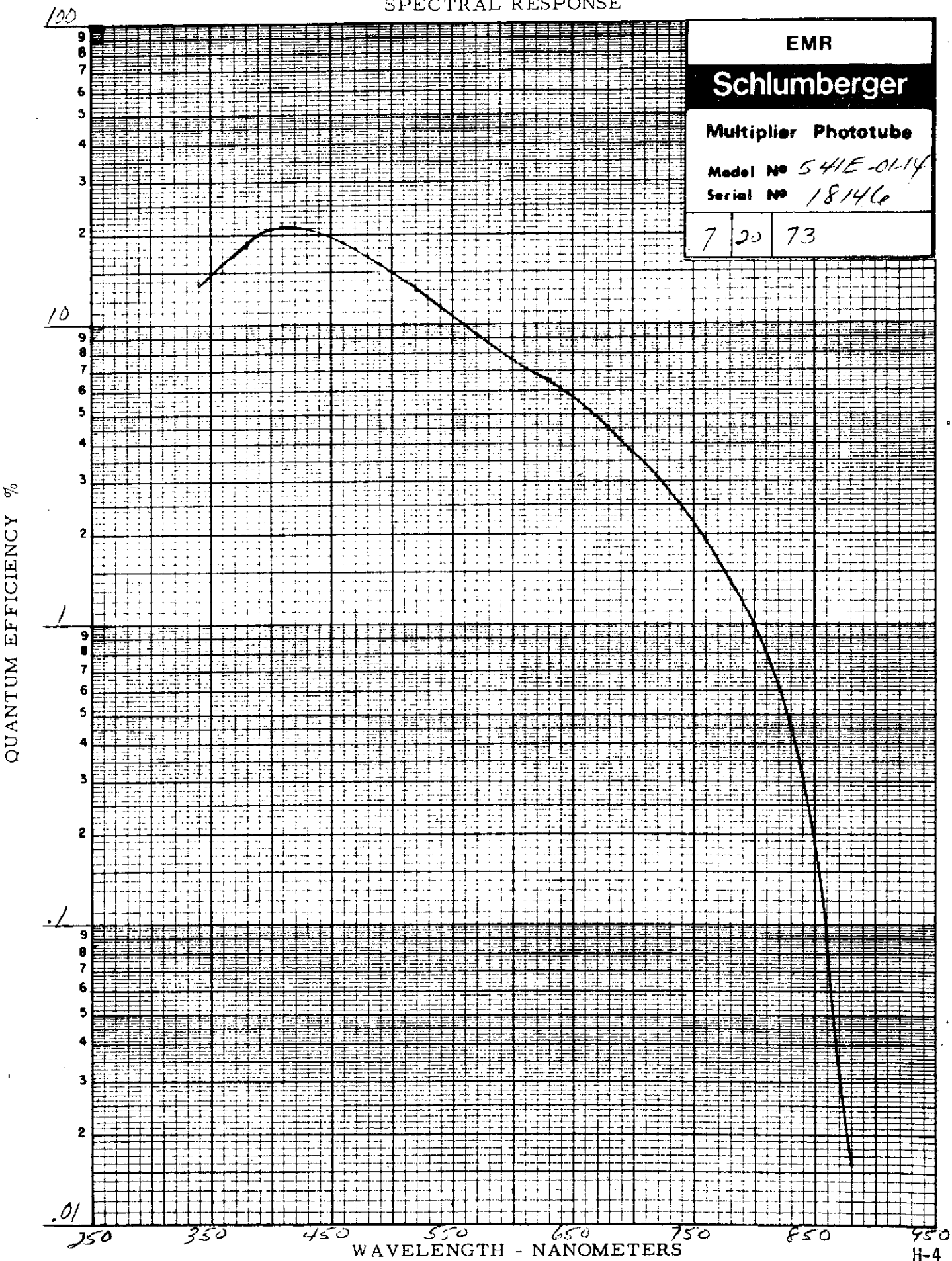
EMR PHOTOELECTRIC
 BOX 44, PRINCETON, NEW JERSEY 08540
 TELEX 843-459 • TELEPHONE 609-799-1000

DEPENDENCE OF CURRENT AMPLIFICATION ON VOLTAGE



EMR		
Schlumberger		
Multiplier Phototube		
Model No 541E-01-14		
Serial No 18146		
7	20	73

SPECTRAL RESPONSE



EMR

Schlumberger

Multiplier Phototube

Model No 541E-0114

Serial No 18146

7 20 73

QUANTUM EFFICIENCY %

WAVELENGTH - NANOMETERS

APPENDIX J

COMPUTER PROGRAMS

PROGRAM ZORCH

THIS PROGRAM COMPUTES THE FOLLOWING:

PROBABILITY OF DETECTION
 PROBABILITY OF TRUE DETECTION
 PROBABILITY OF FALSE ALARM
 TARGET SIGNAL LEVEL
 NOISE LEVEL
 THRESHOLD LEVEL
 NUMBER OF FALSE ALARMS PER SATELLITE REVOLUTION

GET, ZORCH = ZORCH
 [LIST, ZORCH

```

00100      PROGRAM ZORCH (INPUT,OUTPUT)
00110      10 ACCEPT D,XM,Q,DNU,XL,R
00120      IF(D.EQ.9999.) GO TO 50
00130      PRINT 1,D,XM,Q,DNU,XL
00140      1 FORMAT(♦APERTURE=♦E11.3♦CM♦♦NUM. OF OPT. SURF.=♦E11.3♦♦11
00150      1♦DET. QUANT. EFF.=♦E11.3♦♦ELEC. BAND PASS=♦E11.3♦♦
00160      2♦BACKGRND IN UNITS OF 4MAG FLUX=♦E11.3)
00170      PI=3.14159
00180      ETA=1./XL
00190      T=1./((DNU♦SQRT(2.))
00200      SB=XL♦PI♦T♦Q♦((D♦♦2)/4.)♦(0.9♦♦XM)♦1.75E+05
00210      C=(ETA♦SQRT(SB)-R♦SQRT(1.+ETA))/SQRT(2.)
00220      PD=.5♦(1.+ERF(R/SQRT(2.)))
00230      PF=.5♦(1.-ERF(C))
00240      PT=PD-PF
00250      XNFREV=12.35♦DNU♦SQRT(2.)♦PF
00260      TH=SB♦(1.+ETA)-R♦SQRT(SB♦(1.+ETA))
00270      ST=SB/XL
00280      STDT=ST+SB
00290      TOTNOIS=SQRT(STDT)
00300      PRINT 2,PD,PT,PF,ST,TH,XNFREV,STDT,TOTNOIS
00310      2 FORMAT(♦PROB. OF DET.=♦E11.3♦♦PROB OF TRUE DET.=♦E11.3♦♦
00320      1♦PROB OF FALSE ALARM=♦E11.3♦♦♦TARGET SIGNAL=♦E11.3♦PHOTONS♦♦
00330      2♦THRESHOLD=♦E11.3♦PHOTONS♦♦♦NUM. OF FALSE ALARMS/REV.=♦E11.3
00340      3♦♦TOTAL SIGNAL=♦E11.3♦PHOTONS♦♦♦TOTAL NOISE=♦E11.3♦PHOTONS♦
+ )
00350      GO TO 10
00360      50 CONTINUE
00370      STOP
00380      END
    
```

[

PROGRAM WAV

THIS PROGRAM COMPUTES THE EXPECTED SIGNAL WAVEFORM AS A FUNCTION
OF SLIT WIDTH, ASPECT ANGLE, AND DISK RADIUS

[GET,WAV=WAV

[LIST ,WAV

PROGRAM WAVEFOR (INPUT,OUTPUT)

11 ACCEPT B,Z,TH

IF(B.EQ.9999.) GO TO 12

R=Z/B

X01=-(B+Z/2.)

DX=(B+Z/2.)/20.

PRINT 1

1 FORMAT(♦ DISK RADIUS SLIT WIDTH ASPECT ANGL SLIT/DISK♦/)

PRINT 2,B,Z,TH,R

2 FORMAT(1X,4(E11.3,2X)/)

PRINT 3

3 FORMAT(5X,♦ X0♦11X♦X0♦B♦8X♦AREA♦/)

DO 10 J=1,21

JJ=J-1

XJ=JJ

X0=X01+DX*XJ

XL=X0-Z/2.

XR=X0+Z/2.

IF(XL.LT.-B)50,51

50 IF(XR.LT.B)52,53

52 AL=-B

BET=XR

GO TO 60

53 AL=-B

BET=B

GO TO 60

51 IF(XR.LT.B)54,55

54 AL=XL

BET=XR

GO TO 60

55 AL=XL

BET=B

GO TO 60

60 AA=BET*SQRT(B**2-BET**2)

AB=AL*SQRT(B**2-AL**2)

AC=(B**2)*(ASIN(BET/B)-ASIN(AL/B))

A1=(AA-AB+AC)*(1.+COS(TH))*0.5

RX0=X0/B

PRINT 4, X0,RX0,A1

4 FORMAT(3(E11.3,2X))

10 CONTINUE

GO TO 11

12 CONTINUE

STOP

END

[

PROGRAM SIG

THIS PROGRAM COMPUTES THE LIMITING AND WORST CASE PERFORMANCE
OF THE V-SLIT MAPPER

NUMBER OF FALSE SIGNALS PER SECOND
NUMBER OF FALSE SIGNALS PER SATELLITE REVOLUTION
MAXIMUM CROSSING TIME BETWEEN SLITS
NUMBER OF BINARY STORAGE SPACES REQUIRED
MINIMUM RESOLUTION IN PHI-TILDA PLANE

GET, SIG = SIG
[LIST, SIG

J-4

```
00100      PROGRAM SIG (INPUT,OUTPUT)
00110      20 ACCEPT D,XM,0,DNU,XL,ALP,BET,FSI
00120      IF(D.EQ.9999.) GO TO 21
00130      AL=ALP/57.3
00140      BE=BET/57.3
00150      PI=3.14159
00160      ETA=1./XL
00170      T=1./(DNU*SQRT(2.))
00180      T1=1.802E-04/T
00190      ST=(PI*(D**2)/4.)*(0.9**XM)*T*0*1.75E+05
00200      SB=XL*ST
00210      G=(D/2.)*SQRT(PI*T*0)*(0.9**XM/2.)
00220      F=SQRT(1.75E+05)/SQRT(1.+XL)
00230      SN=G*F
00240      A=SQRT(1.+ETA)
00250      B=SQRT(1.+ALOG(1.+ETA)/(SB*ETA*SQRT(2.)))
00260      C=SQRT(SB/2.)*(A-B)
00270      E=SQRT(SB/2.)*(A*B-1.)
00280      PT=.5*(ERF(C)+ERF(E))
00290      PF=.5*(1.-ERF(E))
00300      XNFSEC=DNU*SQRT(2.)*PF
```

```

00310      XNFREV=XNFSEC*12.35
00320      TIMC=(5.24E-2*(TAN(AL)+TAN(BE))+PSI)/5.087E-1
00330      STOR2=(ALOG10(DNU*TIMC))/3.0103
00340      RES=(1.050E+5*T)/(.99863*(TAN(AL)+TAN(BE))+.0524*PSI)
00350      PRINT 10
00360      10 FORMAT(*SYSTEM PARAMETERS**/)
00370      PRINT 1,D,XM,Q,DNU,T,XL,ALP,BET,PSI
00380      1 FORMAT(*APERTURE=*F6.3* CM*/*NUM. OF OPT. SURF.*=*F2.0*/
00390      1*DET. QUAN. EFF.*=*E11.3*/*ELEC. BAND PASS=*E11.3* HZ*/
00400      2*INTEG. TIME=*E11.3* SEC*/*BCKGRND. IN UNITS OF 4MAG FLUX=*E
+ 11.3*/
00410      3*ALPHA=*F6.3* DEG*/*BETA=*F6.3* DEG*/*PSI=*E11.3**/)
00420      PRINT 2,ST,SB,SN,PT,PF,T1
00430      2 FORMAT(*SYSTEM INPUT AND RESPONSE**/*MIN TARGET SIG.*=*E11.3
00440      1* PHOTONS*/*BCKGRND. SIG.*=*E11.3* PHOTONS*/*SIGNAL-TO-NOISE=*
00450      2E11.3*/*PROB. OF A TRUE DETEC.*=*E11.3*/*PROB OF A FALSE DETE
+ C=*
00460      3E11.3*/*NUM. OF ZONES PER SLIT=*E11.3/**/) ,
00470      PRINT 3,XNFSEC,XNFREV,TIMC,STOR2,RES
00480      3 FORMAT(*LIMITING AND WORST CASE PERFORMANCE**/
00490      1*NUM. FALSE SIG./SEC=*E11.3*/*NUM FAL. SIG./SAT. REV.*=*E11.3
+ */
00500      2*MAX. CROSS. TIME BETWEEN SLITS=*E11.3* SEC*/
00510      3*NUM. BINARY STORAGE SPACES REQUIRED=*E11.3*/
00520      4*MIN. RES. IN PHI-TIL=*E11.3* ARC-SEC*)
00530      GO TO 20
00540      21 CONTINUE
00550      STOP
00560      END

```

Program for Computing α_V and β_V

```
-----
00200      SUBROUTINE COMPUT(WT1,XD1,YD1,A1,B1)
00202      PI=3.14159
00204      BZ=PI/4.5
00210      PD1=SQRT(XD1**2+YD1**2+144.)
00230      ZX=XD1*COS(WT1)*COS(BZ)-YD1*SIN(WT1)
00240      ZX=ZX+12.*SIN(BZ)*COS(WT1)
00250      ZY=XD1*SIN(WT1)*COS(BZ)+YD1*COS(WT1)
00260      ZY=ZY+12.*SIN(WT1)*SIN(BZ)
00270      A1=ATAN(ZY/ZX)
00280      B1=ACOS((-XD1*SIN(BZ)+12.*COS(BZ))/PD1)
00282      RETURN
00284      END
00286      PROGRAM VSLIT(INPUT,OUTPUT)
00290      PI=3.14159
00292      ACCEPT A
00293      A=A*PI/180.
00294      DO 100 I=0,10
00296      XI=I
00300      WT=XI*.5*PI/180.
00301      WT5=WT*
                180./PI
00302      DISPLAY WT5
00303      DO 200 K=0,10
00304      XK=K
00306      XD=-.3125+XK*.03125
00310      CALL COMPUT(WT,XD,-.005,ALPHA1,BETA1)
00320      YD=.005+(XD+.3125)*TAN(A)
00330      CALL COMPUT(WT,XD,YD,ALPHA2,BETA2)
00331      XMIN=3437.74668
00332      ALPHA1=ALPHA1*XMIN
00334      ALPHA2=ALPHA2*XMIN
00336      BETA1=BETA1*XMIN
00338      BETA2=BETA2*XMIN
00340 00200 DISPLAY ALPHA 1,BETA1,ALPHA2,BETA2
00350 00100 CONTINUE
00360      RETURN
00370      END
```


Program for Computing θ^i and δ

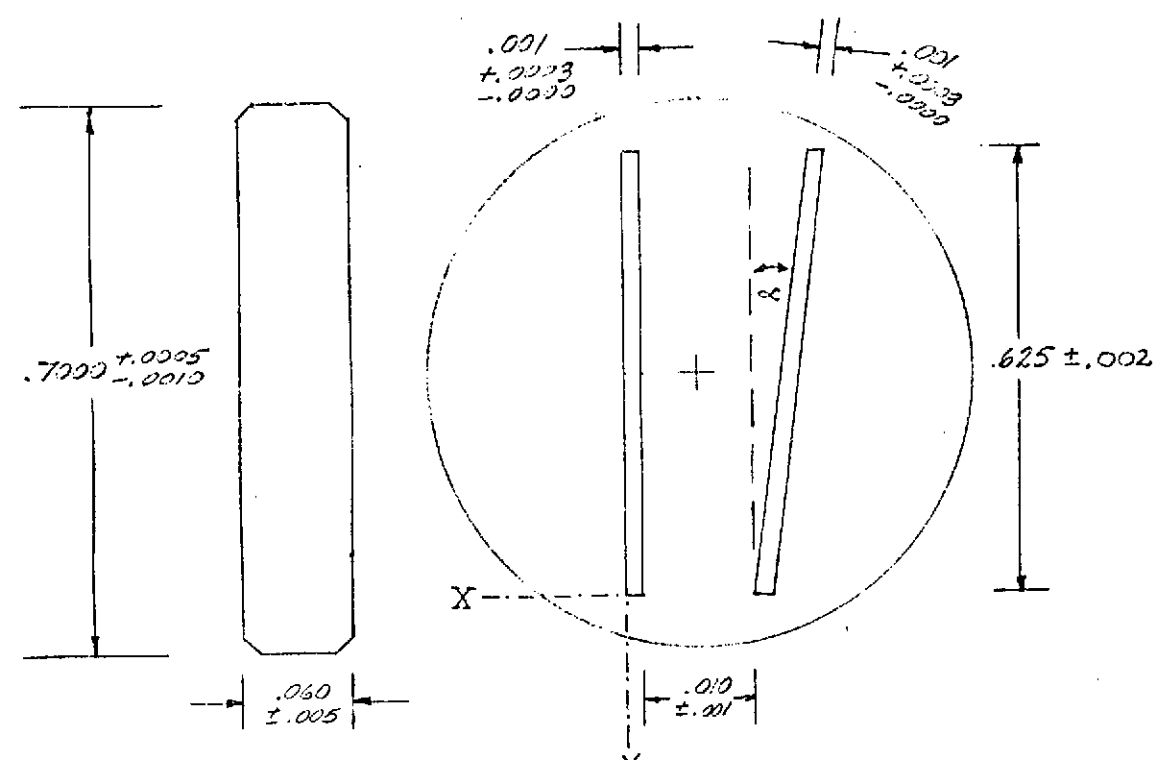
```
00100      PROGRAM SRA (INPUT,OUTPUT)
00110      PI=3.14159
00120      F=12.
00130      Q1=25.9*PI/180.
00140      SK=3437.75
00150      D0 100 I=1,20
00160      XI=11.
00170      Q=-.3125/12.+XI*.3125/120.
00180      SN=.005+(F*TAN(Q)+.3125)*TAN(Q1)
00190      SD=F*COS(Q)-F*TAN(Q)*SIN(Q)
00200      G=ATAN(SN/SD)
00210      G1=G*SK
00220      Q2=Q*SK
00230 00100 DISPLAY Q2,G1
00240      RETURN
00250      END
```

APPENDIX K

V-SLIT RETICLE

SK

REVISIONS			
LTR	DESCRIPTION	DATE	APPROVED



X, Y, CONCENTRICITY REFERENCE DATA LINES

NOTES

- DARK FIELD **CHROME** MASK
- OPTICAL DENSITY ≥ 3.0
- LINE IRREGULARITY ≤ 3%
- PINHOLES < .0001
- NO SPOTS IN CLEAR AREA
- ROUNDING OF SLIT CORNERS ACCEPTABLE, RADIUS ≤ .0005
- SUBSTRATE - PRECISION FLAT GLASS
- BREAK - ALL EDGES
- ALL DIMENSIONS IN INCHES EXCEPT THE ANGLE α

SK 229348	α (°) ± 30 SEC	CONCENTRICITY ±.003		QUANTITY
		X	Y	
-1	10	.034	.313	2
-2	15	.048	.313	2
-3	20	.063	.313	2
-4	25.9	.082	.313	2

ENGINEERING SKETCH		TRW SYSTEMS GROUP ONE SPACE PARK • REDONDO BEACH, CALIFORNIA	
ORIGINATOR <i>M. J. O.</i>	DATE 8-22-73	V SLIT RETICLE	
MJO 2293-48	SIZE A	CODE IDENT NO. 11982	SK 229348-1,2,3,4
SCALE NONE		SHEET 1 OF 1 K-2	

APPENDIX L

STAR SOURCES AND SPECTRAL CALIBRATION

A star source consists of a pair of 60 watt quartz iodine lamps mounted in a finned housing, color correction filters, and an opal glass diffuser. The exit aperture is 1/2" in diameter and the final pinhole source is achieved by mounting a pinhole aperture over the center of the 1/2" area. The star sources used in the testing of the SRA are pictorially shown in Figure L-1. The I-69 color filter is a Corning heat absorbing glass used to remove the IR part of the spectrum from the G.E. 1960 quartz iodine lamps. The I-62 color filter is a Corning blue-green filter which is supposed to raise the color temperature from 3000°K to 6900°K. The opal provides a Lambertian surface of irradiation and the aperture reduces the radiation to the proper value to simulate Canopus in the test set up. The SN-1 source is operated at 5.31 amps while the SN-2 source is operated at 5.33 amps.

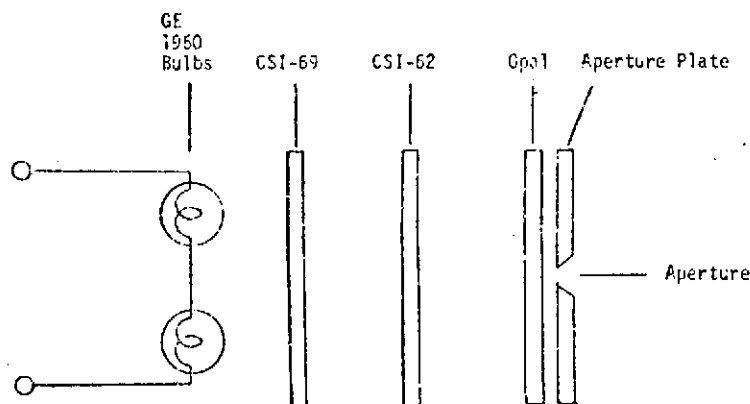


Figure L-1. Pictorial Schematic of Star Source Optical System

CANOPUS

The Canopus standard used for reference purposes was developed by R. Norton at JPL. This development is covered in detail in his paper entitled "The Absolute Spectral Energy Distribution of Canopus" JPL Technical Report Number 32-641, 15 August 1964.

Intensity Map

Because of the rather low intensities, it is necessary to make measurements with the entire 1/2" aperture exposed. In the past, it has been assumed that the illumination over this area is sufficiently uniform that the average value can be used to determine the intensity at the pinhole. Determinations of the spectral shape and the absolute intensity have been made for the 1/2" aperture by comparison to standard irradiance sources and the result assumed to be typical of the center of the aperture. This assumption has now been checked by mapping the intensity over the 1/2" area with a Gamma Corp. photometric microscope. The effective diameter of the scanning spot was about 0.011 inch. The relative intensity was measured at 0.020 inch intervals along "slices" spaced 0.020 inch apart. Figure L-2 is a "three dimensional" plot of the results of these measurements for SN-2 (a few orthogonal slices were taken to verify the measurements, with reasonable correlation resulting).

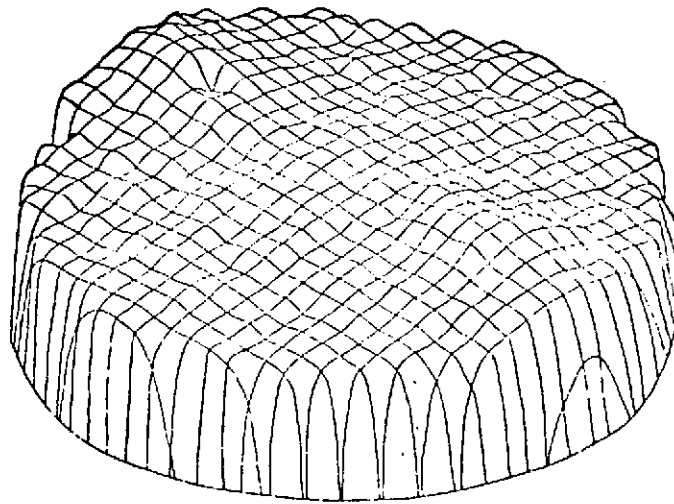


Figure L-2. Non-uniform irradiance of 1/2 opal surface

The plot is terminated at 50% signal amplitude. The difference between the amplitude at the center and an average amplitude over the plot is of the order of 13%..

SN-1 was checked only for a pair of orthogonal diameters, which showed the same shape as SN-2. Values were interpreted according to the same pattern and gave a correction of about 8%.

Spectral Shape and Absolute Calibration Using Monochromator

The spectral shape of the emission was determined by a wavelength by wavelength comparison with several standards of spectral irradiance. The light from each of these sources was allowed to illuminate the diffuser of the input optics of an EG&G grating monochromator which is equipped with a photomultiplier detector. The detector has an S-1 photocathode and proved to have adequate sensitivity for measurement over the entire spectral range. The PMT is cooled by a thermoelectric cooler, which stabilizes the temperature and minimizes drift and dark current. In order to cover the spectral range, the use of two different gratings and several filters to block higher orders is required. Overlapping readings were made at each point where these changes were made, and in the case of the grating change, overlapping of a larger portion of the scale was also done. The slits used in the monochromator result in an equivalent spectral bandwidth of 20 nm for the UV-visible grating and 40 nm for the IR grating.

One of the deficiencies of the measurement is that a long time elapses between the measurements taken for the two sources at comparable wavelengths, and a consequent greater sensitivity to drift in detector characteristics. Repeated measurements separated by a time interval of an hour or two give an estimate of the magnitude of effects attributed to drift. Finally, the distance to the diffuser of the input optics from each of the sources was measured in order to permit calculation of an absolute level from the input data. The shortest distance was from the diffuser of the star source. The distance was about 4 inches and resulted in illumination which appeared quite uniform over the input diffuser under visual examination. The source itself subtends a half angle of about 3-1/2 degrees at this distance, with the result that cosine effects are small and the use of inverse square

scaling for other distances is justified, since other measurement inaccuracies can be expected to give larger errors than those associated with this cause; assuming a $\cos^4 \theta/2$ dependence, the 3-1/2 degree angle will result in a deviation less than 1% for areas at the outer edge of the source, with the average being much less. The distances for the two 1000 watt irradiance standards was of the order of 19 feet and for the Gamma irradiance standard it is about 15 inches.

Because earlier workers at TRW using the EG&G monochromator had indicated that the wavelength indication is slightly in error, the monochromator wavelength dial was checked against prominent lines of the mercury spectrum. It was found that peaks could be located repeatedly to within 1 nanometer or better of dial setting. When the dial values are compared to the published values, the correction curve given in Figure L-3 results. These corrections were incorporated in the processed data.

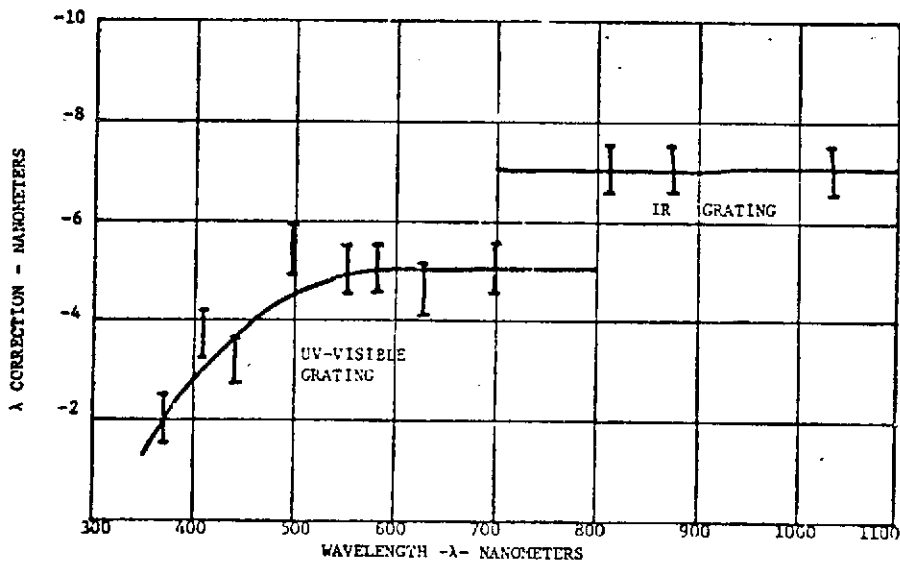


Figure L-3. WAVELENGTH CORRECTION CURVES

Figures L-4, L-5, and L-6 reproduce the spectral curves for SN-2 which resulted from comparisons with the three irradiance standards, while Figure L-7 is a smoothed composite of the three. The initial portion of the curve using the Gamma standard falls below values obtained when that portion was repeated an hour or so later, the deviations being of the order of 7%.

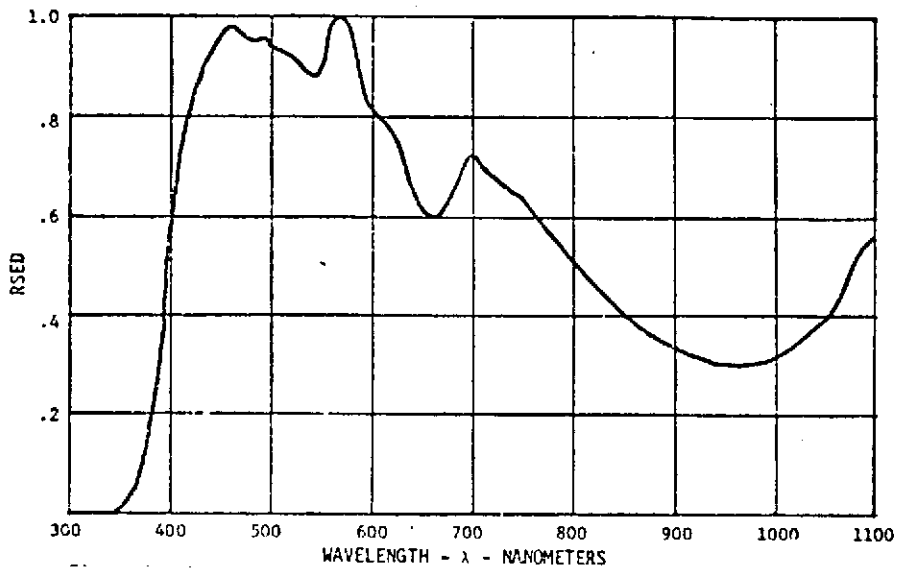


Figure L-4. Spectral shape of S/N 2 using Epply Standard 1466

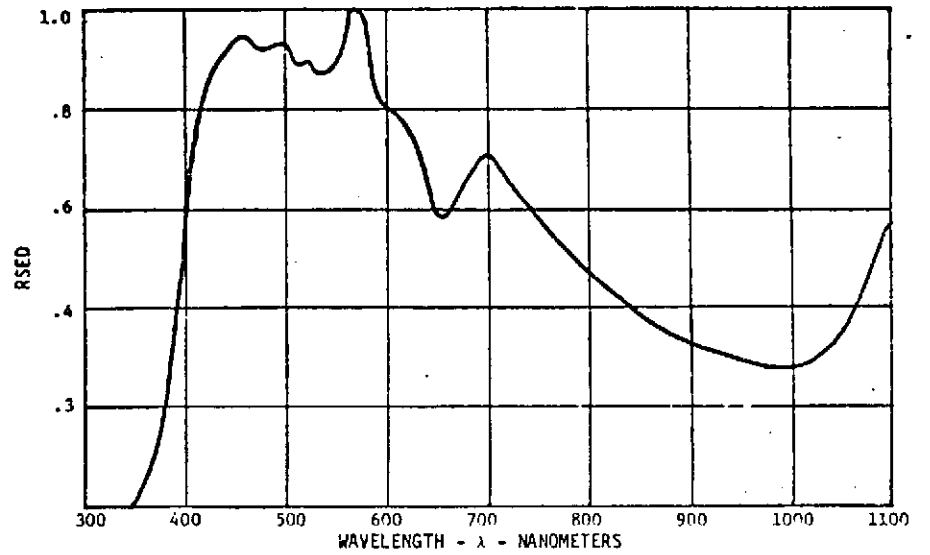


Figure L-5. Spectral Shape of S/N 2 using Epply Standard 1520

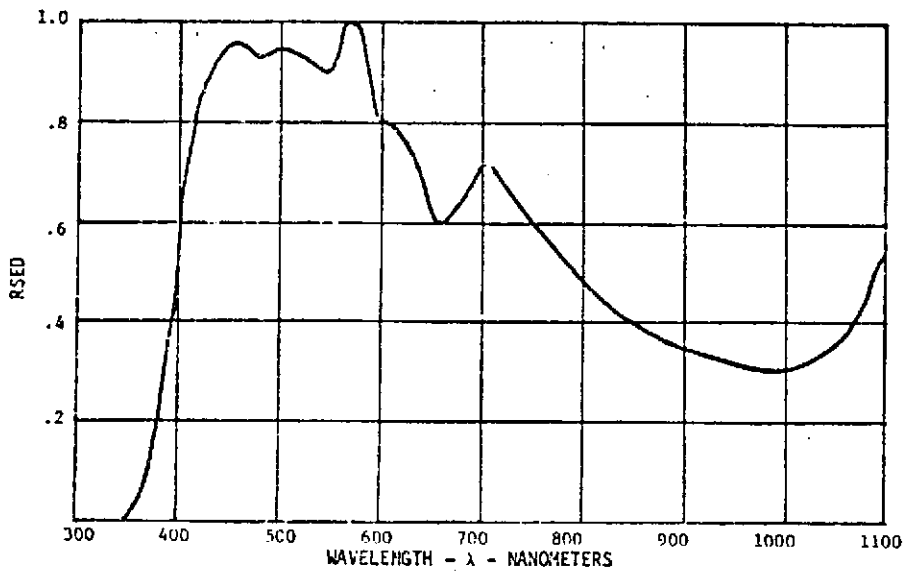


Figure L-6. Spectral Shape of S/N 2 using Gamma Scientific Standard

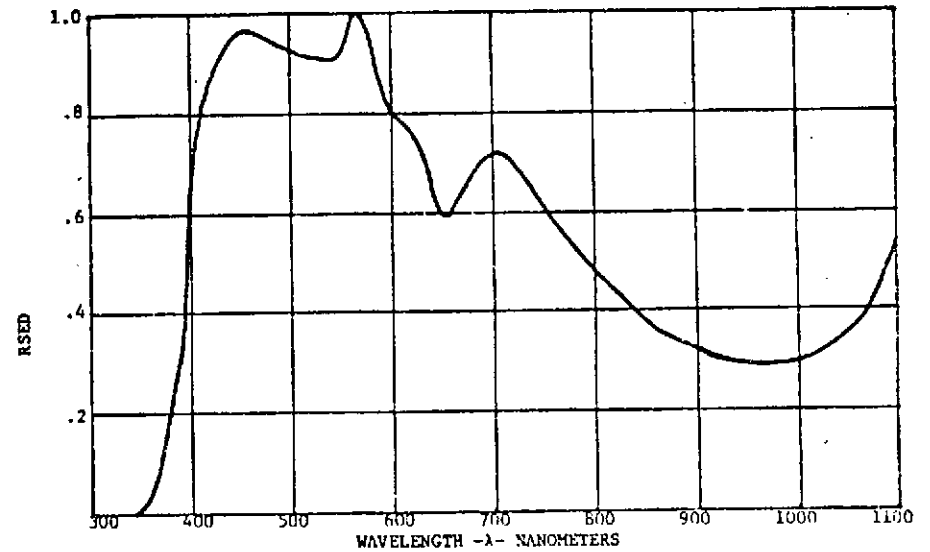


Figure L-7. S/N-2 COMPOSITE SPECTRAL SHAPE

Figures L-8 through L-11 present similar spectral shape data for SN-1.

Absolute Calibrations

The amplitude of the spectral curve for each source was determined by comparison to the standard sources using a series of filters to give narrow band radiation and a calibrated silicon solar cell to measure the intensity. The comparison was made with the three irradiance standards mentioned earlier in this section. The results were averaged to give absolute amplitudes at each of the filter test wavelengths. Those values in the intermediate spectral ranges, where the lamp spectrum and the detector have small slopes, were fitted to the measured spectral shape curve by least squares procedures, to give a peak amplitude for the spectral curve.

Figures L-12 and L-13 are plots of the three measured values at each wavelength, versus wavelength. A comparison with the spectral shape curve was used to select which wavelengths should be used in calculating the absolute value. In general, the shape disagreement was worst at the extreme wavelengths and these values were excluded in the least squares determination. Near the peak the variation between the three sources produces a peak-to-peak uncertainty of about 5%, as can be seen from an examination of the graphical presentation. At the short wavelengths and extreme long wavelength, this increases to about 16% and 20% peak-to-peak, respectively.

The peak irradiance for SN-2 is about 20% larger than SN-1. This may be partly due to surface contamination of the blue filter of SN-1 which was discovered only after these measurements were completed.

L-7

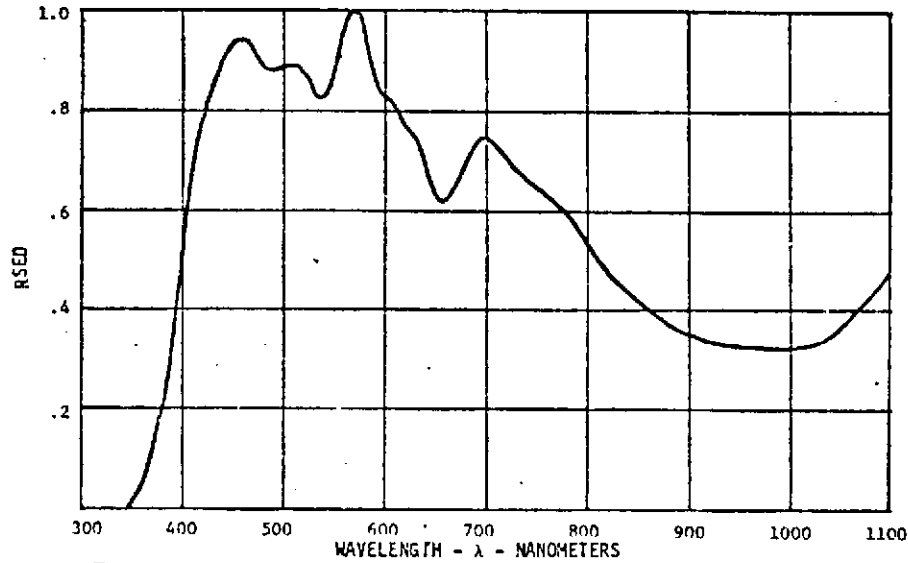


Figure L-8. Spectral Shape of S/N 1 using Epply Standard 1466

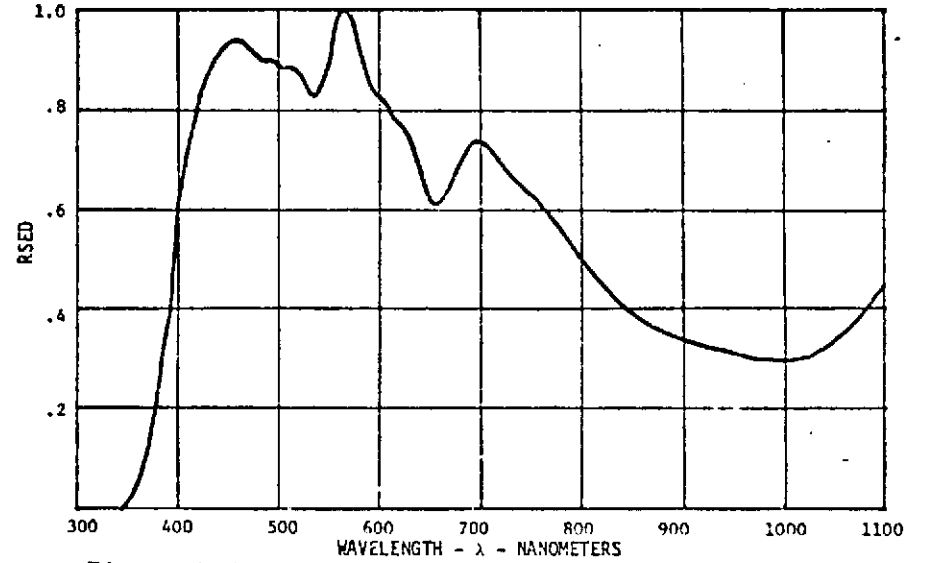


Figure L-9. Spectral Shape of S/N 1 using Epply Standard 1520

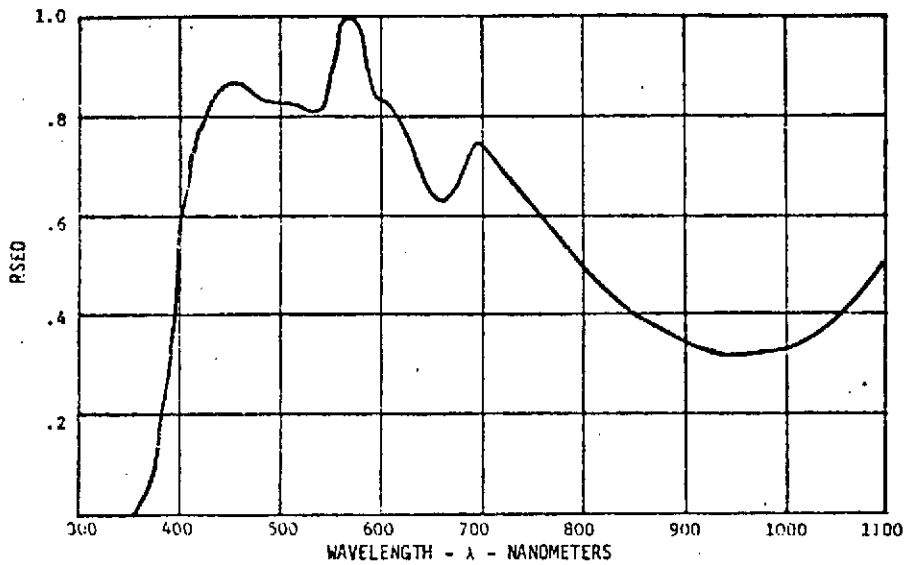


Figure L-10. Spectral Shape of S/N 1 using Gamma Scientific Standard

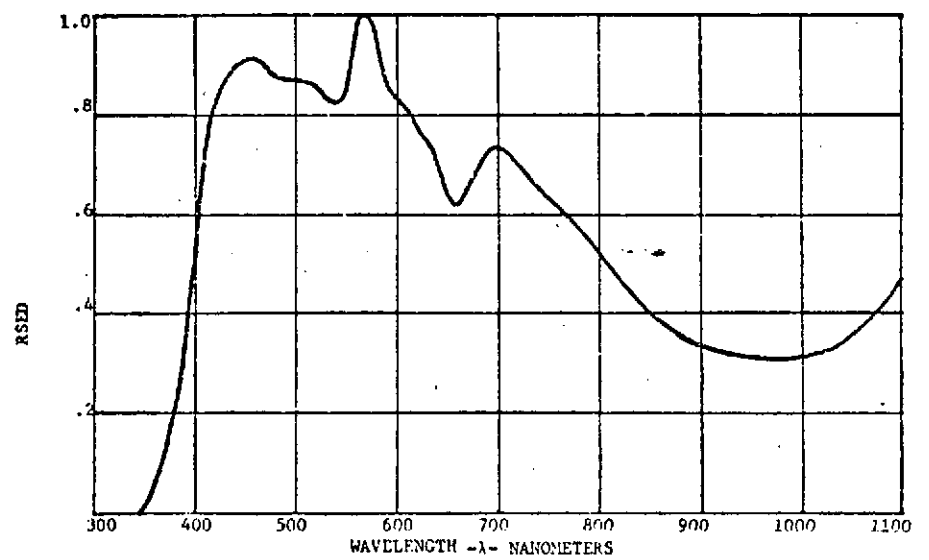


Figure L-11. S/N-1 COMPOSITE SPECTRAL SHAPE

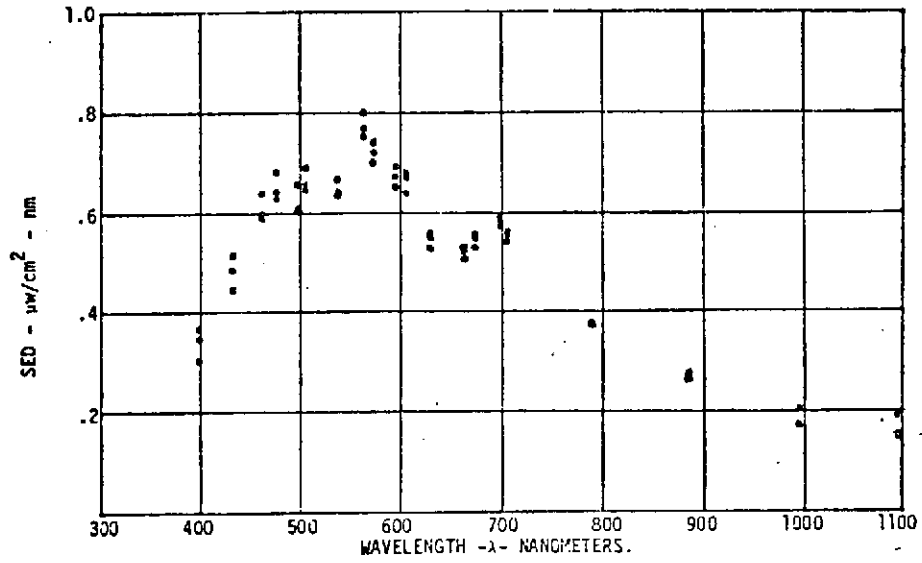


Figure L-12. Absolute SED of S/N 1 Source

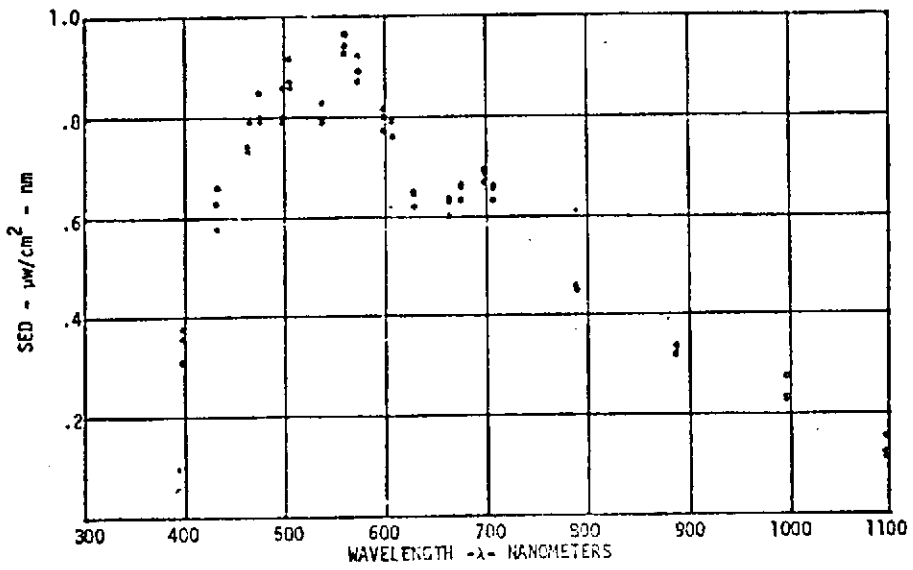


Figure L-13. Absolute SED of S/N 2 Source